EXPERIMENTAL AND NUMERICAL STUDIES ON THE PERFORMANCE OF POLYETHYLENE-GRAPHENE BASED COMPOSITE PHASE CHANGE MATERIALS FOR THERMAL ENERGY STORAGE

Thesis

Submitted in partial fulfillment of the requirements for the Degree of

DOCTOR OF PHILOSOPHY

By

SANTOSH

DEPARTMENT OF MECHANICAL ENGINEERING

NATIONAL INSTITUTE OF TECHNOLOGY KARNATAKA,

SURATHKAL, MANGALORE-575025

SEPTEMBER, 2019

EXPERIMENTAL AND NUMERICAL STUDIES ON THE PERFORMANCE OF POLYETHYLENE - GRAPHENE BASED COMPOSITE PHASE CHANGE MATERIALS FOR THERMAL ENERGY STORAGE

Thesis

Submitted in partial fulfillment of the requirements for the Degree of

DOCTOR OF PHILOSOPHY

By
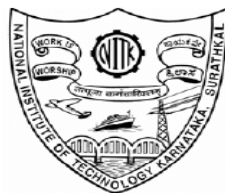
SANTOSH
(165078 ME16F16)

Under the Guidance of

Dr. VEERSHETTY GUMTAPURE

Associate Professor

Dr. ARUMUGA PERUMAL D

Assistant Professor

DEPARTMENT MECHANICAL ENGINEERING

NATIONAL INSTITUTE OF TECHNOLOGY KARNATAKA,
SURATHKAL, MANGALORE -575025
SEPTEMBER, 2019

D E C L A R A T I O N

I hereby declare that the Research Thesis entitled **"EXPERIMENTAL AND NUMERICAL STUDIES ON THE PERFORMANCE OF POLYETHYLENE-GRAPHENE BASED COMPOSITE PHASE CHANGE MATERIALS FOR THERMAL ENERGY STORAGE"** which is being submitted to the **National Institute of Technology Karnataka, Surathkal** in partial fulfilment of the requirements for the award of the Degree of **Doctor of Philosophy** in **Mechanical Engineering** is a *bonafide report of the research work carried out by me*. The material contained in this Research Thesis has not been submitted to any other Universities or Institutes for the award of any degree.

Register Number: **165078 ME16F16**

Name of the Research Scholar: **SANTOSH**

Signature of the Research Scholar:

Department of Mechanical Engineering

Place: NITK, Surathkal

Date:

C E R T I F I C A T E

This is to certify that the Research Thesis entitled **"EXPERIMENTAL AND NUMERICAL STUDIES ON THE PERFORMANCE OF POLYETHYLENE-GRAPHENE BASED COMPOSITE PHASE CHANGE MATERIALS FOR THERMAL ENERGY STORAGE"** submitted by **Mr. SANTOSH (Register Number: 165078 ME16F16)** as the record of the research work carried out by him, *is accepted as the Research Thesis submission* in partial fulfilment of the requirements for the award of the degree of **Doctor of Philosophy.**

R e s e a r c h   G u i d e s

Dr. Veershetty Gumtapure   **Dr. Arumuga Perumal D**

Associate Professor   Assistant Professor

Department of Mechanical Engineering   Department of Mechanical Engineering

Chairman-DRPC

Department of Mechanical Engineering

National Institute of Technology Karnataka, Surathkal

DEDICATED TO

MY BELOVED

FAMILY MEMBERS

ACKNOWLEDGMENT

ABSTRACT

Thermal energy storage domain is filled with composite phase change materials (CPCMs) for thermal performance analysis. The assessment is carried out for different nano additive materials such as copper and Al_2O_3 with square and rectangular geometric models. The interface morphology is used to understand the flow structure, and two-dimensional energy transport. The flow patterns are depending on the orientation (deep and shallow) of flow domain and initial sub-cooling. The orientation also has significant effect on formation of natural convection currents, heat transfer rate, and melting time. Effects of deep domain orientation (45˚, 90˚, 135˚ and 180˚) with different wall heating (base, left, top) conditions are analyzed numerically during melting and solidification processes. As the orientation changes, the heat transfer rate gets influenced significantly and convection currents amplifies. Next, to study the effect of geometry on melting and solidification characteristics, three different geometrical models of square, pentagon and hexagon are considered. Among the three models, hexagon model shown optimum results for both the heating and cooling processes with uniform and smooth variation in liquid fraction and temperature.

To achieve the competence in thermophysical properties nanoparticle are blended to base materials (polyethylene). In the present work, linear low-density polyethylene (LLDPE) is blended with functionalized graphene with different concentrations (1, 3 and 5%) and CPCMs are named as CPCM-1, CPCM-2 and CPCM-3 for 1, 3 and 5% respectively. Polyethylene-based composites with optimal concentration (3%) can be utilized for thermal energy storage applications. Higher nanoparticle concentration (5%) emulsifies the molecules and generates micelles between themselves.

The present work also attempts to address the energy issues by converting recycled plastics into thermal storage materials (TSM). Unfavorable thermophysical properties of plastic make it impractical, but these inadequacies can be amended by blending with additives of superior thermophysical properties such as functionalized graphene (f-Gr) and carbon-based nanoparticles. The experimental results shown energy level enrichment with nano

additive concentration. Among the TSM, CPCM-2 shows relatively better storage capability due to incorporation of optimum concentration of enhancing material. The solidification process takes place through convection and radiation mode of heat transfer. An energy storage estimation is also performed through characterization, numerical and experimental studies. Thermal energy storage model implementation determines the better utilization of thermal energy for a greener environment.

TABLE OF CONTENTS

LIST OF FIGURES

LIST OF TABLES

NOMENCLATURE

Greek Letters		Subscripts and Superscripts	
α	Thermal Diffusivity (m^2/s)	T_i	Initial Temperature (°C)
β	Coefficient of volumetric expansion	T_f	Final Temperature (°C)
ζ	Correction Factor	T_m	Melting Temperature (°C)
ε	Emissivity	T_{ref}	Reference Temperature (°C)
μ	Viscosity (m^2/s)	T_{melt}	Melting Temperature (°C)
ρ	Density (kg/m^3)	T_{room}	Room Temperature (°C)
φ_m	Mass Fraction	T_{max}	Maximum Temperature (°C)
Symbols		T_s	Surface Temperature (°C)
Q	Thermal energy / Heat (kJ)	T_a	Atmospheric Temperature (°C)
p	Pressure (N/m^2)	C_p	Specific Heat (kJ/kg K)
g	Acceleration due to Gravity (m/s^2)	C_{sp}	Specific heat in solid phase (kJ/kg K)
k	Thermal Conductivity (W/mK)	C_{lp}	Specific heat in liquid phase (kJ/kg K)
h	Heat Transfer Coefficient (W/ (m^2 K)	H_{fus}	Latent heat of fusion (kJ/kg)
Nu	Nusselt number	ΔH_m	Heat of Fusion (kJ/kg).
Pr	Prandtl's number	ΔH_c	Melting specific heat
Ra	Rayleigh number	ΔH_o	Solidification specific heat
Abbreviations			
BN	Boron Nitride	MFI	Melt Flow Index
CLHS	Cascade Latent Heat Storage	MMA	Methyl Methacrylate
CLHS	Cascade latent heat storage	NePCM	Nanoparticle Enhanced Phase Change Material
CNTs	Carbon Nanotubes	NFPCM	Nanofluid Phase Change Material
CPCM-1	Composite Phase Change Material -1	NGPs	Nano-Graphene Platelets
CPCM-2	Composite Phase Change Material-2	NLHS	Non-Cascade Latent Heat Storage

CPCM-3	Composite Phase Change Material -3	OA	Octadecanoic Acid
CPCMs	Composite Phase Change Materials	OA	octadecanoic acid
DSC	Differential Scanning Calorimetry	OMMT	Organophilic Montmorillonite
DSC	Differential scanning calorimetry	PA	Palmitic Acid
EG	Expanded Graphite	PCM	Phase Change Material
EPDM	Ethylene–Propylene–Diene Terpolymer	PCS	Phase change slurries
EVA	Ethylene Vinyl Acetate	PDMS	Polydimethylsiloxane
f-Gr	Functionalized Graphene	PEG	Poly Ethylene Glycol
FTIR	Fourier-Transform Infrared Spectroscopy	PLA	Poly Lactic Acid
GA	Graphene Aerogel	PMMA-MAA	Methyl Methacrylate Co-Methacrylic Acid
GNP	Graphene Nanoplatelet	PUPEG	Polyurethane Polyethylene Glycol
GnPs	Graphene Nano Platelets	SA	Stearic Acid
HAP	Hydroxyapatite	SAL	Stearyl Alcohol
HDPE	High Density Polyethylene	SEM	Scanning Electron Microscope
HTF	Heat Transfer Fluid	SEP	Sepiolite
LA	Lauric Acid	SHS	Sensible Heat Storage
LDPE	Low-Density Polyethylene	SL	Sodium Laurate
LHS	Latent Heat Storage	TES	Thermal Energy Storage
LHTES	Latent Heat Thermal Energy Storage	TGA	Thermogravimetric Analysis
MA	Myristic Acid	TSM	Thermal Storage Material
MA	Myristyl alcohol	TSU	Thermal Storage Unit
MAA	Methacrylic Acid	UDF	User-Defined Functions
MDs	Molecular Dynamics	XRD	X-Ray Diffraction

CHAPTER 1

INTRODUCTION

1.1 INTRODUCTION

Energy conservation and pollution control is a primary concern worldwide due to increase in global warming over the past few decades. The scientific community is also apprehensive about environmental issues caused by the usage of plastics and energy issues. Phase change material (PCM) based thermal energy storage technologies are encouraged as an alternative energy utilization opportunity (Xu et al. 2019). It is more important to harvest the available energy than searching for new resources. The mismatch between the solar thermal energy availability and the demand thrusts towards the new possibilities. Among several energy conservation methods, thermal energy storage (TES) is one of the proficient ways that bridge the intermittency of solar thermal energy. TES is achieved through different methods such as sensible, latent, and thermochemical heat storage. Among the methods, latent heat storage provides better results due to its isothermal. Sensible heat storage causes a change in temperature, whereas latent heat is stored during phase conversion. Latent heat storage is an effective way due to its high energy storage density at a constant temperature. In latent heat storage method selection of suitable material plays a significant role to address the thermal energy utilization (Dahash et al. 2019).

The most basic requirement for storing the latent heat is phase change material (PCM). The PCMs are of various categories, and their selection depends on the working temperature range like low-temperature thermal storage (melt range is between 0 and 120°C) used for several applications such as, domestic water heating, direct heating or heat-pump assisted space heating, greenhouse heating, solar cooling, etc. Medium temperature thermal storage (100 to 180°C) used for many industrial processes, e.g., food, paper, chemical industries

1

etc. High-temperature thermal storage (up to 900˚C) used for power plant and metallurgical applications (Bhatt et al. 2010).

Storage of energy eliminates or minimizes the gap between energy supply & demand, and it improves the performance of energy storage systems. The PCMs become significant for its excessive energy storage capacity, and it reduces the fluctuation of temperature during the day, stabilizes the temperatures in the required range. Researchers have shown much interest towards encapsulation of PCMs for large scale applications. PCMs with limited storage capacity can be blended with any suitable nanoparticles, to overcome the limitations of composite phase change materials (CPCMs) (Akeiber et al. 2016).

1.2 THERMAL ENERGY STORAGE

Thermal energy storage (TES) using PCM is an efficient method of storing and releasing a large amount of energy. The TES system is based on phase conversion of the material such as, melting, solidification or evaporation processes, which absorbs and releases energy during phase conversion and it may be solid to liquid and vice versa.
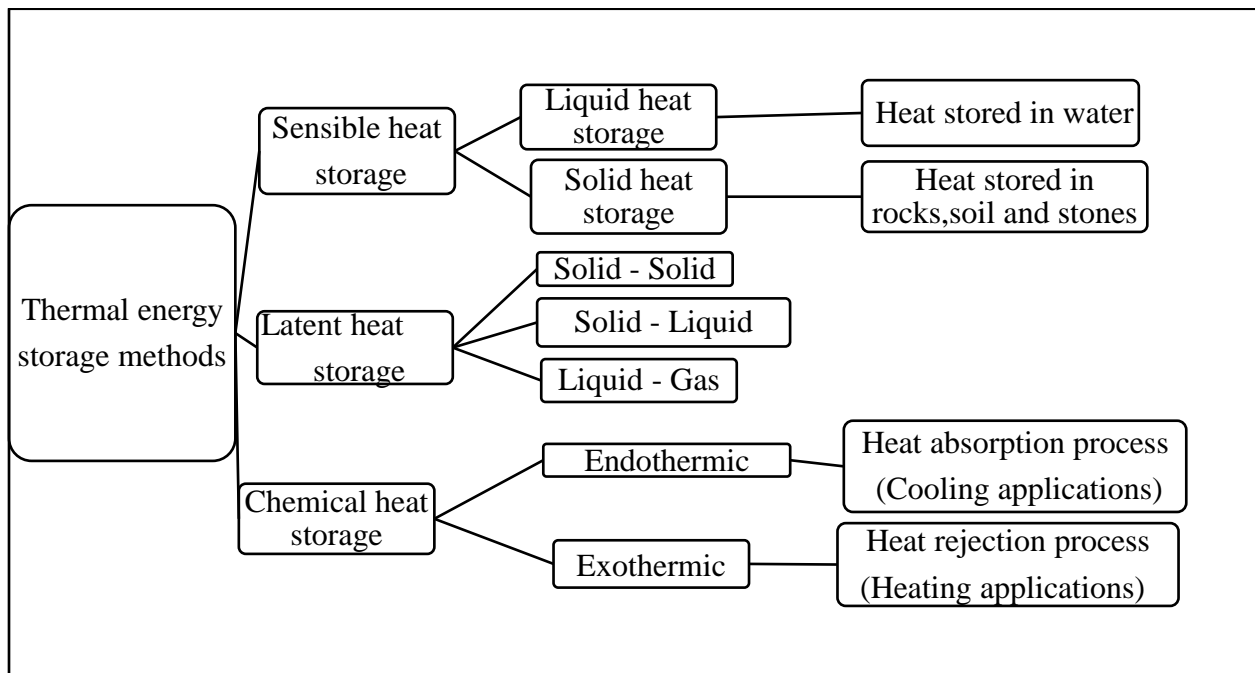
Figure 1.1: Methods of thermal energy storage (Abhat 1983) and (Sharma et al. 2009).

There are different methods of TES which are shown in figure.1.1. It is seen that the storage method depends on the availability of the energy and the required applications. First, latent heat storage where a large amount of heat energy is stored during the phase change process. The phase change may be solid-solid, solid-liquid, and liquid-gas. In solid-solid PCMs, only molecular crystalline structure changes, and its volume requirement limits its storage capacity. Solid–gas or liquid-gas phase change materials can exhibit higher latent heat of fusion, but these are not preferred due to their large volume requirement after phase conversion. Therefore, solid-liquid PCMs are considered to be the most practical and economical (Kumar and Shukla, 2015). Previous studies have shown that latent heat storage provides low-cost storage systems by using easily available PCMs (Bose and Amirtham, 2016).

1.2.1 Sensible Heat Storage

In sensible heat storage (SHS) system, the temperature of thermal storage material (TSM) changes during heat absorption and rejection. SHS system uses the specific heat capacity and temperature difference of the material during charging and discharging processes.
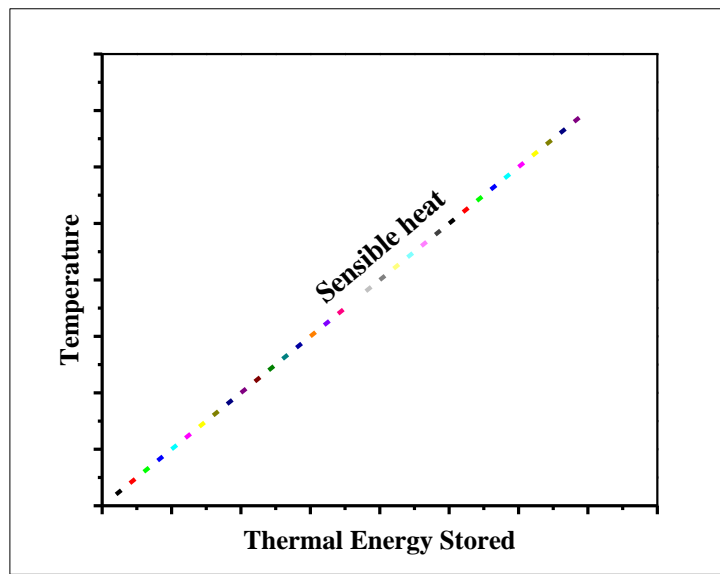
Figure 1.2: Thermal energy storage in sensible heat form with temperature.

The amount of heat energy stored depends on the specific heat of the TSM, the temperature difference, and the quantity of storage material. Figure 1.2 shows the thermal energy storage in sensible heat form with temperature.

$$Q_{Sensible} = mCp(T_f - T_i) \qquad (1.1)$$

Where Q is the amount of thermal energy absorbed or rejected in sensible heat (kJ) form, T_i and T_f are initial and final temperature (°C), m and C_p are the mass (kg) and specific heat (kJ/kg°C) of used storage material. Sensible heat storage using solid materials like, stones, bricks, pebbles, and liquid material is water, gas materials have very low volumetric heat capacity, and it is not used for sensible heat storage.

1.2.2 Latent Heat Storage

In latent heat storage (LHS) system, thermal energy is stored or released during phase conversion without changing temperature. Phase conversion may be solid to liquid or liquid to gas or vice versa. Figure 1.3 shows thermal energy storage in sensible and latent heat form with temperature.
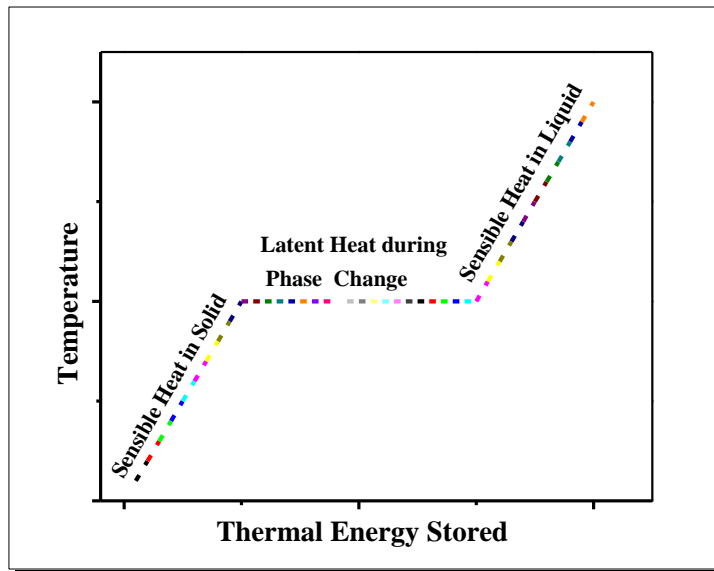
Figure 1.3: Thermal energy storage in sensible and latent heat form with temperature.

The latent heat storage capacity with PCM is given by

$$Q_{Latent} = m[C_{sp}(T_m - T_i) + \varphi_m \Delta H_m + C_{lp}(T_f - T_m)]$$ (1.2)

Where Q is the amount of thermal energy stored or released in latent heat (kJ) form, T_i , T_m and T_f are initial, melting and final temperature (°C) respectively, m is the mass (kg) and C_{sp}, and C_{lp} are specific heat (kJ/kg°C) in solid and liquid state of used storage material, φ_m is melted fraction and ΔH_m is the heat of fusion per unit mass (kJ/kg). The first term of the Equation 1.2 represents the amount of heat stored or released between the melting temperature and initial temperature. The second term represents the energy released during phase conversion, and the last term represents the sensible energy stored or released between the final temperature and melting temperature.

1.2.3 Thermochemical Heat Storage

Thermochemical heat storage system absorbs and releases energy during breaking and reforming molecular bonds in a complete reversible chemical reaction. The amount of heat energy stored depends on the amount of storage material used, the heat absorbed during an endothermic chemical reaction, and heat released during the exothermic reversible chemical reaction. The amount of heat energy stored and released can be written as

$$Q_{Reaction} = m\varphi_m \Delta H_m$$ (1.3)

Where Q is the amount of thermal energy stored or released in form chemical reaction (kJ), m (kg) is the mass of storage material used, φ_m is melted fraction and ΔH_m is the heat of fusion per unit mass (kJ/kg).

1.3 PHASE CHANGE MATERIALS AND ITS CLASSIFICATIONS

Phase change materials are materials which melt and solidifies at a specific temperature when it is heated or cooled subsequently, and the temperature at which phase change occurs is called as the phase change temperature of that material. The selection of proper PCM for a specific application is essential for the different range of applications to select proper material. Commonly available PCMs and its classifications are shown in Figure 1.4. It is quite unfortunate that no single material can fully satisfy all the desirable properties

5

required for thermal storage applications. Apart from the disadvantages related to volume requirements, organic PCMs work as essential heat storage materials. Paraffins are the substances which are having straight chains of hydrocarbons with a small amount of branching near the end of the chain, which are characterized as alkanes (C_nH_{2n+2}). These are again classified depending upon the chain length of the alkane. Paraffins with hydrocarbon of branched-chain structures is called iso-paraffins. The inorganic PCMs are not preferred in the TES systems due to their supercooling effect, toxicity, corrosivity and other harmful properties. However, the usage of paraffin is also complicated due to their undesirable leakage problem in the molten state (Yang et al. 2016a). To achieve better storability with safety, two or three PCMs are mixed to form binary or ternary eutectics (Tang et al. 2016a).
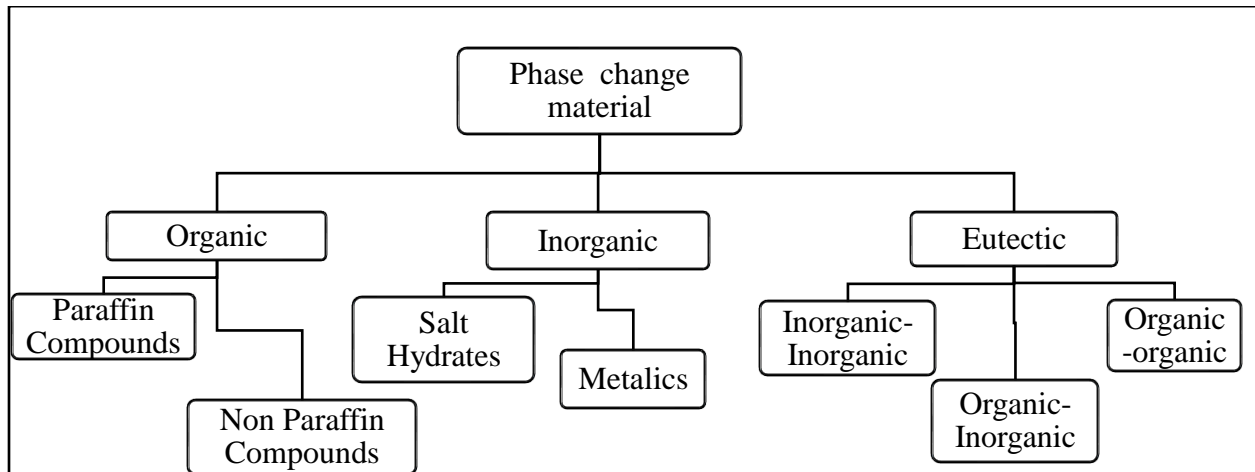
Figure 1.4: Classification of PCMs (Abhat 1983) and (Sharma et al. 2009).

Eutectic is a composition of two or more materials, each of which melts and solidifies without forming accumulation separately and changes phase without segregation of component materials, eutectic mixture (*e.g.,* salt hydrates) have high storage density and higher thermal conductivity as compared to paraffins.

1.3.1 Characteristics of Phase Change Materials

Table1.1 shows the phase change materials and their properties in detail. The PCMs selected for application should possess the following characteristics.

- Should sustain the operating temperature with proper phase transition.
- Should possess high latent heat to reduce the size of the storage structure.
- Should possess high thermal conductivity to make system charge faster.

Table 1.1 Phase change materials and their properties (Bailey 2010).

Material	Type	Desirable Properties	Undesirable Properties
Organic Materials	Paraffins	Non-corrosive	Low thermal conductivity
		Chemically stable up to 500°C	Non-compatible with the plastic container
		Less expensive	Moderately flammable
		Reliable	
		Safe and Predictable	
	Non Paraffins	High heat of fusion	Inflammability
		No supercooling	Low thermal conductivity
		Some fatty acids can be used for low-temperature latent heat thermal energy storage applications	Low flashpoints
			Instability at high temperatures
Inorganic Materials	Salt Hydrate	High latent heat of fusion per unit volume	Slightly toxic
		Relatively high thermal conductivity (almost double of the paraffins).	Require supercooling
		Change in volume is small while melting.	
		Non-corrosive	
		Compatible with plastics	
	Metallic	High thermal conductivity	Low specific heat
		Low heat of fusion per unit weight	Relatively low vapor pressure
		High heat of fusion per unit volume	

- Should possess high density to provide better stability during melting and solidification.
- The volume required for phase transition must be small, and it should not require supercooling.
- Should be chemically stable (*i.e.,* should not degrade, should be non-toxic and should be non-explosive).

1.3.2 Role of Composite Phase Change Materials

Storing thermal energy using composite phase change materials (CPCM) is one of the alternative approaches to enhance the thermophysical properties of PCMs, which delivers exciting results with different compositions of base materials and additives. Materials with high energy storage capacity used for thermochemical heat storage are selected for a suitable range of chemical reaction temperatures (André et al. 2016). Recently, researchers adopted the encapsulation method to enhance the performance of TES by mixing of nanomaterials with PCMs. This is done to improve certain properties such as low thermal conductivity, supercooling and incongruent melting (solid substance does not melt uniformly, decomposing into another solid and a liquid with different compositions) (Raam Dheep and Sreekumar 2014).

Metals and metal oxides can be added to traditional PCMs in which carbon-based nanomaterials are more suitable because of their excellent thermophysical and thermochemical properties. For lower temperature range, inorganic PCMs are adequate, but it leads to corrosion, incongruent melting, and supercooling. To overcome these confines, one can go for organic PCMs, but organic PCMs have relatively lower thermal conductivity and heat transfer rate, which can be eliminated by adding metals and metal oxides.

1.4 APPLICATIONS OF THERMAL ENERGY STORAGE SYSTEMS

Thermal energy storage techniques can be used for different applications such as solar water heating systems, solar cookers, building applications, industrial waste heat recovery. As an application, solar water heating systems consist of a storage tank and solar collectors.

There are two types of solar water heating systems. They are active solar water heating systems with circulating pumps and controls and passive solar water heating systems without pumps and controls.

Thermal energy storage systems are also useful in a wide variety of applications. Beginning with the lower-temperature region, district heating processes use TES units for seasonal and buffer storage. In the non-residential building sector, heat is managed both for domestic hot water production and space heating. Industrial processes use thermal energy storage primarily for waste heat recovery and process efficiency. Power plant applications, particularly those in concentrating solar power, use TES systems to improve performance and increase the operational efficiency of process units. In automobile applications, TES systems are seeing developmental work in waste heat recovery and thermal management.

1.5 MOTIVATION OF THE PRESENT WORK

Most of the studies are carried out for paraffin-based composite phase change materials for thermal energy storage analysis. Polyethylene and polyethylene-based materials are not much explored due to poor thermophysical properties. Limited work has been carried to use the waste or recycled plastic for thermal energy storage application. Polyethylene-graphene-based materials are remained unrevealed to evaluate thermal performance. Limited experimental investigations are carried out for plastic-based materials to assess the thermal storage capacity. Polyethylene-graphene based composite phase change materials (CPCMs) are least discovered. An attempt is also made to address the issues by using waste plastics as the thermal energy storage material. The present work deals with the development of composite phase change materials consist of linear low-density polyethylene blended with functionalized graphene nano additives.

1.6 OBJECTIVES OF THE PRESENT WORK

The objectives of the present research work are to develop, characterize, and analyze the performance of composite phase change materials. The important objectives are as follows.

1. Parametric analysis of composite phase change materials for melting and solidification characteristics in bounded domains.
2. Development, characterization, and analysis of polyethylene-graphene based composite phase change materials for enhanced thermophysical properties.
3. Numerical investigation of different composite phase change materials for thermal performance evaluation in bounded domains.
4. Experimental investigation of polyethylene-graphene based composite phase change material in a bounded domain to enhance the thermal storage capacity.

1.7 ORGANIZATION OF THESIS

This thesis is organized into six chapters to understand the nature of the present work.

Chapter 1 Provides a brief introduction about the thermal energy storage systems, methods, and materials used for applications, thermal energy storage methods, and suitable material properties. Applications of thermal storage systems, motivation for the present research work and objectives are listed at the end this chapter.

Chapter 2 Gives an exhaustive literature survey related to thermophysical properties enhancement, thermal storage improvement, and suitability of materials. This chapter also provides insight about the research gap and summary of the literature review.

Chapter 3 Discusses the materials and methods used in the present research work. Preparation of composite phase change materials and characterization methods are also discussed.

Chapter 4 Focuses on parametric analysis of different composite phase change materials, and various geometrical models to analyze the thermal storage capability. Analytical calculations, and numerical simulation of the 2-D model adopted in the research work is also discussed in the same chapter.

Chapter 5 Gives detailed procedure of different characterization through Fourier transform infrared spectroscopy, scanning electron microscopy, and differential scanning calorimeter analysis. Thermal storage analysis of the prepared composite phase change materials is carried out analytically and numerically.

Chapter 6 Presents the experimental and numerical methods employed in the study to estimate the thermal storage performance. It also discusses the nature of heat transfer to and from the thermal storage medium with the variation of energy level and temperature with charging and discharging time.

Chapter 7 Contains the significant conclusions drawn from the results. In the end, concluding remarks and scope for future work are made.

CHAPTER 2

LITERATURE REVIEW

2.1 INTRODUCTION

This chapter is dedicated to reviewing the enhancement of the thermophysical properties, different composite phase change materials, nanoparticle concentrations, thermal energy storage materials through characterization, numerical and experimental studies of different material combinations and compatibility.

2.2 ENHANCEMENT OF THERMOPHYSICAL PROPERTIES OF CPCM USING CHARACTERIZATION STUDIES

Composite phase change materials are becoming popular due to its wide range of applications compared with other base materials. One of the ways to enhance the properties of materials through characterization study. Composite materials are used in thermal energy storage (TES) systems with the enhancement of thermophysical properties. Several experiments are conducted to investigate the composite behavior with different material compositions. In ceramic composites, the highly conductive additive material is mixed to provide excellent structural stability to the PCM (Zhou et al. 2014). The high thermal conductivity material increases the overall thermal conductivity of the composite material, such as magnesium oxide to provide structural stability. It is known that carbon allotropes are thermal conductivity enhancing materials with excellent physical and chemical stability (Ge et al. 2014). Eutectic salt of lithium and sodium carbonate can be used as PCM for medium and high-temperature TES applications. To provide wettability and stability the composite structure can be blended with carbon allotropes (Ye et al. 2014).

A polyurethane-based PCM synthesized by polymerization method in which polyethylene glycol (PEG) is mixed with graphite nanoplatelets, and it is characterized by Fourier-

transform infrared spectroscopy (FTIR) analysis, Differential scanning calorimetry (DSC) study, Thermogravimetric analysis (TGA), Scanning electron microscope (SEM) study and Ultrasonic techniques. It also provides better crystal structure and enhances thermal conductivity with increase in graphite nanoplatelets concentration (Pielichowska et al. 2016b). In PEG, boron nitride (BN) and graphene nanoplatelets (GNP) are mixed, the presence of GNP enhances thermal conductivity and thermal energy conversion (Yang et al. 2017). Polymorphic nature of mannitol is also suitable for thermal storage application to provide thermal stability. To find the thermophysical behaviour of mannitol, galactitol and mannitol mixture is prepared and analyzed with the help of DSC analysis, X-ray diffraction (XRD) and FTIR analysis. The eutectic mixture at 30:70 molar fraction of galacititol and mannitol (ΔH_{fus} = 292 J/g) at melting point 153℃ provides better cyclic, thermal and chemical stability in comparison with individual state in nitrogen or air with suppressed supercooling (Paul et al. 2015).

A PEG is a white free-flowing powder or creamy white flakes which is considered as an efficient PCM for TES applications, due to its relatively high latent heat of fusion, congruent melting, freezing behavior, appropriate melting temperature range, non-corrosiveness and non-toxicity property (Torkkeli 2003). A CPCM of PEG and cellulose/graphene nanoplatelets (GNP's) aerogel with 5.3 wt.% of GNP in CPCM enhances the thermal conductivity up to 463% and also provides better stability by developing porous cellulose network which prominently influences the thermal conductivity (Yang et al. 2016b). Polyurethane polyethylene glycol (PUPEG) is mixed with graphene (as a chain extender) to enhance the thermal conductivity and thermal stability. The increase in graphene concentration increases the thermal conductivity, and CPCM retains its thermal reliability even after 100 thermal cycles both under air and nitrogen atmosphere (Pielichowska et al. 2016a). To achieve better thermal stability during large number of thermal cycles, a eutectic mixture of myristic acid/palmitic acid/sodium laurate (MA/PA/SL) is prepared. The CPCM sustained up to 1000 thermal cycles with the same charging / discharging ability with minor changes in the conversion capability (Fauzi et al. 2014). Eutectic mixture of sodium nitrate and potassium nitrate with alumina

nanoparticles greatly influences the specific heat capacity. The nanoparticle concentration increases specific heat capacity up to 30.6% at 0.78% mixing (Schuller et al. 2015).

The PCMs blended with nanoparticles like expanded graphite, exfoliated graphite nanoplatelets or carbon nanotubes (CNTs) improves the thermal properties and no change in structural stability. To provide better structural stability microcrystalline cellulose and light-weight cellulose is the possibilities because it forms three-dimensional strong porous structures. For TES application, paraffins and paraffin-based CPCMs are most beneficial, but the drawback is low thermal conductivity, due to more charging /discharging time. To reduce the charging/discharging, time nano-fillers are used, primarily carbon-based nanomaterials, such as short and long multi-walled carbon nanotubes (S-MWCNT's and L-MWCNT's), carbon nanofibers and GNPs. The S-MWCNT's exhibits the best dispersion due to its smaller geometry. GNPs has shown higher thermal conductivity enhancement in composite material 170% at 5 wt% of blending (Fan et al. 2013).

2.3 ENHANCEMENT OF THERMOPHYSICAL PROPERTIES OF CPCM USING EXPERIMENTAL STUDIES

Experimental investigation of paraffin and copper foam-based CPCM exhibits enhancement of TES capacity for a short duration (Wang et al. 2016a). Paraffin with nano zinc oxide in the tubular shape shown satisfactory results for thermophysical properties enhancement, but specific heat capacity reduces (7%) (Şahan and Paksoy 2017). Usage of pure metals does not give relevant results, to look forward for better performance metal oxide and metal hydrates are used. Among many transition metal oxides, RuO_2 is preferred for electronic supercapacitor devices due to high reversible redox reactions, longer life cycle, and metallic type conductivity. These excellent properties of RuO_2 motivate researchers for thermal energy storage applications (Zheng 1995). Ruthenium (Ru) and Iridium (Ir) nano-oxide properties are altered by changing oxide compositions. Addition of Iridium eliminates the catalyst passivation and improves the activity at a higher temperature. To develop the existing potential, preferably the thermochemical systems working under 400-1200˚C range (for the thermochemical storage applications) metal

carbonates, hydroxides and metal oxides provides significant results (Audichon et al. 2017).

The CPCMs are prepared and characterized using superolephilic graphene nickel foam as a porous supporting material, SEM and XRD images indicates crystal structure arrangements, and thermal properties are measured using DSC analysis. This microstructural analysis reveals the excellent thermal conductivity and thermal stability of CPCM. Form-stable expanded graphite (EG) / stearic acid (SA) based CPCM shows better thermal stability for a wide range of operating temperature with excellent thermal performance. It reduces porosity and improves TES capacity per volume. Palmitic Acid (PA)/ SA and GNPs and EG of various proportions are fabricated and analyzed for thermophysical properties analysis (Yuan et al. 2016).

The CPCM of graphene aerogel (GA) and octadecanoic acid (OA) have thermal conductivity (14 times) more than that of the base material at 20 vol% loading, and high TES capacity (Zhong et al. 2013). Graphite nanofibers mixed with paraffin is studied with different parameters, like aspect ratio, power density, solidification, and melting time. The results showed reduction in melting and solidification time by 61%, and enhancement of thermal storage capacity up to 48% (Sanusi et al. 2011).

The betterment of CPCM for medium and high-temperature thermal storage applications salt-based composite materials are prepared and investigated. The thermal characteristics shown greater chemical stability and higher thermal conductivity by the addition of magnesium oxide and carbon allotropes. The oxides of lithium carbonate increase dispersion in amorphous powder which results in high specific heat capacity of molten salt. The molten salt with nanofluids shows higher potential towards concentrated solar power systems (Arthur and Karim 2016). Addition of 0.05 wt% of graphene in epoxy/ graphene composite enhances the thermomechanical properties and better dispersion in composite material. The higher concentration of graphene causes a reduction in mechanical properties due to aggregation of graphene particles (Saha et al. 2016). Aluminate cement and nano magnesium oxide CPCM affects mechanical and thermal properties. It also optimizes the pore distribution and enhances the thermal conductivity by 34.8 % and 40.8% at 1 and 2

wt% respectively. Overall, experimental and characterization studies represent similar facts to achieve the better TES capacity of potential materials (Yuan et al. 2014).

Paraffin based materials are complicated due to leakage problems during the melting process, which limits its TES application. To compensate for this problem, Rude-Palygorskite (Pal) is mixed with the paraffin, and the composite is analyzed through FTIR and DSC analysis. The Pal composite shows improvement in thermophysical properties and better stability after 500 thermal cycles with negligible change (5 J/g) in latent heat capacity (Yang et al. 2016a). The experimental investigation is carried out to avoid the leakage problems by mixing PEG (up to 85 wt%) in the composite, and the analysis shown better thermal reliability and stability (Liu et al. 2017b).

PEG is a light density, high thermal conductivity, heat storage capacity and good stability material which makes it attractive PCM for TES applications (Ferrão 2017). To improve the thermal properties, myristyl alcohol (MA) is blended with nickel and copper metal foams. The thermal conductivity of CPCM enhances 88% with a reduction of specific heat capacity up to 29% (Huang et al. 2017). Hydroxyapatite (HAP) is used to improve the stability for thermal energy storage application (Wang et al. 2017). The composite based PCM shows better chemical compatibility and thermal conductivity due to graphite addition (Xu et al. 2017a). TES systems based on gypsum composites significantly reforms the thermal performance with an increase in diatomite/paraffin concentration (Liu et al. 2017a).

Continuous efforts making thermal storage systems more effective through different techniques like encapsulation, micro encapsulations, etc, poly (methyl methacrylate-co-methacrylic acid) (PMMA-MAA) is prepared and experimented for methyl methacrylate (MMA) and methacrylic acid (MAA). The thermal conductivity improved and high storage capacity is achieved (Pina et al. 2017). A composite of $LiNO_3$-KCl-$NaNO_3$ / expanded graphite conducted, and it shown high thermal conductivity, and a faster charging rate is achieved than the base material (Xu et al. 2017b). Lauric acid (LA) impregnated into modified sepiolite (SEP), and the composite showed better thermal reliability after 200 thermal cycles (Shen et al. 2017). To reduce the cost of energy conservation using easily

available materials will be an efficient way such as waste recyclable plastics, polyethylene, etc. High-density polyethylene (HDPE) and stearyl alcohol (SAL) blended expanded graphite (EG) exhibited improvement in the thermal conductivity (Tang et al. 2017).

Paraffin with copper nanoparticles (1 wt%) improves thermal conductivity and reduces melting time up to 13.1% (Wu et al. 2012). Various forms of CPCMs are developed such as slurries, eutectics, and different material blends to improve the heat transfer rate. Slurry is a binary composition of the carrier material, water (continuous phase) and PCM (dispersed phase), are called phase change slurries (PCS). PCS uses the latent heat capacity of the PCM and sensible heat capacity of the carrier material to store or transfer thermal energy (Youssef et al. 2013). A PCS (10 wt% paraffin) is employed to analyze the TES capability of the material. The energy stored in the slurry was 75% more than the energy stored in water at the same temperature, and the convective heat transfer coefficient also increases up to 25% (Delgado et al. 2012).

To study the thermophysical properties in micro-scale, molecular dynamics (MD) approach is employed to analyze the thermophysical properties of crystalline octadecane and octadecane–water slurry (Rao et al. 2012). The results exhibit that there is a reduction in heat capacity of octadecane slurry with a high mass fraction (Wang et al. 2016b). n-octadecane with copper oxide (CuO) nanoparticle suspensions are also studied for development of melting interface, and melting fraction under constant heat supply conditions. The thermophysical properties are amplified with an increase in nanoparticle concentration up to a specific percentage. Above that limit, there is an adverse effect due to increase of viscosity, agglomeration, and precipitation (Cascetta et al. 2014).

Nanoparticle enhanced phase change material (NePCM) is studied to analyze the copper nanoparticles sizes (diameter of 2 and 5 nm) suspended in water, as the particle size reduces, the interface morphology changes from uniform to the non-uniform dendritic structure during the solidification process. By reducing the size of the nanoparticles, solidification time is reduced due to the enhancement of thermal conductivity (Hasadi 2013). A mixture of water and copper nanoparticles possesses a high heat release rate compared to the conventional PCMs, and its high thermal conductivity makes it efficient

material for TES applications (Khodadadi and Hosseinizadeh 2007). To reduce the melting and solidification time of PCM (paraffin) by mixing alumina nanoparticles, and the time saving of 8 to 20% by adding 3 to 8% volume. Alumina nanoparticles initiate PCM to perform better and result faster solidification rate (Mahdi and Nsofor 2016).

To improve the heat transfer rate, spherical encapsulation arrangement is made in a thermal storage tank using CPCM (a mixture of 0.4% copper nanoparticles, and 99.6% of erythritol). The thermostatic oil bath and CPCM sealed in the balls. The results show the influence on heat dissipation rate through phase change balls, and the interfaces are moved during the heat rejection process (Zhang et al. 2016). To understand the solidification and melting process for CPCM, which is encapsulated inside cylindrical enclosures, the transient interface positions are located, and complete phase change time is predicted for solidification and melting processes. The heat generation delays the solidification, and accelerates the melting process. The heat generation increases at the time of the phase change process due to the increase in thermal conductivity of PCM. Addition of nanoparticles decreases the phase change process; it leads to accelerate the heat diffusion within the NePCM (Bechiri and Mansouri 2016). To analyze the TES capacity, a numerical transport model of porous media and phase change model of thermocline bed is developed. The packed bed has shown enhancement in the energy storage capacity, heat rejection efficiency, and discharging time with an increase in CPCM concentration (Lu et al. 2014). Two methods of thermal storage are given as Cascade Latent Heat Storage (CLHS) and Non-Cascade Latent Heat Storage (NLHS) (Medrano et al. 2010). The CLHS utilizes the phase change process more effectively compared to NLHS at uniform outlet temperature with salt, it achieves high storage capacity. To enhance the thermal conductivity of CPCM, metallic foam and metallic sponge are mixed, and different cooling rates are used under unsteady state conditions. The additives also enhances the thermal conductivity of CPCM (Zhang et al. 2014). Erythritol is a potential material for TES application, but the thermal conductivity is relatively low. Expanded graphite (EG) is added by using direct contact synthesis method. The performance is also evaluated and found enhanced thermal conductivity of the composite with an adverse effect on latent heat capacity. Addition of 4

wt% of EG increased thermal conductivity by 2.5 times, and specific heat capacity is reduced by 2.59%. The investigation reveals a reduction of 16.7% melting time but solidification time remains the same (Gao et al. 2017).

Compared to salt hydrates, the organic PCMs have low volumetric TES capacity. Several experiments are carried out to investigate paraffin wax embedded with aluminum powder. The results have shown 60% reduction in charging time after addition of aluminum powder (Mettawee and Assassa 2007). For enhancing thermal storage density of paraffin (n-docosane) EG is the suitable material to obtain form-stable CPCM. Influence of EG is studied for thermal conductivity enhancement using the transient hot-wire method. Latent heat thermal energy storage (LHTES) characteristics of paraffin, melting time, melting temperature and latent heat capacity is investigated with the help of DSC analysis. The paraffin/EG CPCM with the mass fraction of 10% EG shown the most favorable results (Sarı and Karaipekli 2007). Single and multi-walled carbon nanotubes, carbon blacks, exfoliated graphite nanoplatelets with high conductivity are used to prepare CPCMs at low loading levels. The results influences exfoliated graphite nanoplatelets (xGnP-1 and xGnP-15) in paraffin wax to provide high thermal conductivity and stability with high aspect ratio, low interface density, and better orientation (Xiang and Drzal 2011).

Two different paraffins namely, docosane and hexacosane with melting temperature of 317.15 and 329.45 K are investigated for TES application (Alkan 2006). Sulfonation method is done at three different mole percentage for increasing the LHTES capacity, it found that the samples are absorbing and dissipating more energy than the pure paraffin. Sulfonation method is also suitable for enhancing LHTES capacity of paraffins. Experimental investigation of the TES capacity and discharging efficiency of d-mannitol and hydroquinone is done. The working fluid used is thermal oil with a working temperature of 373 to 673 K (Oró et al. 2012). For the same operating conditions, TES of d-mannitol is greater than that of hydroquinone.

Modification can be done in design by providing fins on the rectangular enclosure of PCM because it reduces the melting time, and increases total heat transfer rate with the number of fins. The inverse effect is also seen while the wall temperature raises (Kamkari and

Shokouhmand 2014). Paraffin wax contains a straight chain of hydrocarbons (>75%) and a small amount of branching. Commercially available waxes may range about 8–15 carbon-number with a volume shrinkage less than 12% during freezing (Demirel and Öztürk 2006). Beeswax of the honey bee is a complex mixture of long-chain alkanes, alkenes, monoesters, diesters, hydroxy-monoesters, and fatty acids which can be utilized for similar applications (Jackson and Eller 2006). The thermal storage unit (TSU) is modeled with beeswax and copper helical coils are inserted for heat transfer enhancement. Series of charging/discharging cycles are carried out, it is shown that beeswax is the best naturally available PCM, which can be used for low-temperature TES applications (Dinker et al. 2017).

2.4 ENHANCEMENT OF THERMOPHYSICAL PROPERTIES OF CPCM USING NUMERICAL ANALYSIS

The numerical investigation is carried out for thermal stability, supercooling, corrosion test, and reliability of inorganic hydrated salt ($Ba(OH)_28H_2O$) with copper as nano additives (Lv et al. 2016). The results have shown good thermochemical stability even after 300 thermal charging /discharging cycles. Enthalpy of fusion and heat-storing capacity in both solid and liquid phases of $LiNO_3$, $NaNO_3$, and KNO_3 is prominently better (Takahashi 1988). Out of these, sodium nitrate ($NaNO_3$) metal matrix possessed high thermal conductivity, good mechanical properties, and high surface area. The heat transfer coefficient of CPCM is enhanced up to 28 times, and heat conduction, as well as both melting and solidification time duration, is reduced. The porosity of the copper matrix enhances the conductivity of composite materials (Li and Wu 2014). Heat transfer enhancement and energy storage performance of CPCM can be achieved with CuO nanoparticles by adding 0 - 4 vol% of CuO nanoparticles in HTF, and 0 – 7 vol% of CuO nanoparticles with PCM (Parsazadeh and Duan 2017).

Energy storage technology balancing mismatch between energy supply and demand during day and night. The air conditioning system combined with ice storage can use during night time for reducing operating costs (Yang et al. 2018a). The overall heat transfer rate is

increased, the convective heat transfer coefficient is suppressed for a high concentration of nanoparticles due to increase in viscosity. TES technology gives substantial energy storage ability with minimum volume requirement at a constant working temperature amid heat storage process (Huang et al. 2014). Thermal energy is the only form of energy which is directly usable thus, thermal energy storage is much significant for the contemporary condition (Fan et al. 2013). Numerical models studied for TES applications by the various researchers are given in Table 2.1 to compare the different parameters.

The addition of high conductivity nanoparticles functions as a nucleating agent to start the solidification process of the nanofluid phase change material (NFPCM), and it reduces the subcooling effect. High thermal conductivity reduces the solidification time by 20.6% than base PCM at a working temperature of $-9\,^\circ$C. The NFPCM shows higher cooling rate in the sub-cooled region (Sathishkumar et al. 2016) and (Teng et al. 2013).

2.5 PLASTIC BASED COMPOSITE PHASE CHANGE MATERIAL STUDIES

Plastics are becoming a vital asset of humanity due to its wide range of applications and feasibility that cannot be easily or economically replaced by other materials (Koushal et al. 2014). Plastic usage is almost unavoidable in the present-day scenario even though it is a major toxic pollutant. To overcome the problem of intrinsic toxicity of polyethylene (plastic), it is possible to modify these materials and use as a TES media. Recycled high-density polyethylene is a low-cost material with a melting temperature of $125\,^\circ$C, and latent heat of 210–220 J/g, which can be used for TES material. To provide more feasibility to the material usage, HDPE is also used with material combinations such as poly lactic acid (PLA), paraffin wax, polyethylene glycol etc. The blending of suitable materials with HDPE phase avoids the risk of leakage problem during phase conversion (Lu et al. 2019).

The effects of nano-additives on thermophysical properties of PCM's are listed in Table.2.2.

Table 2.1: Numerical models studied for TES applications by the various researchers.

Authors	Dimensionality	Geometry	Steady / Transient	Parameters Studied	Observations
Jiji and Gaye (2006)	One	Slab	Steady	Solidification and melting	The dimensionless heat generation parameter should be unity or smaller and solidification and melting solutions are governed by single parameter.
Parsazadeh and Duan (2017)	Two	Cylindrical	Transient	Role of nanoparticles in the HTF and their effects on the melting rate	A regression model is developed for prediction of liquid fraction in the NePCM.
Mahdi and Nsofor (2016)	Two	Cylindrical	Transient	Flow behavior and heat transfer characteristics during solidification of a nano-PCM	The presence of nanoparticles shows increase in volume fraction and amplifies solidification rate.
Das et al. (2016a)	Two	Rectangular	Transient	Melting of graphene-based phase change nano-composites	The inclusion of graphene nanosheets decreases the melting time by enhancing thermal conductivity of CPCM.

Lv et al. (2016)	Two	Cylindrical	Transient	Solidification and melting process	Nanoparticles provided good thermal stability.
Das et al. (2016)	Two	Cylindrical	Transient	Solidification and melting process and temperature distribution	2 vol% of graphene, melting time reduces by 41%.
Lu et al. (2014a)	Two	Square	Transient	Energy storage density	The optimal melting point should be equal to the outlet temperature for good heat storage performance.
Lu et al. (2014b)	Two	Cylindrical	Transient	Energy storage performances	The phase change material content increases the phase change layer thickness and discharging time increases.
Wu et al. (2012)	Two	Square	Transient	Melting of PCM	Addition of nanoparticles is an efficient way to enhance the heat transfer in latent heat thermal energy storage system.
Abolghasemi et al., (2012)	Two	square	Transient	Effect of nanoparticles on thermos-physical properties of PCM	The performance of an energy storage unit is directly related to the thermal conductivity of nano-particles.

Delgado et al. (2012)	Two	Circular	Transient	Influence of fluid temperature on wall	A slurry with 10% weight concentration of paraffin improves the convective heat transfer coefficient by 25%.
Kalaiselvam et al. (2008)	Two	Cylindrical	Transient	Solidification and melting process	The solidification time depends on Stefan number and heat generation parameter β, and complete melting time depends on equivalent thermal conductivity.
Khodadadi and Hosseinizadeh (2007)	Two	Square	Transient	Solidification of water/copper nanoparticles.	Increase in thermal conductivity reduces the latent heat of fusion, but heat release rate increased.
Zhang et al. (2016b)	Three	Spherical	Transient	Charging, discharging and thermal profile	Increased bulk density of the CPCM shortens the thermal energy storage time.

Bechiri and Mansouri (2016)	Three	Cylindrical	Transient	Melting and solidification process	The storage efficiency can be higher than 1 for positive heat generation (g > 0), and for negative heat generation (g < 0), the storage efficiency is always lower than 1.
Li and Wu (2014)	Three	Cube	Transient	Phase distribution during melting	Optimizing the porosity and pore density to make effective energy transport.
Hasadi (2013)	Three	Square	Transient	Solidification of water/copper nanoparticles.	The higher thermal conductivity of the colloids, decreases the solidification phase as the particle size decreased.

Table 2.2: Effect of Nano-additives on thermophysical properties of PCMs with different combinations.

Authors	CPCM Combination		Parameter Studied	Observations
	Base PCM	Additives		
Yuan et al. (2019)	Polyethylene glycol (PEG)	functionalization of graphene	Thermal characteristic and thermal response	Phase change temperature and specific heat capacity increased
Li et al. (2019)	Linear low-density polyethylene	α-zirconium phosphates (ZrP),α-zirconium phosphates (OZrP) and organophilic montmorillonite (OMMT)	Heat resistance increase	Distortion temperature enhanced of 16 °C
Putra et al. (2019)	beeswax	Multi-walled carbon nanotubes	Latent heat, sensible heat, melting point, k and thermal cycle up to 300 cycles	Thermal conductivity increased 132%
Saeed et al. (2018)	Form-stable eutectic mixture	Nano-graphene platelets (NGPs)	Thermal conductivity, specific heat and thermal diffusivity	Thermal conductivity increased 102.2% for solid phase and 97.7% for liquid phase, thermal diffusivity increased by 47% for solid phase and 54% for liquid phase.
Parsazadeh and Duan (2017)	Water	CuO Nano particles*	Melting and solidification characteristics	Overall heat transfer rate increased* Melting time reduced*

Gao et al. (2017)	Erythritol	Expanded graphite* (EG)	Thermal characteristic and thermal response	k increased by 2.5 times. Latent heat reduced by 2.59%. Melting time reduced by 16.7%.
Karaipekli et al. (2017)	Eicosane (C20)	Carbon nano tubes (CNTs) (1wt %)	Thermal conductivity (k)	k increased by 113.3%.
Wang et al. (2017)	OP10E (30%)/ water (70%) emulsion	Graphite nanoparticles (5wt %)	Supercooling and k	Supercooling decreases* Enhancement in k*
Jing Yang et al. (2016)	Polyethylene glycol (PEG)	Microcrystalline cellulose and GNPs (5.3 wt %)	k, Shape stability and latent heat of fusion	Good shape stability and Large latent heat of fusion and k enhanced by 463%
Pielichowska et al. (2016b)	Polyurethane	Graphene*	Thermal reliability and chemical stability	Improved*
Wu et al. (2016)	Stearic acid (SA)	EG*	k	k enhanced by 4 times
Yuan et al. (2016)	Palmitic-Stearic Acid (PA-SA)	Graphene nanoplatelets (GnPs) (nano scale) and EG (micro- scale) *	k	k of the CPCM is 2.7 times higher with GnPs and 15.8 times higher with EG.
Saha and Pal (2016)	Epoxy	Graphene oxide and graphene*	Thermal and Mechanical properties	Improved*
Wang and Ling (2016a)	Water	Octadecane*	Thermal storage density (TSD)	Heat Capacity (Cp) reduced with increase in octadecane mass fraction*.
Mahdi and Nsofor (2016)	Paraffin	Alumina nanoparticles (3–8%)	Melting characteristics	Time saving between 8% and 20%.
(Lv et al (2016)	Hydrated salt $Ba(OH)_2 \cdot 8H_2O$	Copper nanoparticles*	Heat transfer rate	Heat transfer efficiency improved*

Wang et al. (2016)	Paraffin (RT 42)	EG Powder (20 wt%)	k and TSD	k enhanced 7.5 times
Xu et al. (2016)	D-Mannitol	EG*	TSD	Improved*
Lee et al. (2016)	Epoxy	Graphene*	Thermal characteristic	Improved*
Jialin Yang et al. (2016)	Paraffin	Copper foam*	Melting characteristics	Metal foam shortens melting time*.
Liu, and Rao (2016)	Paraffin	Kaolin*	k	Thermal storage capacity improved* Heat release rate enhanced (HRR)*
Zhou, and Jin (2016)	Polyethylene glycol	EG*	Thermal properties	Heat storage duration 46.52%, and heat retrieval duration 30.05% enhanced
Liang et al. (2015)	Polydimethylsiloxane (PDMS)	Superoleophilic graphene–nickel foam (PDMS–G–NF) *	Latent heat	The latent heat of CPCM ranges between 42.3–123.41 (kJ/ kg)
Paul, Shi, and Bielawski (2015)	Eutectic mixture of Galactitol (30%) and Manntitol (70%)	Graphite powder and Silver Iodide (0.5 wt %)	Temperature and enthalpy of crystallization	Improved by up to 34%.
Schuller and Lalk (2015)	Sodium nitrate and potassium nitrate (60:40 mole fraction)	Alumina nanoparticle (0.78%)	Specific heat	Enhancement of specific heat by 30.6%
Luo et al. (2015)	Paraffin	EG*	Melting characteristics	Shorten the melting time *

Fauzi et al. (2014)	Myristic Acid (MA)	Palmitic Acid (PA) and Sodium Laurate (SL)*	Thermal properties, chemical stability and thermal performance	Improved*
Ge et al. (2014)	Eutectic salt of Lithium carbonates (43%) and Sodium carbonates (57%) (LiNaCO$_3$)	MgO, Natural graphite flakes and carbon nanotubes (CNTs)*	k and TSD	k = 4.3 (W/m K), TSD = 530 (kJ/kg)
Li and Wu (2014)	Sodium Nitrate (NaNO$_3$)	Porous Copper Matrix*	Heat transfer characteristics	k and HRR enhanced*
Ye et al. (2014)	Na$_2$CO$_3$/MgO	Multi-walled carbon nanotubes (MWCNTs)*	TES, chemical compatibility and thermal stability	Improved*
Yuan et al. (2014)	Aluminate cement paste	Nano-MgO (NM) and Polycarboxylate*	k	k enhanced up to 40.8%.
Zhang et al. (2014)	NaNO$_3$/KNO$_3$	Metallic foam and Metallic sponge*	k	Improved*
Fan et al. (2013)	Paraffin wax	CNTs (S-MWCNTs), long MWCNTs (L-MWCNTs), CNFs, and GNPs (5wt. %.).	k	k enhanced up to 164%.
Hasadi (2013)	Water	copper nanoparticles*	Melting and Solidification characteristics	Melting time Shorten *
Li (2013)	Paraffin was	Nano-graphite (NG)*	k	k enhanced up to 70%.
Youssef et al. (2013)	Clathrate hydrates	Water*	Thermal characteristic	Improved*

Zhong et al. (2013)	Octadecanoic acid (OA)	Graphene aerogel (GA)*	k	k enhanced by 14.
Abolghasemi et al. (2012)	$CaCl_2–6H_2O$	Cu, Al_2O_3 and CuO nanoparticles*	Energy storage unit Performance	Energy consumption of plant reduced by 43 %.
Delgado et al. (2012)	Paraffin	Water*	Heat transfer phenomenon	Enhancement in HRR by 25%.
Jegadheeswaran, et al. (2012)	Hydrated salt	Micro-copper particles*	Thermal characteristic	Improved*
Rao et al. (2012)	n-nonadecane	Water*	TSD	Enhanced TES capacity due to reduced Mobility*.
Shuying et al. (2012)	Paraffin	Copper nanoparticles (1 wt %)	Melting characteristics	Melting time reduced by 13.1%.
Sanusi et al. (2011)	n-Tricosane	Graphite nanofibers (GNFs)*	Solidification and melting time.	GNF shortens solidification time by 61%.
Xiang and Drzal (2011)	Paraffin wax	EG nanoplatelets (xGnP-1 and xGnP-15) *	Thermal characteristic	Improved*
Yavari et al. (2011)	1-octadecanol (stearyl alcohol)	Graphene platelets (4wt %)	k	k increases by 140%.
Sari et al. (2008)	Fatty acid (capric, lauric, and myristic acids)	EG*	charging/discharging characteristics	Charging and discharging rate improved*.
Khodadadi and Hosseinizadeh (2007)	Water	Copper Nanoparticles*	Thermal Characteristic	Enhanced k *, HRR Increased*
Mettawee and Assassa (2007)	Paraffin Wax	Aluminum Powder*	Charging and discharging processes	Charging time reduced by 60%.

* Specific values not available

Recent studies on different combinations of materials focus the development of thermal storage materials on enhancing the overall performance of the TES system. However, their thermophysical properties vary with mass concentrations, thermal conductivity, phase change behavior, heat capacity, and the equivalent thermodynamic response are not investigated extensively (Yan Kou et al. 2019). Low thermal conductivity, poor thermal stability, high flammability, supercooling, corrosiveness, and leakage during phase change processes are confines the feasibility of PCMs (Nazir et al. 2019). The CPCMs based on LDPE, LLDPE, and HDPE blended with soft paraffin wax are investigated, and wax contents influence the melting and solidification characteristics. The waxes are uniformly dispersed in the polymer matrix without any leakage (Molefi et al. 2010).

The scientific community is continuously focusing on improving the thermophysical properties of PCMs for making feasible and commercial. Linear low-density polyethylene and ethylene–propylene–diene terpolymer (EPDM) blend also shown enhanced thermophysical properties and, LLDPE ethylene vinyl acetate (LLDPE/EVA) blends demonstrated reduction in activation energy (da Costa and Ramos 2008) and (Khonakdar 2015). Thermal storability of the composite improves the combination with LLDPE, paraffin wax, and expanded graphite (Sobolciak et al. 2015). Present-day challenge is to tackle the energy issues and pollution due to plastic usage by utilizing the recycled plastics for TES applications.

2.6 RESEARCH GAP

Based on the literature review conducted for enhancement of thermophysical properties, thermal performance evaluation, and effect of nanoparticle addition on melting and solidification characteristics, the following research gaps are explored.

1. There is a need for enhancement in thermophysical properties of traditional PCMs.
2. Carbon-based nanoparticles like Graphene, graphene oxide, carbon nanotubes, fullerene, graphite, graphite oxide, extracted graphite, etc., are significantly enhancing the thermo-physical properties of CPCMs.

3. Composite phase change materials with graphene-based nanoparticle are having greater potential for TES applications.

4. Blending of polyethylene-based phase change materials and nano enhanced phase change materials for the future TES applications.

2.7 SUMMARY OF THE LITERATURE REVIEW

This literature review presents an in-sight study on the available thermal energy storage technology with composite phase change materials. It is seen that the thermophysical properties enhancement is studied by characterization of CPCM by selecting different base PCMs and some novel additives. The differential scanning calorimeter, thermogravimetric analysis, X-ray diffraction, and scanning electron microscopy are used to study the thermal properties and topography (the study of shape and features) of the CPCM. The numerical models with different material compositions are investigated at different operating conditions and compared with experimental results. Recent patents on thermal storage systems have also promoted TES technology.

2.8 CLOSURE

A detailed analysis of the literature is carried out in this chapter. Essential, as well as parametric issues, are observed through characterization, numerica, and experimental studies in detail. Comparison of different material combinations and compatibility is also listed. Based on the research gaps, objectives are identified.

CHAPTER 3

MATERIALS AND METHODS

3.1 INTRODUCTION

To study the influence of nanoparticle concentration on thermophysical properties, thermal performance evaluation, and thermal storage characteristics of composite phase change materials are developed, and different methods are used to characterize these composites. To make use of waste plastics as recycled composites and to study the influence on environment preservation and better substitute for thermal energy storage application using waste raw material prepared at low cost. Characterization is also carried out to analyze the relationship between the base material and the nano additive concentration on thermophysical properties.

3.2 MATERIALS USED FOR THE STUDY

Thermophysical properties of base materials can be enhanced by various methods such as, inserting fins, metal matrices, and blending high-conductivity particles. Thermophysical properties of nanoparticles based composite materials also increases with nanoparticle concentration. Different base materials and nano additive materials are used to study the different parametric effects, and to evaluate the thermal storage capacity.

3.2.1 Materials Used in Numerical Simulation

Paraffin wax, copper nanoparticles, and nano Al_2O_3 with an average particle size of 10 to 20 nm are used for improving the thermophysical properties of the base (paraffin wax) material, properties of all the materials are listed in Table 3.1.

Table 3.1: Properties of paraffin wax, copper nanoparticles, and Al_2O_3.

Sl.no	Properties	Base phase change material	Nano additives	
		Paraffin Wax	Copper	Al_2O_3
1	Density (kg/m^3)	$\dfrac{750}{0.001(T-319.15)+1}$	8954	3600
2	Specific heat (J/kg K)	2890	383	765
3	Thermal conductivity (W/m K)	0.21 if T < Tsolidus 0.12 if T > Tliquidus	400	36
4	Viscosity (Ns/m^2)	$0.001 \times e^{\left(-4.25+\frac{1790}{T}\right)}$	-	-
5	Thermal expansion coefficient β (1/K)	5×10^{-4}	1.67×10^{-5}	12.66×10^{-6}
6	Latent heat (J/kg)	173400	-	-
7	Solidification temperature (K)	319	-	-
8	Melting temperature (K)	321	-	-

The intermediate state between solidus ($T_{solidus}$) and liquidus ($T_{liquidus}$) temperatures represents the transition phase during the melting of CPCM. The density, specific heat capacity and latent heat of the composite phase change materials are defined as per the correlation is given by Khodadadi and Hosseinizadeh 2007. Same correlations are considered for all parametric analysis carried out in the present work.

$$\varphi = \frac{T - T_{solidus}}{T_{liquidus} - T_{solidus}}$$ (3.1)

$$\rho_{cpcm} = \varphi \rho_{np} + (1-\varphi)\rho_{pcm}$$ (3.2)

$$Cp_{cpcm} = \frac{\varphi(\rho Cp)_{np} + (1-\varphi)(\rho Cp)_{pcm}}{\rho_{cpcm}} \qquad (3.3)$$

$$L_{cpcm} = \frac{(1-\varphi)(\rho L)_{pcm}}{\rho_{cpcm}} \qquad (3.4)$$

$$\mu_{cpcm} = 0.983 e^{(12.959\varphi)} \mu_{pcm} \qquad (3.5)$$

$$k_{cpcm} = \frac{k_{np} + 2k_{pcm} - 2(k_{pcm} - k_{np})\varphi}{k_{np} + 2k_{pcm} + (k_{pcm} - k_{np})\varphi} k_{pcm} + 5\times10^4 \beta_k \varsigma \varphi \rho_{pcm} Cp_{pcm} \sqrt{\frac{BT}{\rho_{np} d_{np}}} f(T, \varphi) \qquad (3.6)$$

Where B= 1.381×10^{-23} (J/K) is Boltzmann constant and β_k =8.4407(100φ) - 1.07304,

f (T, φ) = $(2.8217 \times 10^{-2} \varphi + 3.197 \times 10^{-3}) \frac{T}{Tref}$ +$(-3.0669 \times 10^{-2} \varphi - 3.91123 \times 10^{-3})$

Where T_{ref} is the reference temperature =273 K, and ζ is the correction factor and its value are same as the value for liquid fraction β.

3.2.2 Materials Used in Characterization and Experimentation

(a) Description of Linear Low-Density Polyethylene (LLDPE)

Linear low-density polyethylene of material code JLL36RA045 is purchased from Reliance Industries Limited, Product Application & Research Center (PARC), Gujarat. LLDPE is a linear polymer (polyethylene), with enough numbers of short branches made by copolymerization of ethylene with longer-chain olefins. The density of the LLDPE is 928 kg/m^3 (ASTM D1505) and melt flow index (MFI) 25.00 g/10 min (ASTM D1238). It is a polymer, inexpensive, adaptable, which is used in different forms.

The LLDPE properties enhancement is of much importance to extend its applicability. In this study, LLDPE-functionalized graphene (f-Gr) nanocomposites are prepared by using twin-screw extruder equipment with an injection machine. The LLDPE properties, thermal stability, and the impact of f-Gr blending on thermophysical properties are studied. The base material used is LLDPE, as shown in Figure 3.1 (a).

(b) Description of Carboxyl Functionalized Graphene (f-Gr)

Carboxyl Functionalized Graphene (ADG-COOH, purchased from Ad-Nano Technologies Private Limited, India) is blended to enhance the performance of CPCM matrix. The material specifications of f-Gr are of purity 99%, COOH ratio-22-24%, surface area ~250 m^2/g, and the number of layers 1-4. The functionalized graphene with thermal conductivity ~5000 W/mK, upon blending it enhances the thermophysical properties of resulting material. Functionalized Graphene is clearly visible in Figure 3.1 (b).
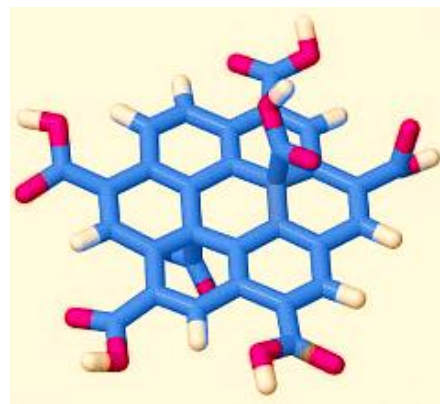
(a)   (b)

Figure 3.1**:** Materials used (a) Linear low-density polyethylene (b) Functionalized Graphene.

3.3 METHOD OF MATERIAL PREPARATION AND CHARACTERIZATION

In the present work, Linear low-density polyethylene and carboxyl functionalized graphene are used to prepare the composite phase change materials. CPCMs (plastic-based composites) are prepared with different concentrations of nano additives such as 1, 3, 5% and these are referred to as CPCM-1, CPCM-2, and CPCM-3.

3.3.1 Composite Phase Change Materials Preparation using Twin screw extruder

LLDPE granules are used and before processing 0.4 g of phenolic stabilizer is also mixed for 1 kg of LLDPE to avoid the degradation during high-temperature processing. In the

extrusion process, the material transforms physio-chemically, and it converts the viscous polymeric media into structured products under precise maintained conditions.

A customized homemade co-rotating, twin-screw extruder (Screw diameter 29.7 mm, diameter ratio (d_o/d_i) 1.71, barrel to screw clearance 0.15 mm, screw to screw clearance 0.50 mm, maximum drive power 50 kW, maximum screw speed 1200 rpm, specified nominal torque/shaft 200 Nm, output 50-100 kg/h) is used to prepare the CPCMs. It contains two interlinking's, co-rotating screws mounted on shafts in a closed container. The wide range of flexibility in design modification makes it applicable to a variety of applications. The complete process can be illustrated from figure 3.2, which shows block diagram of the twin-screw extruder.
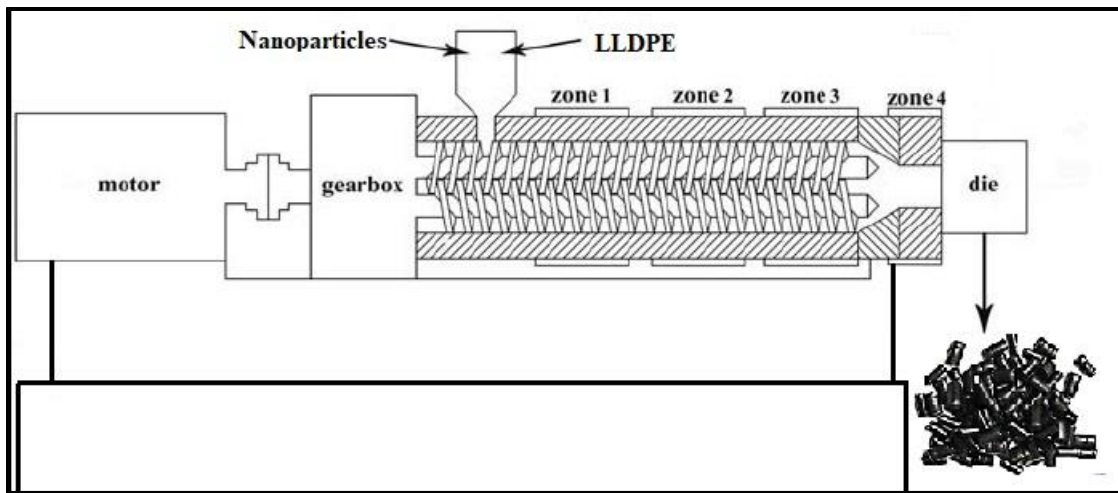
Figure 3.2: Schematic diagram of the twin-screw extruder.

Twin-screw extruder also performs various activities such as transportation, compression, mixing, shearing, heating, and cooling with better flexibility. The melting temperature is set to 200℃ and the twin-screws are rotating with 60–80 rpm speed, with the applications of constant shear force. The main advantage of interlinking co-rotating twin screw extruders is their outstanding mixing ability which converses excellent characteristics to the products and adds substantial importance to the processing units. The screw extruder uses the raw material in different forms such as, solids (powders, granulates, flours), liquids, slurries and gases. Plastic compounds chemically modified polymers are some of the end products of this process.

The preparation of CPCM using LLDPE and f-Gr where LLDPE is base material and f-Gr is dispersed into three different concentrations 1.0, 3.0, and 5.0 wt% and referred as CPCM-1, CPCM-2, and CPCM-3 respectively. LLDPE and f-Gr are mixed in the dry state at room temperature, and it is transferred to the extruder and allowed to mix for 10 min. Figure 3.3 shows composites prepared are (a) LLDPE, (b) CPCM-1, (c) CPCM-2, (d) PCM-3.

| (a) | (b) | (c) | (d) |
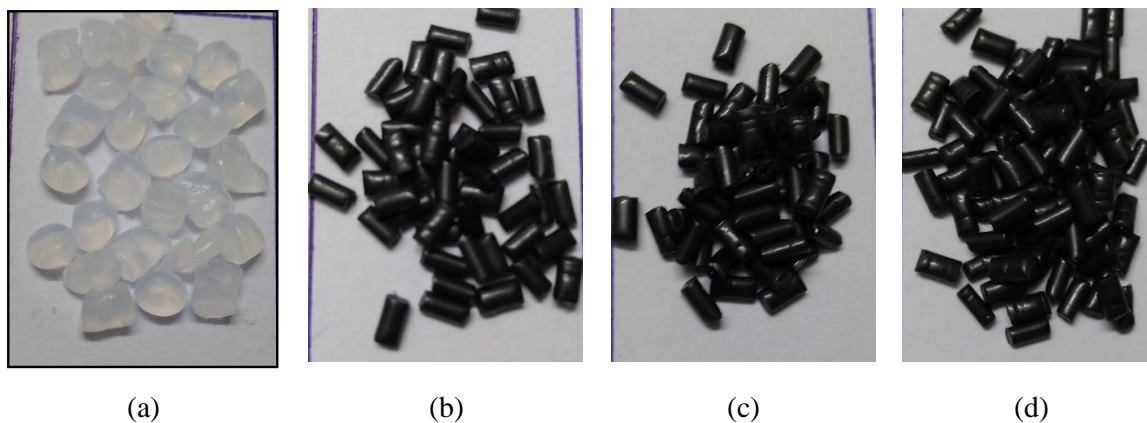
Figure 3.3: Composites prepared (a) LLDPE, (b) CPCM-1, (c) CPCM-2, (d) PCM-3.

3.3.2 Characterization of Composite Phase Change Materials

The prepared CPCMs are examined in this section using various methods for ensuring the thermophysical property enhancement such as Fourier transform infrared spectroscopy (FTIR), scanning electron microscopy (SEM), differential scanning calorimetry (DSC) analysis. The FTIR analysis (Jasco FTIR 4200 series) is used for finding the carboxyl group functionalization. The SEM (JEOL Scanning Electron Microscope with EDS) study is used to understand the morphological structure variations and DSC analysis is used to study the thermophysical properties of the CPCMs. The DSC Model used is METTLER-TOLEDO DSC1 with mW range of heat flow, which also provides phase transitions, such as melting, glass transitions, or exothermic decompositions. Thermal properties of CPCMs are also measured by DSC analysis at a heating rate of 10℃/min between the range of 25-250℃. The latent heat, melting temperature, and crystallization temperature of CPCMs are obtained from the DSC analysis curves.

3.3.3 Flow Chart of Material Preparation and Experimentation

Figure 3.4 shows the complete procedure of material preparation, characterization and experimentation carried out in the present study. The materials used and methods adopted for different analysis carried out to evaluate different properties of the prepared composite phase change materials. The procedure starts from melt mixing the base material and nano additive, by melt mixing CPCMs are prepared. Different characterization methods such as SEM, DSC are conducted to affirm proper dispersion, and to evaluate the thermophysical properties. These obtained thermophysical properties are considered for numerical investigations carried out to estimate the thermal storage capacity and thermal performance. Same materials are used to conduct the experiment for charging/ discharging time and thermal performance evaluation. By comparing these numerical and experimental results best suited thermal storage material can be suggested for thermal storage applications.
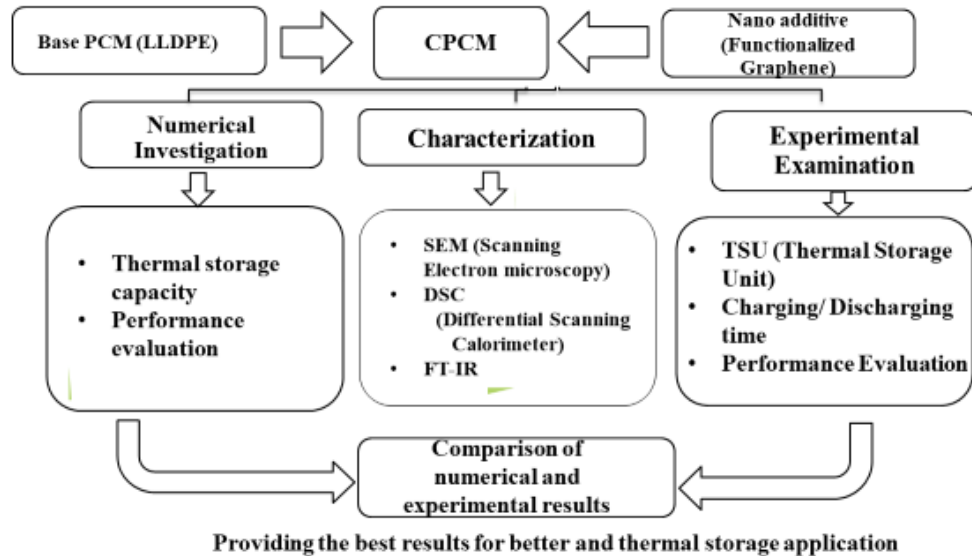
Figure 3.4: Flowchart of material preparation, characterization, and experimentation.

3.4 NUMERICAL METHODOLOGY

The square and rectangular geometries are modeled using pre-processing software ICEMCFD 16.0. The fine quality mesh is generated for good results, near the boundaries fine structured mesh is generated to compensate computational domain. Fine mesh is generated in the rest of the domain to minimize the computational time. The meshed model is imported to FLUENT 16.0 for solving the governing equations with boundary conditions. In the present work, PRESSURE BASED method is adopted for solving governing equations, and all the thermophysical properties of CPCM are defined by using User-defined functions (UDF). FIRST ORDER upwind differencing scheme is used, and PRESTO scheme is adopted for pressure correction formula. The under-relaxation factors for pressure correction, velocity components, and thermal energy are 0.3, 0.5, and 1.0 is considered. Convergence criteria are 10^{-6} for continuity and momentum equations and 10^{-9} for energy equation. Enthalpy-porosity technique is used to study the melting and solidification processes.

3.4.1 Governing Equations

The two- dimensional governing equations are used in this chapter as follows. Boussinesq term is considered for natural convection flow, to achieve faster convergence. The fluid density is defined as a function of temperature. This model treats density as a constant value in all solved equations, except for the buoyancy term in the momentum equation.

Continuity equation

$$\frac{\partial u}{\partial x} + \frac{\partial v}{\partial y} = 0 \tag{3.7}$$

x - Momentum equation

$$\frac{\partial u}{\partial t} + u\frac{\partial u}{\partial x} + v\frac{\partial v}{\partial y} = -\frac{1}{\rho}\frac{\partial p}{\partial x} + \frac{\mu}{\rho}\left(\frac{\partial^2 u}{\partial x^2} + \frac{\partial^2 u}{\partial y^2}\right) \tag{3.8}$$

y - Momentum equation

$$\frac{\partial v}{\partial t} + u\frac{\partial v}{\partial x} + v\frac{\partial v}{\partial y} = -\frac{1}{\rho}\frac{\partial p}{\partial y} + \frac{\mu}{\rho}\left(\frac{\partial^2 v}{\partial x^2} + \frac{\partial^2 v}{\partial y^2}\right) + g\beta\left(T - T_{ref}\right)$$

(3.9)

Energy equation

$$\frac{\partial T}{\partial t} + u\frac{\partial T}{\partial x} + v\frac{\partial T}{\partial y} = \alpha\left(\frac{\partial^2 T}{\partial x^2} + \frac{\partial^2 T}{\partial y^2}\right)$$

(3.10)

Where ρ is density, μ is the viscosity of the CPCM, p is pressure, g is gravity, β is coefficient of volumetric expansion, T and T_{ref} are medium temperature and reference temperature respectively.

3.5 EXPERIMENTAL PROCEDURE FOR THERMAL PERFORMANCE EVALUATION

Initially, CPCM has filled in the thermal storage unit in the experiment, same as numerical analysis. All thermocouples are inserted at appropriate positions, and the top face is closed with transparent glass to visualize the melting and solidification processes. A 250 W heat supply is set by adjusting the current and voltage in the voltage regulator unit. The complete set up is perfectly insulated by packing with glass wool, and all thermocouples are connected to the calibrated data acquisition system (DAQ). The DAQ is connected to the computer unit for data collection and analysis.

3.6 COMPONENTS OF EXPERIMENTAL SETUP

In the present experimental setup contains seven different components as shown in Figures 3.4 (a)-(d)

(i) Power supply

The first component of the TES system is the power supply which is the primary source for running all the equipment. AC supply of 230 V 50 Hz, is used but it can be changed to the required voltage range for running different types of devices.

(ii) Voltage Regulator unit

Adjustable DC power supply of AC220V 50/60 Hz input, Voltage (0-150) VDC, current (0-2) A, maximum power 300W (PROXIM ASIA INC) voltage regulator is used to control the supply, as the voltage and current set to provide the required wattage (as shown in Figure 3.4 (a)).

(a) Voltage regulator
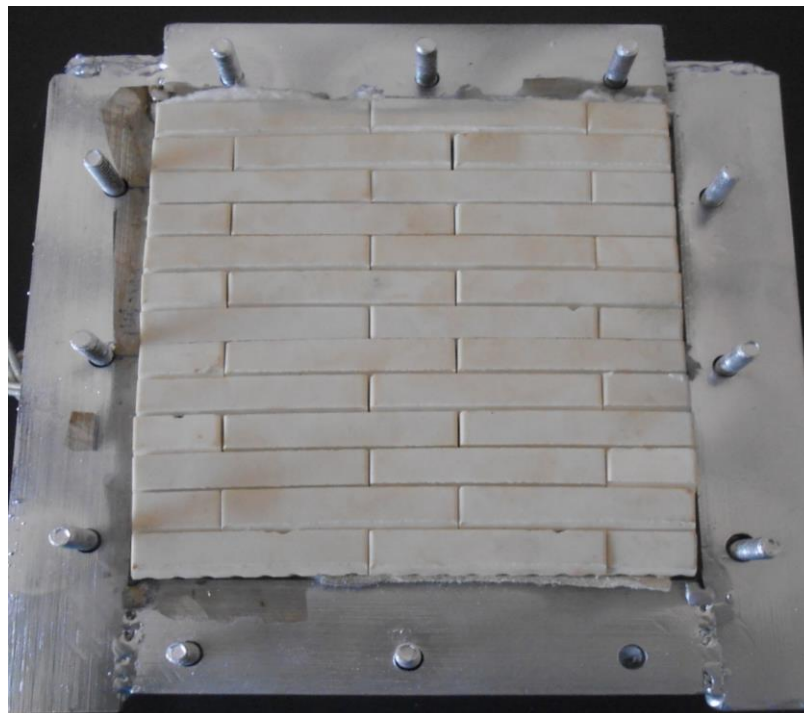
(b) Electric ceramic heater
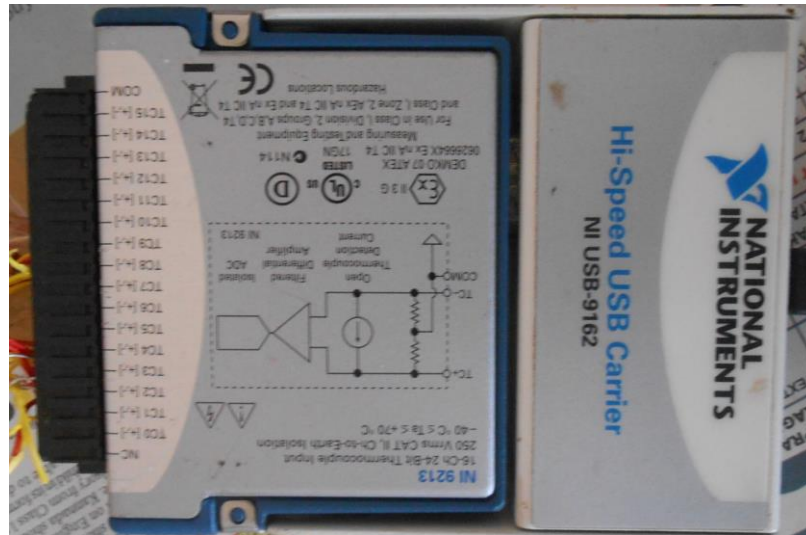
(c) Data acquisition system
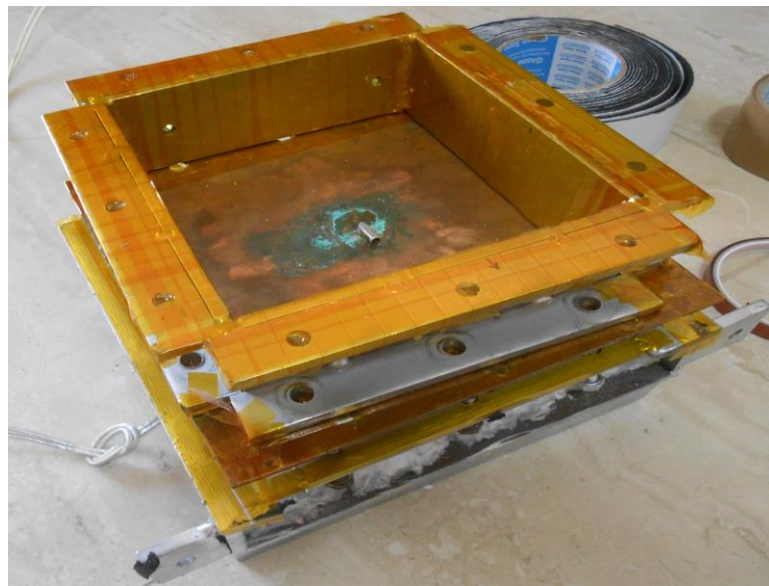
(d) Thermal storage unit.

Figure 3.5: Experimental Setup components (a) Voltage regulator (b) Electric ceramic heater (c) Data Acquisition system (DAQ) and (d) Thermal storage unit.

(iii) Electric Ceramic Heater

A ceramic heating plate (Pragati Ceramics, Gujarat, India) is used to provide uniform surface temperature up to $800°\,C$, and the maximum heating capacity of the heater is 1 kW.

43

The heating rate is varied by the voltage regulator, and large grooves can heat the plate uniformly with low watt density, and high wattage per square inch of the radiating surface. The heating elements are fixed in ceramic in different shapes, and size depends on the requirements. The heater plate is widely used from low to high voltage due to its cost-effective, energy-efficient and environment-friendly in nature (as shown in Figure 3.4 (b)).

(iv) Data Acquisition system (DAQ)

The NI 9213 is used to record and analyze the experimental data, the NI 9213 reads, and it transfers thermocouple data to the mixed-signal test systems with greater feasibility (as shown in Figure 3.4 (c)).

(v) Thermal storage unit

The thermal storage unit of 150 mm $\times$ 50 mm $\times$ 150 mm in (x, y, z) dimensions are fabricated using different size of stainless-steel plates. In this unit, four holes are provided for thermocouples from two opposite sides, and it is confirmed that there is no leakage from any part of the unit. The top face is open and closes according to the requirement of replacing the thermal storage material and clean up the unit for a different set of experiments. The complete TSU is well insulated with glass wool material for providing the adiabatic boundary conditions (as shown in Figure 3.4 (d).

(vi) Thermocouples

The thermocouples used in the experiment are customized with k-type temperature sensors of pen type assembly. The dimensions of thermocouples are 3 mm in diameter, 70 mm with 2 m cable length and the temperature range is 0-800° C. The total number of thermocouples are seven, and namely T_1, T_2, T_3, and T_4 indicates temperatures at different locations of the thermal storage medium, T_5 and T_6 indicates heating base wall and top wall temperature and T_7 shows the surrounding temperature respectively. All thermocouples are directly connected to the DAQ unit for further recording and computing.

(vii) Computer unit

Dell Inspiron 15 3543 model laptop (CPU: Intel Core i3-5005U, GPU: Intel HD Graphics 5500 and RAM: 4GB DDR3) with LabVIEW 2017 is used for recording and computing the data coming from the DAQ unit.

3.7 CLOSURE

This chapter provides comprehensive details of materials used in the numerical simulation, characterization and experimental studies, it elaborately discusses the methods adopted for different analysis such as Fourier transform infrared spectroscopy (FTIR), scanning electron microscopy (SEM), and differential scanning calorimetry (DSC). Preparation of composite phase change material is also discussed in detail.

CHAPTER 4

PARAMETRIC ANALYSIS OF THERMAL STORAGE SYSTEMS THROUGH NUMERICAL STUDY

4.1 INTRODUCTION

Parametric analysis is carried out in this chapter by varying different parameters such as nanoparticle concentration, geometrical orientation, and domain geometry to analyze the thermal performance. First, the effect of copper nanoparticle concentration in a bounded square domain is studied in detail. Next, the study is extended to two different domains such as deep and shallow domain, respectively. Then, the effect of different orientations and different wall heatings are studied, and three different domains such as square, pentagon, and hexagon domains are also analyzed.

4.2 EFFECT OF NANO ADDITIVES ON THERMOPHYSICAL PROPERTIES OF CPCM

4.2.1 Two- Dimensional Computational Model Description

A bounded domain of square geometry (25 mm × 25 mm) shown in Figure 4.1 is considered to study the thermophysical properties of composite phase change material (CPCMs). The analysis is carried out from zero % (Base PCM) to 10 % of nanoparticles to observe the gradual variation and response of the base material. The study is carried out for four different composition of nanomaterial randomly such as 2, 5, 8 and 10% addition. Unit quantity (1 kg) of total mass is considered for the study and it is obvious that for 2, 5,8 and 10 % copper nanoparticles indicate 20, 50, 80 and 100 grams respectively and PCM mass will be 980, 950, 920 and 900 grams. To achieve the results assumptions are made. Same assumptions are considered for all the numerical simulations presented in this

chapter. (i) The working fluid in the melting phase is Newtonian fluid and the flow is incompressible. (ii) The flow in the melting phase is laminar with negligible viscous dissipation rate. (iii) The thermophysical properties of CPCM are purely temperature-dependent. (iv) The change of volume during phase conversion is negligible, and the CPCM solid is in contact with the cold wall at all the times. During the phase change process, the PCM expands as it is converts from solid to liquid phase, practically there will be no space for the PCM to expand. The top and base walls are insulated, and vertical walls are kept isothermal. The left wall is maintained at 330 K, the right wall is at 300 K, and the initial temperature of CPCM is chosen as 300 K. The isothermal boundary condition is imposed to practical application of PCM where most of the cases isothermal condition need to be maintained.
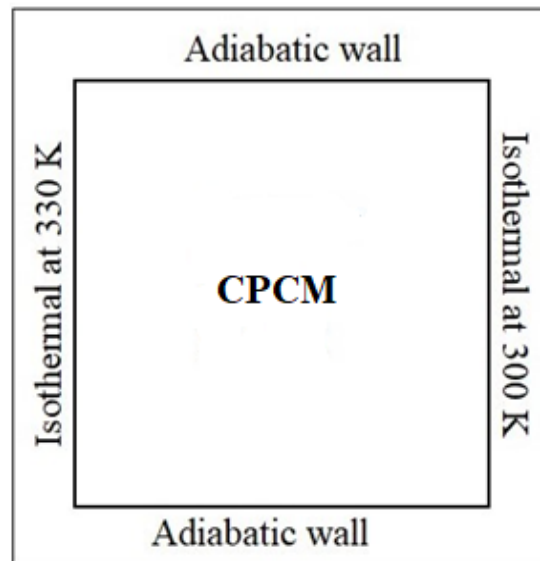
Figure 4.1: The square geometry of the computational model with boundary conditions.

4.2.2 Validation of Square Domain

To authenticate the validity of present results, existing results of Khodadadi et al. (2007) in a square geometry is compared for two different time durations. The boundary conditions imposed are left and right walls are isothermal at 330 K and 300 K, and top and bottom walls are insulated. Figure 4.2 shows the streamline patterns of present and existing results of Khodadadi et al. (2007). It is observed that as time increases the melting

fraction also increases. The streamlines patterns of 500 and 1000 sec are found to be similar, and matching with existing results.

(a) 500 sec	(b) 500 sec
(a) 1000 sec	(b) 1000 sec
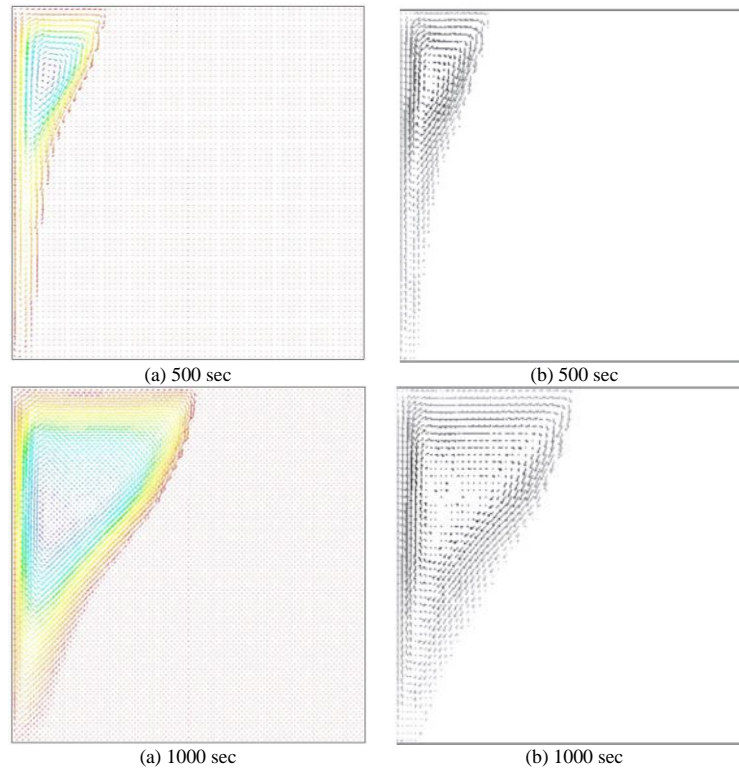
Figure 4.2: Streamline patterns (a) Present results and (b) results of Khodadadi et al (2007).

4.2.3 Variation of Mass Fraction (φ) during the Melting Process

Figure 4.3 shows the variation of mass fraction during the heating process with different nanoparticle concentrations in the square domain. The contours show the melting fraction of CPCM with 2, 5, 8, and 10 % blending. For 2 % blending, improper melting is observed with partially molten patches in the molten region, which represents an intermittent phase of solid-liquid is called as mushy zone. The heat transfer rate at higher percentage loading is faster than lower percentage loading, which shows that Cu nanoparticles accelerate the melting process. The melting rate is high at adjacent to the top portion of the domain due to the influence of natural convection in the liquid region. At the beginning of the melting phase, the melting front movement is slow due to the buoyancy effect. Initially, melting

front is parallel to hot wall which indicates the conduction dominated melting process, as time proceeds melting front gradually picks up a typical shape due to convection dominated melting process.
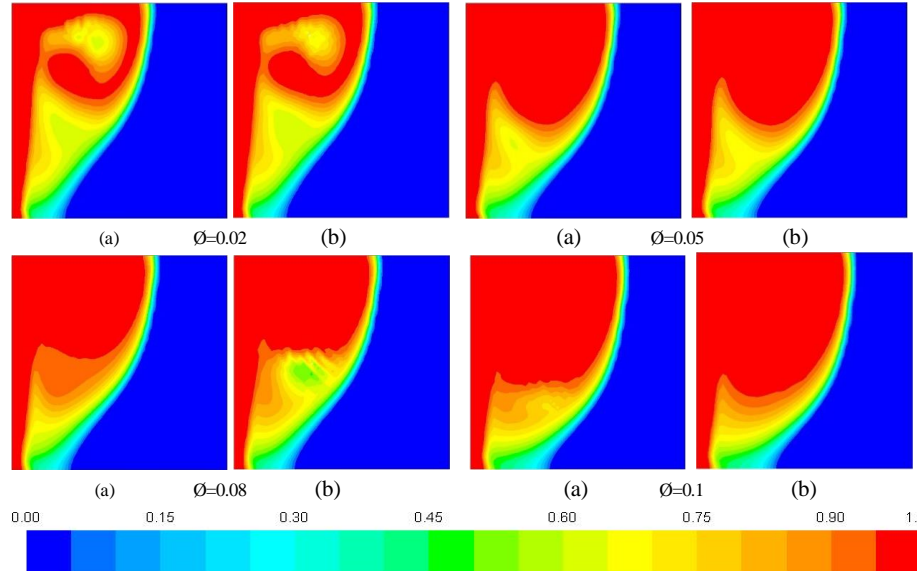
Figure 4.3: Variation of mass fraction during the heating process in a square domain with different nanoparticle concentrations at (a) t = 500 and (b) t =1000 sec.

The interface moves quickly close to the upper portion of the domain where the liquid is heated by the hot wall, and the melting rate is reduced at the base wall. The liquid inside the domain gets cooled and it reduces the sideways of the interface. With change in time, the temperature gradient in the solid phase built and makes the melting process to slow down. When the nanoparticle percentage loading is increased to 5 %, the mushy patches are disappeared completely, and pure melting is observed. As the loading percentage increased to 10 %, melt front penetration is deeper than the lower percentage loading.

4.2.4 Variation of Temperature during Melting Process

Figure 4.4 shows the variation of temperature during the heating process with different nanoparticle concentrations at different time intervals. The temperature distribution patterns are quite like the melting process when natural convection is completed. The temperature gradient along the hot wall is higher at the bottom region and smaller at the

top region of the domain. An inverse pattern of temperature distribution is seen along with the solid-liquid interface, and the center, top and bottom walls in the solid phase are linear and almost same.
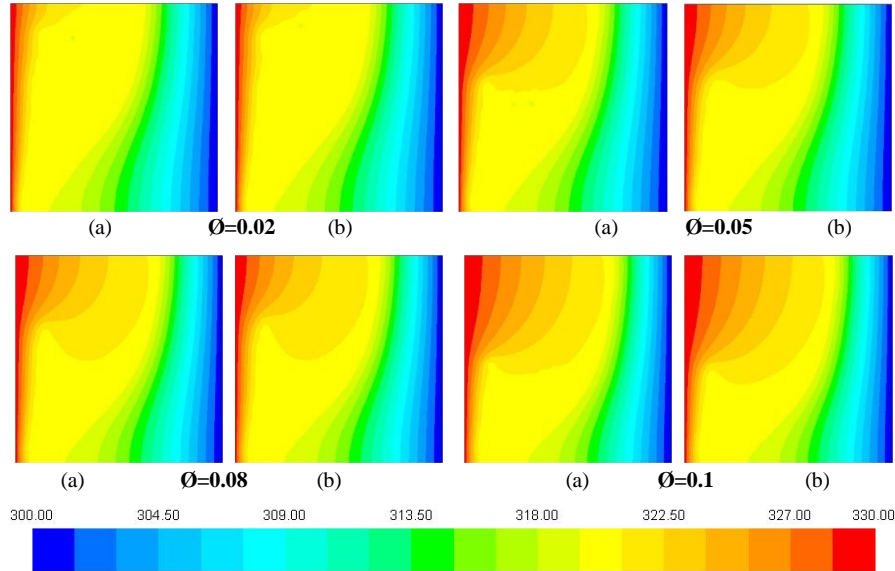
Figure 4.4: Variation of temperature during the heating process in the domain with different nanoparticle concentrations at (a) t = 500 and (b) t =1000 sec.

It is known that natural convection starts to play an essential part in terms of controlling the solidification process at later stages when the temperature gradient in the solid decreases with the expansion of the solid region thickness.

4.2.5 Effect of Nanoparticle Concentration on Thermophysical Properties

Figures 4.5 (a) and (b) shows the variation of thermal conductivity and specific heat capacity with temperature. The thermal conductivity of CPCM increases considerably with increase in loading percentage, and this improvement in thermal conductivity significantly reduces the charging and discharging time and it provides better performance. The dispersion of nano additives carries the heat energy, and drives the melting front, speed directly depends on the percentage loading. Higher viscosity leads to enhanced heat transfer rate and low specific heat, optimum viscosity values are suitable for TES applications.
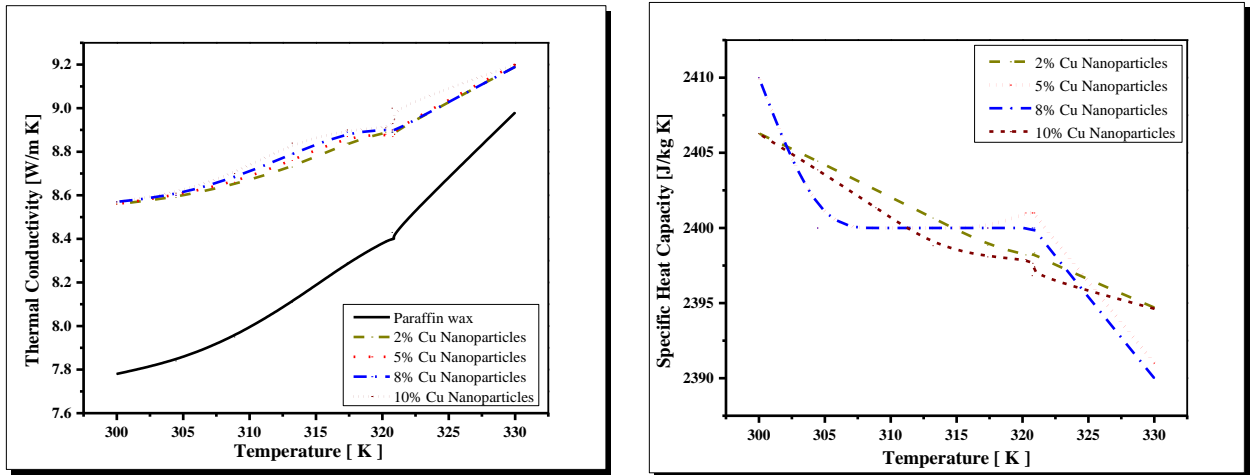
Figure 4.5: Variation of (a) thermal conductivity and (b) specific heat capacity with temperature.

Conduction heat transfer affects the overall solidification and melting processes, and it shows that slow movement of melting front. Nanoparticle addition also enhances the specific heat of CPCM up to certain percentage, and at high loading percentage (10%) the specific heat capacity gets reduced up to 20%, which have an adverse effect (increases the volume requirement) on the TES applications.

4.3 STUDIES OF DEEP AND SHALLOW DOMAIN ON MELTING AND SOLIDIFICATION CHARACTERISTICS

The thermal storage model is extended to deep (100 mm × 150 mm) and shallow (150 mm × 100 mm) domain with constant heat of 500 W supply to top wall heating and cooling. The thermal storage medium used for the investigation is CPCM (a mixture of 98% of paraffin and 2% copper nanoparticles) with enhanced thermophysical properties.

4.3.1 Problem Description

The present model is a bounded rectangular domain with two different orientations, such as deep and shallow domain as shown in Figures 4.6 (a) and (b). Geometrical model of

the domain with different orientations and boundary conditions are studied to analyze the effect of changing the orientation with respect to the horizontal base.
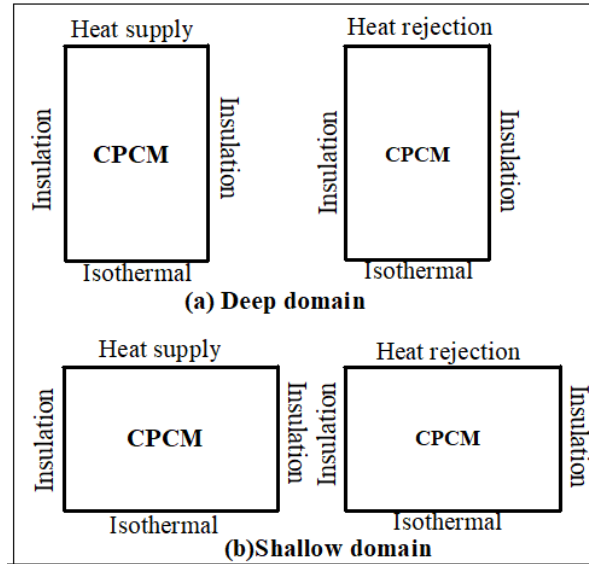
Figure 4.6: Computational domain of (a) deep and (b) shallow geometry with boundary conditions.

The TSM in the present work is a composite phase change material (a mixture of 98% of paraffin and 2% copper nanoparticles) with enhanced thermophysical properties. The boundary conditions imposed are (i) Base wall is maintained isothermal at atmospheric temperature of 300 K, (ii) Both vertical walls are insulated, and (iii) Constant heat is supplied from the top wall of the domain.

4.3.2 Variation of Mass Fraction in Deep Domain

Figures 4.7 (a)-(d) shows the variation of mass fraction during charging and discharging processes in the deep domain. The melting process starts due to the supply of heat from the top surface of the deep domain, as the time progresses melting front moves forward direction and convection current dominates at 500 sec. The constant heat supply intensifies the melting front to travel in the downward direction and starts to develop a convex shape in the domain. At the completion of the melting process, the melt forms a straight line at 2000 sec on the surface of the sub-cooled CPCM, maintained below its

phase change temperature. The solidification process follows the reverse direction, instead of supplying heat is rejected at a constant rate. After 500 sec, the solidification front forms a bulged rectangular shape, shrinks from both ends, as time proceeds size of the bulged rectangle gets reduces towards the center. During the solidification mechanism move near termination, it forms a tiny circle towards the base wall center.
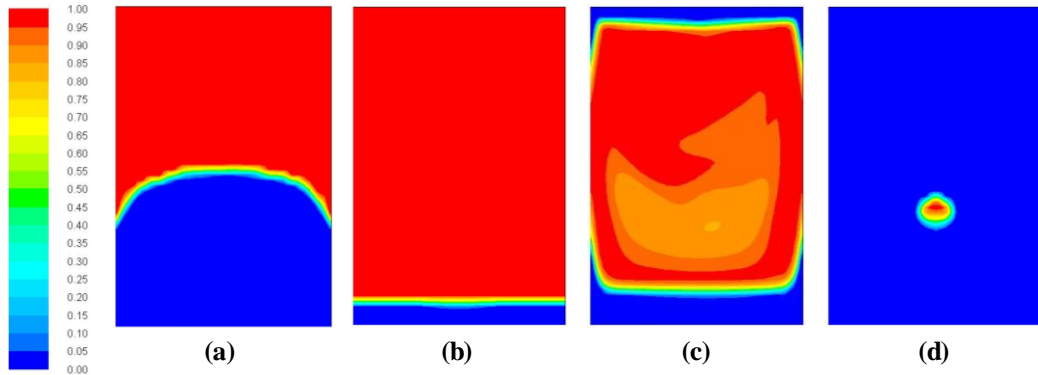
Figure 4.7: Variation of mass fraction during charging at (a) t = 500, (b) t = 2000 sec and discharging process at (c) t = 500, (d) t = 2000 sec in the deep domain.

4.3.3 Variation of Temperature in Deep Domain

Figures 4.8 (a)-(d) shows the temperature distribution during the charging and discharging processes in the deep domain. The temperature over the entire domain is uniform, but drop-in temperature occurs in the melting region.
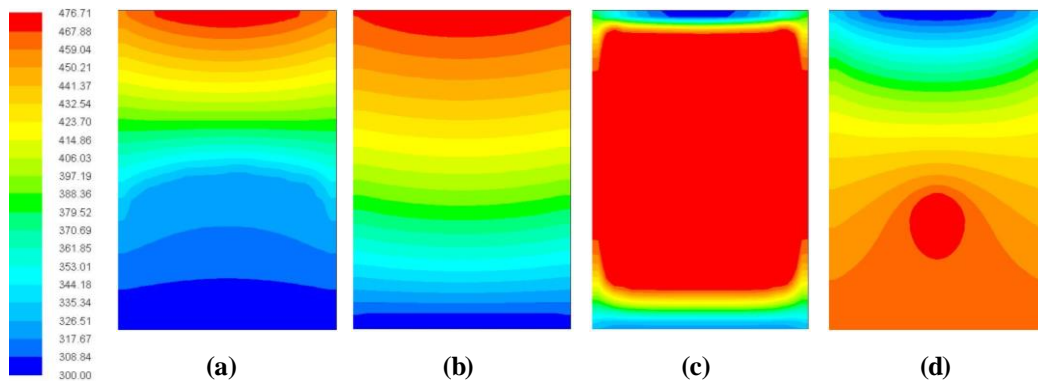
Figure 4.8: Variation of temperature during charging at (a) t = 500, (b) t = 2000 sec and discharging process at (c) t = 500, (d) t = 2000 sec in deep domain.

The reason behind is that the heat energy coming from the melting front is absorbed by the sub-cooled solid CPCM, and allows a small portion to penetrate. At the culmination of the melting process, the temperature distribution is uniform other than the isothermal wall.

4.3.4 Variation of Mass Fraction in Shallow Domain

Figures 4.9 (a)-(d) shows the variation of mass fraction during charging and discharging processes in the shallow domain. The melting progresses like a deep domain with dome-shaped structure at 500 sec, as time proceeds the melting front travels along the insulated vertical walls up to the vicinity of the base wall.
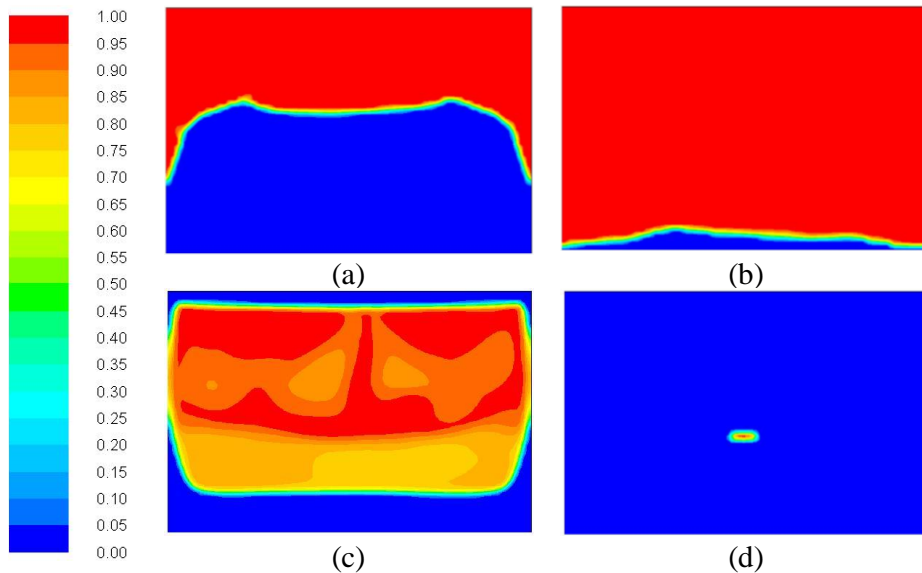
Figure 4.9: Variation of mass fraction during charging at (a) t = 500, (b) t = 2000 sec and discharging process at (c) t = 500, (d) t = 2000 sec for shallow domain.

4.3.5 Variation of Temperature in Shallow Domain

Figures 4.10 (a)-(d) shows the temperature distribution during charging and discharging processes in the shallow domain. At the completion of the melting process, the temperature is distributed uniformly all over the surface. For the discharging process, the temperature forms a bulge rectangular shape. As time progresses, the shape get reduces gradually and at 2000 sec a tiny circle formed adjacent to the center of the domain.
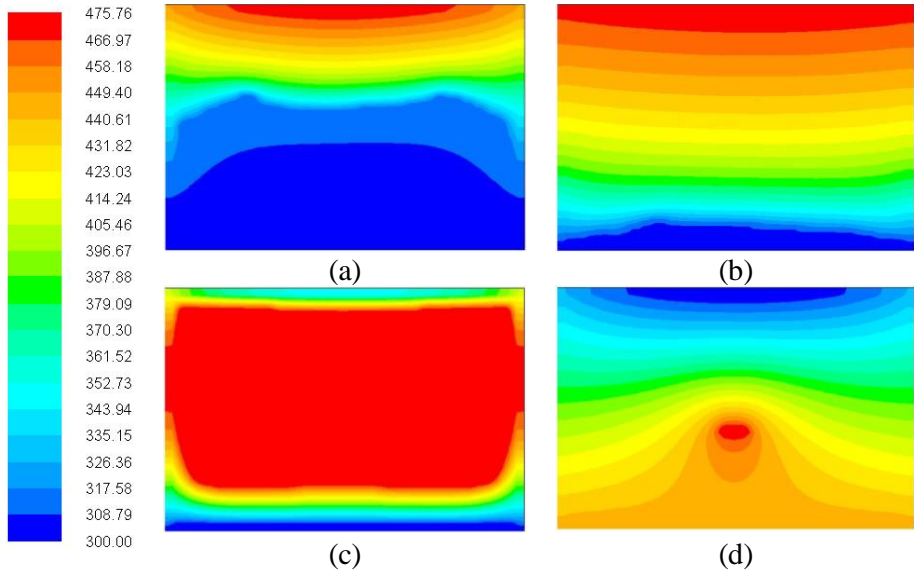
Figure 4.10: Variation of temperature during charging at (a) t = 500, (b) t = 2000 sec and discharging process at (c) t = 500, (d) t = 2000 sec in shallow domain.

4.3.6 Comparison of Mass Fraction in Deep and Shallow Domain

Figures 4.11 (a) and (b) shows the variation of mass fraction during charging and discharging processes in deep and shallow domains.
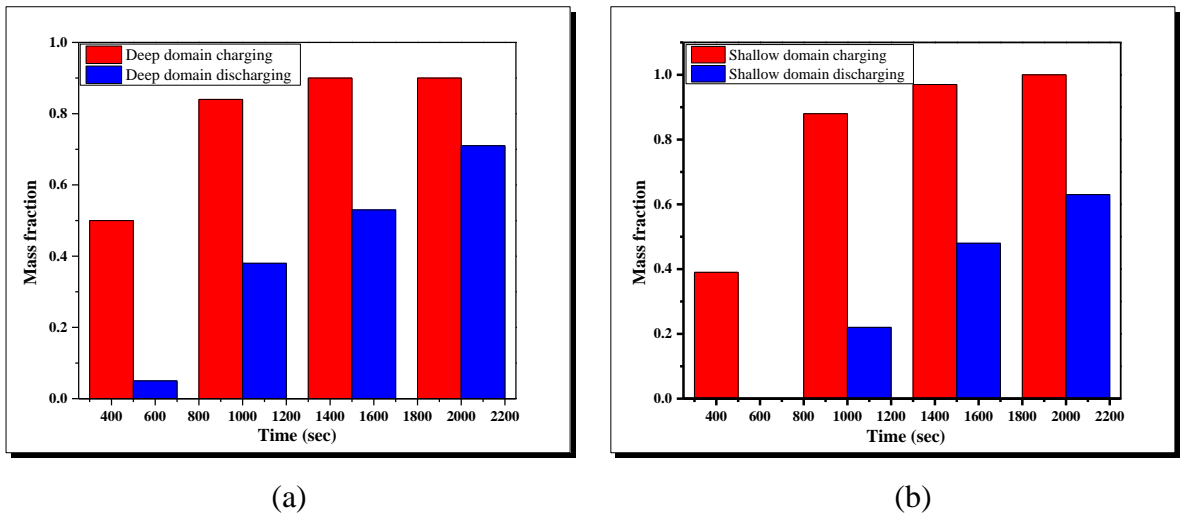
Figure 4.11: Variation of mass fraction during charging and discharging processes of (a) deep and (b) shallow domain.

The variation of mass fraction in the shallow domain is higher during charging and lesser during discharging as compared to deep domain. The shallow domain shown faster charging/discharging rate compared to the deep domain (up to 10% less time). The shallow domain can be preferred for better charging/ discharging rates, which could be essential in thermal storage applications.

4.4 EFFECT OF DIFFERENT ORIENTATIONS AND WALL HEATING OF MATERIALS

The study is continued for different orientations and wall heating to analyze the melting/solidification characteristics of CPCM. The numerical study is carried out for four different orientations by changing in clockwise direction. For each orientation, three different wall heatings are studied to understand the melting and solidification characteristics.

4.4.1 Problem Description

Figures 4.12 (a)-(d) shows the geometrical representation of the 2-D model with different orientations. The same geometry is studied by changing clockwise direction with the increment of 45°. (a) 45° orientation, (b) 90° (deep) orientation, (c) 135° orientation and (d)180° (shallow) orientation.
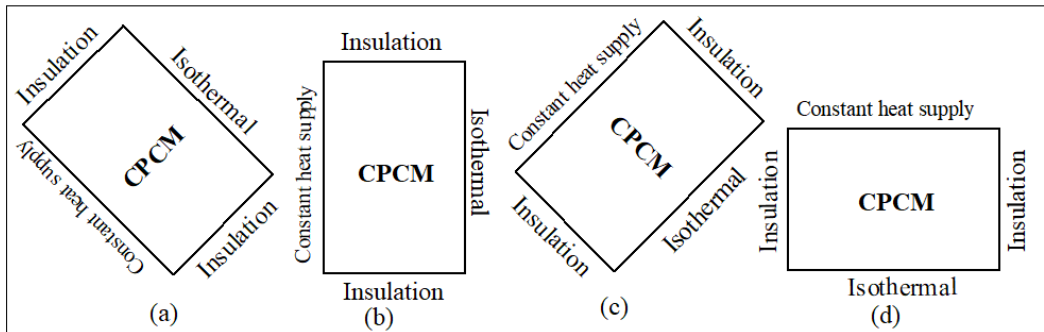
Figure 4.12: Geometrical representation of 2-D model with different orientations (a) 45° (b) 90° (deep) (c) 135° and (d)180° (shallow) orientation.

4.4.2 Boundary Conditions

The constant heat supplied to each wall, and the opposite wall is maintained isothermal at 300 K, and the remaining walls are insulated. For all the cases 250 W heat is supplied. The different conditions are (i) Constant heat supply applied to the base wall, (ii) Constant heat supply applied to the left wall, (iii) Constant heat supply applied to the top wall. All four orientations are investigated and observed the factors affecting the melting and solidification characteristics. Orientation effects are studied for flow characteristics, melting of CPCM, and temperature distribution.

4.4.3 Flow Characteristic Study for Shallow Domain with Heating and Cooling

The complete melting and solidification processes are divided into different time steps (500, 1000, 2000 and 3000 sec) for melting and (100, 500, 800 and 1200 sec) for solidification process to understand the mechanism. The maximum time limit of 3000 sec is selected due to shallow domain completes melting at 3000 sec. Solidification process completes within 1200 sec time duration.

Variation of streamline patterns for base wall heating and cooling is shown in figures 4.13 (a) and (b) respectively. Heat transfer through base wall forms circulation vortices adjacent to the hot wall, which is due to the development of the melting front. The progression of the buoyancy effect causes the development of circular currents adjacent to the hot wall of the domain. A sunken shape at the upper portion of the melt front is observed while the interface is linear. For 3000 sec, it covers half of the domain, and there is no change in the streamline patterns due to non-penetration of melting layer. Heat rejection reduces the vortex formation during solidification process as time progresses, these patterns disappear and generate a uniform distribution of streamline patterns at 1200 sec.

Variation of streamline patterns for left wall heating and cooling are shown in figures 4.13 (c) and (d). In the melting process streamline patterns forms a thin layer of molten CPCM near the hot wall, which demonstrates the conduction heat transfer, and it succeeds until the fluid is resisted by the viscous effect. At this stage, the solid-liquid interface becomes steady and remains uniform along the surface of the hot wall. As time progresses, melting layer thickness builds and buoyancy effect increases which dominates the viscous effect.

The top portion of the solid-liquid interface initiates the natural convection currents in the melting region and starts dissolving due to erosion.

(i) 500 sec

(ii) 1000 sec

(iii) 2000 sec

(iv) 3000 sec

(a) Base wall heating

(i) 100 sec

(ii) 500 sec

(iii) 800 sec

(iv) 1200 sec

(b) Base wall cooling

(i) 500 sec

(ii) 1000 sec

(iii) 2000 sec

(iv) 3000 sec

(c) Left wall heating

(i) 100 sec

(ii) 500 sec

(iii) 800 sec

(iv) 1200 sec

(d) Left wall cooling

(e) Top wall heating

(i) 500 sec

(ii) 1000 sec

(iii) 2000 sec

(iv) 3000 sec

(f) Top wall cooling

(i) 100 sec

(ii) 500 sec

(iii) 800 sec

(iv) 1200 sec
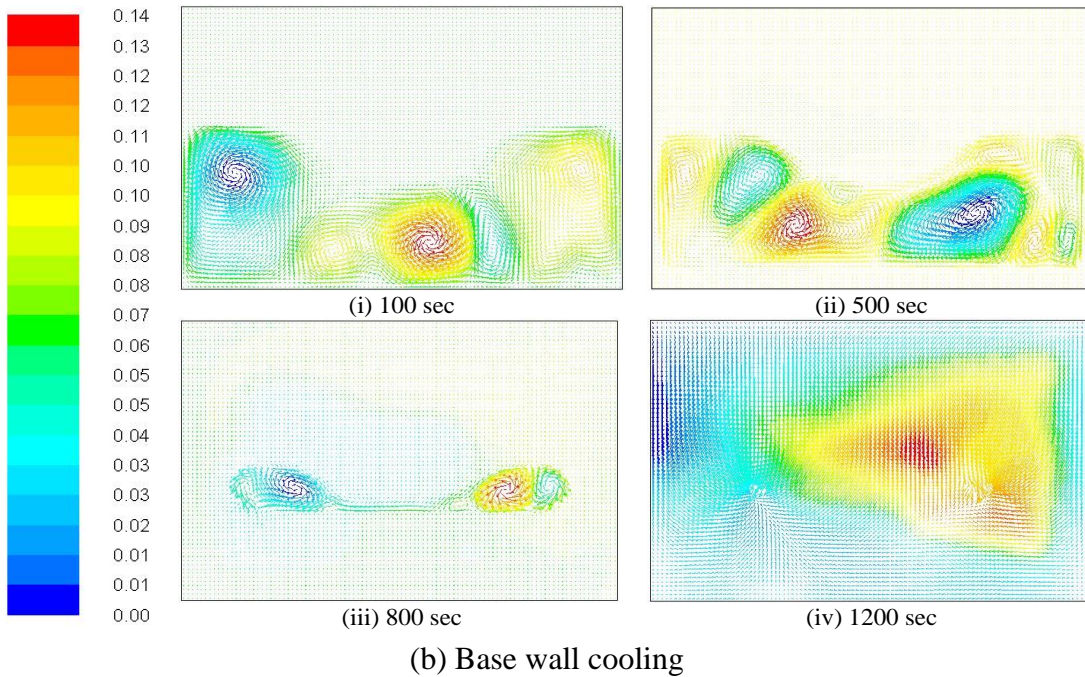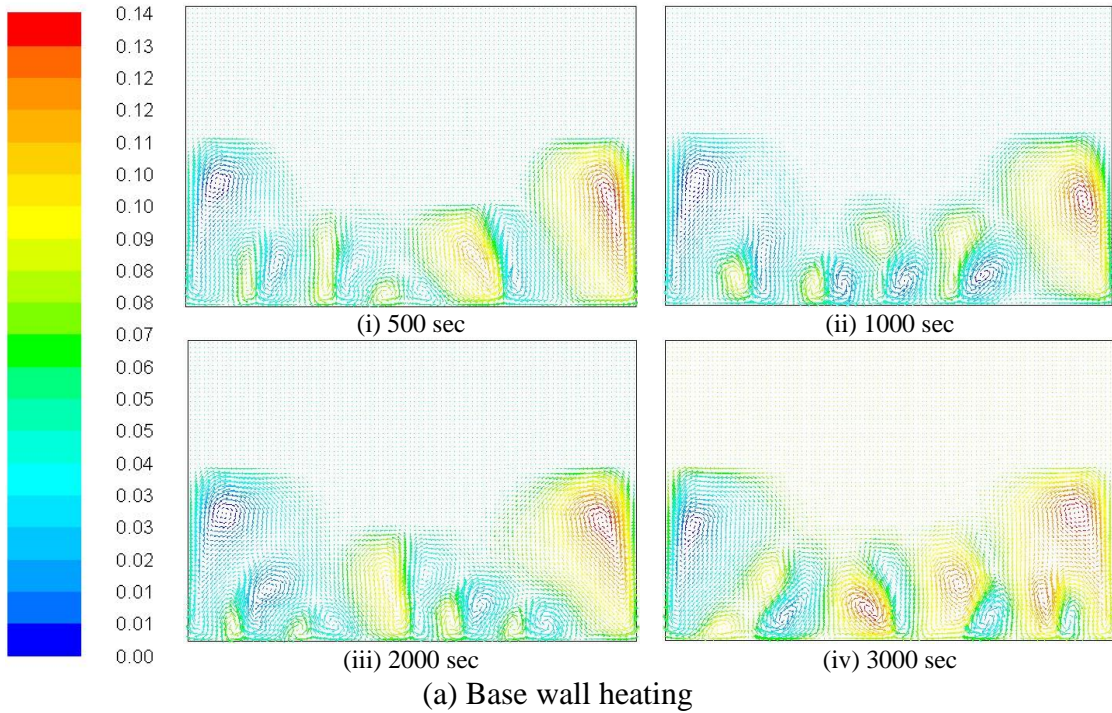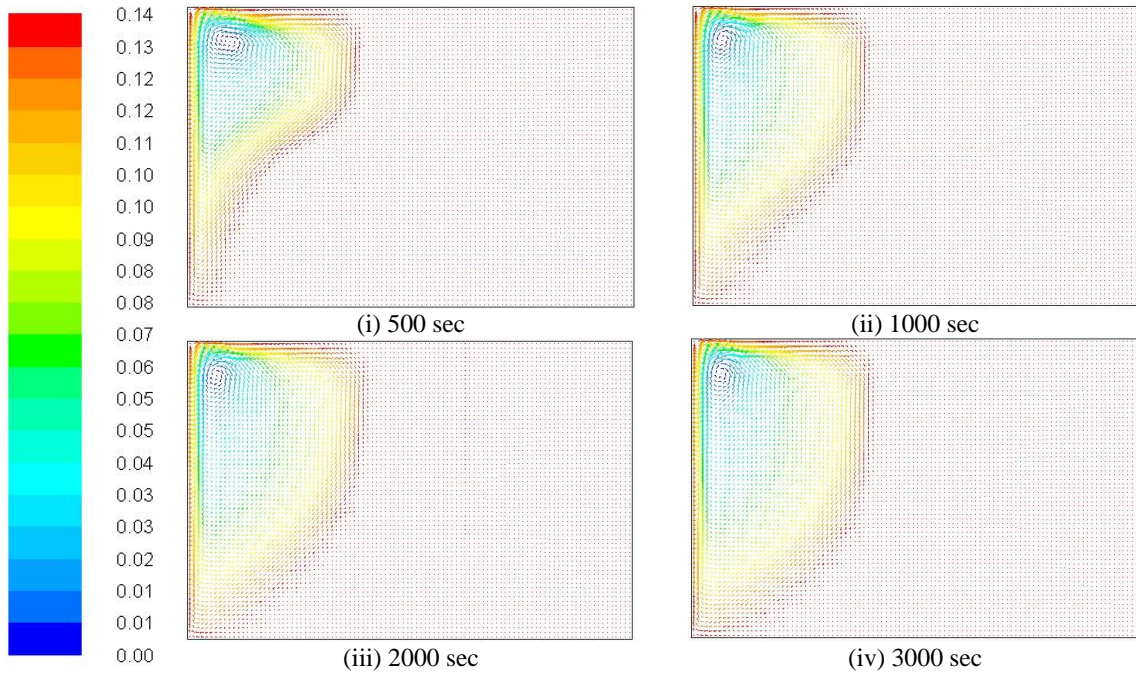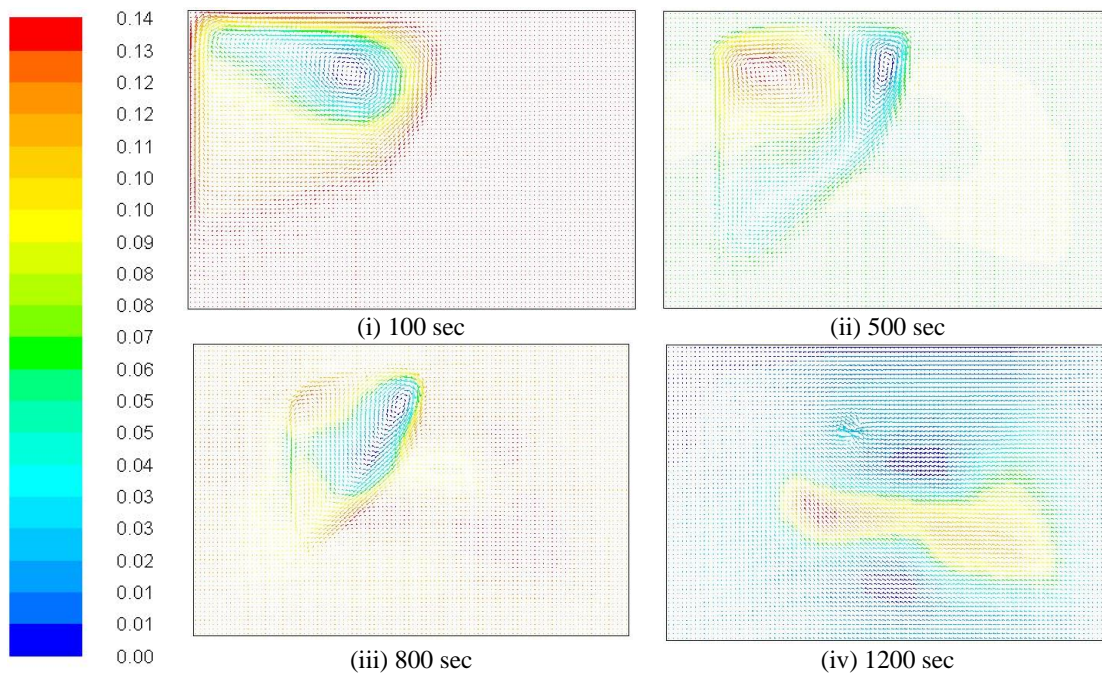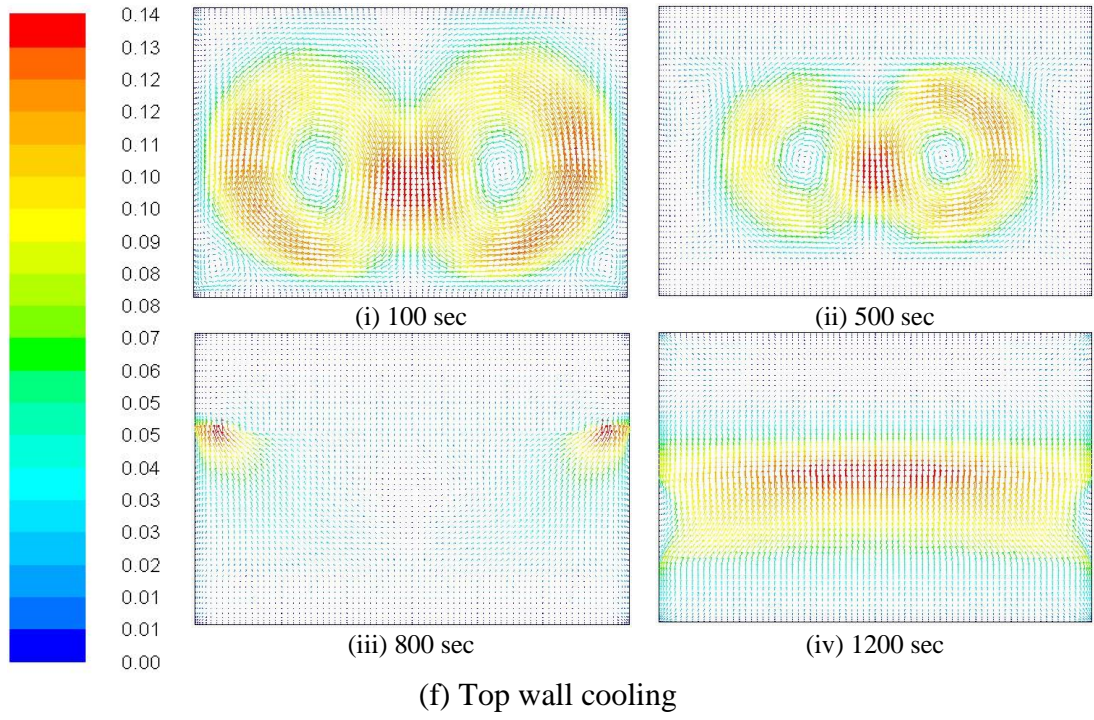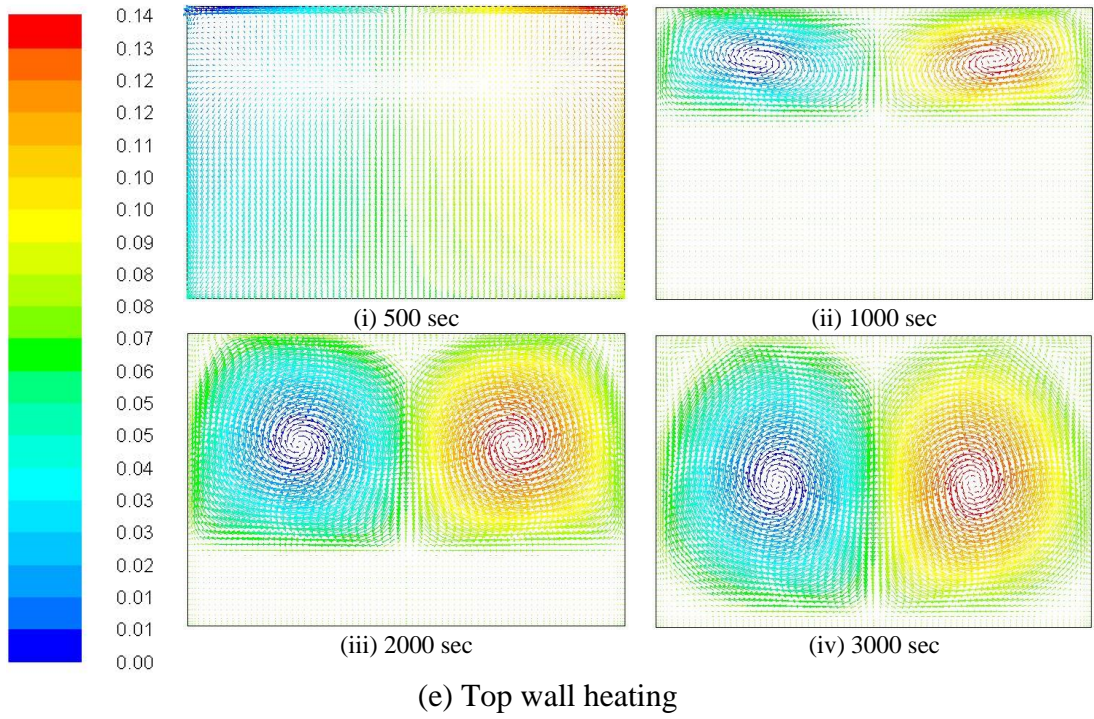
Figure 4.13: Variation of streamline patterns (a) base wall, (c) left wall, (e) top wall heating, and (b) base wall, (d) left wall, (f) top wall cooling process.

The increase in buoyancy effect develops the circulation currents and the bottom portion of melting front changes and raises with time. Variations of streamline patterns for top wall heating and cooling are shown in figures 4.13 (e) and (f). In the melting process streamline patterns changes abruptly, and as temperature increases, the convection currents travel and occupies the significant portion of the domain. The smooth movement of fluid develops continuously until 3000 sec. The natural convection currents in the domain are fully generated, and the complete process can be visualized from figures 4.13 (a)-(f).

4.4.4 Variation of Mass Fraction in Shallow Domain for Heating and Cooling

Figures 4.14 (a)-(f) shows the variation of melting fraction during heating and cooling processes in the shallow domain. At the beginning of the melting process, the solid-liquid interface dominated by conduction heat transfer. The interface patterns change to the wavy structure and is controlled by the natural convection streams in the liquid CPCM. The hot liquid travel towards the center of domain in the opposite direction to the hot wall due to erosion, the solid falls to the bottom of domain as shown in figures 4.14 (a) and (b). As the fluid layer builds towards the center and it vanishes, but the liquid fraction at the base wall increases. Approximately half portion gets melted due to lack of contact between molten and solid phase. Thin molten layers cannot penetrate at higher level because conduction gets depressed and the convection heat transfer dominates. The heat transfer coefficient becomes small and convection becomes insignificant.

The effect of gravity on molten phase causes settlement on the base wall and buoyancy effect is not enough to reach the remaining portion of domain. The orientation also affects the melting and solidification processes. The molten fluid is fallen and spread all over the solid phase and it comes directly in contact. Heat transfer begins and covers a larger surface area of solid CPCM and melts relatively faster. The uniform melting can be achieved and complete melting without partially molten patches. The solidification process is dominated by conduction, and the orientation affects the melting process due to the variation of natural convection currents and gravitation effect. The inclusion of nano additives, such as copper or copper oxide nanoparticles, might significantly depress the natural convection heat

transfer rate and reduces the melting process when orientation is changed and the same trend is observed.

Melting fraction variation during left wall heating and cooling are shown in figures 4.14 (c) and (d). In the left wall heating, the interface movement is uniform and melting profile at the upper region is smoothly curved at the beginning, and it expands slightly. The high melting rate at the upper part of domain where the fluid CPCM ascended along the heated wall. The melting rate is low at the bottom of domain where the fluid is cold. In this heating it requires long duration to complete the melting process up to 3000 sec small portions of CPCM is melted but cooling occurs at much faster rates. The domination of the conduction falls on molten fluid and spread all over the solid CPCM. The molten fluid comes directly in contact with solid, heat transfer begins, and CPCM melts quickly.

(i) 500 sec

(ii) 1000 sec

(iii) 2000 sec

(iv) 3000 sec

(a) Base wall heating

(i) 100 sec   (ii) 500 sec

(iii) 800 sec   (iv) 1200 sec

(b) Base wall cooling

(i) 500 sec   (ii) 1000 sec

(iii) 2000 sec   (iv) 3000 sec

(c) Left wall heating

(i) 100 sec   (ii) 500 sec

(iii) 800 sec   (iv) 1200 sec

(d) Left wall cooling

(i) 500 sec   (ii) 1000 sec

(iii) 2000 sec   (iv) 3000 sec
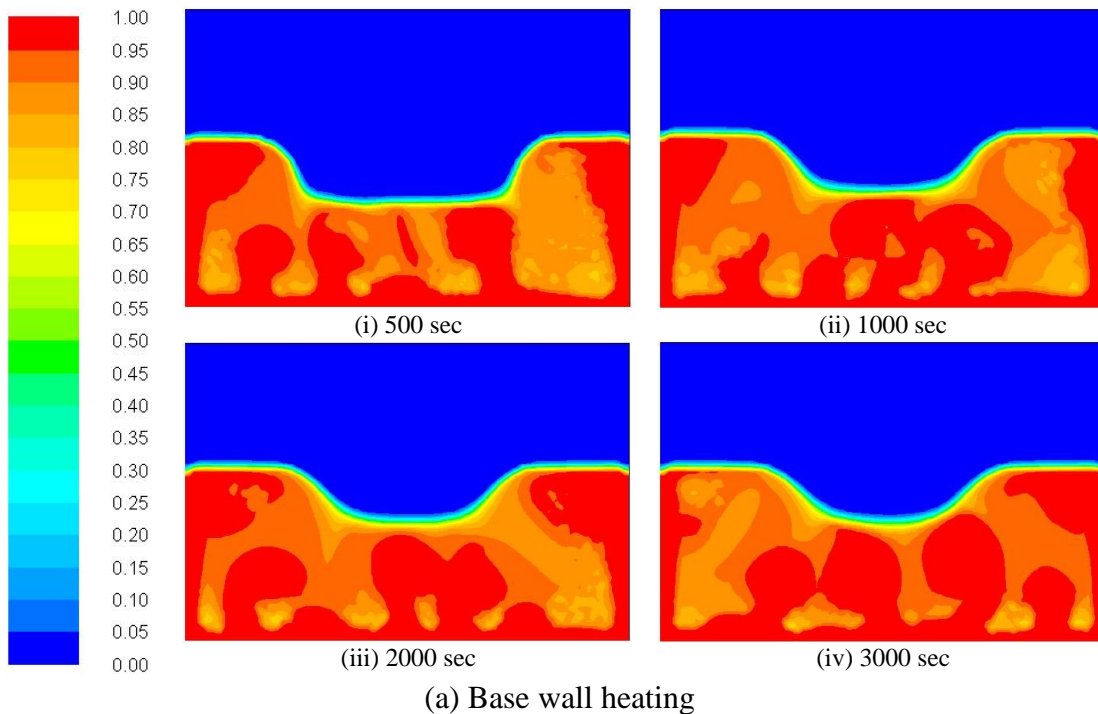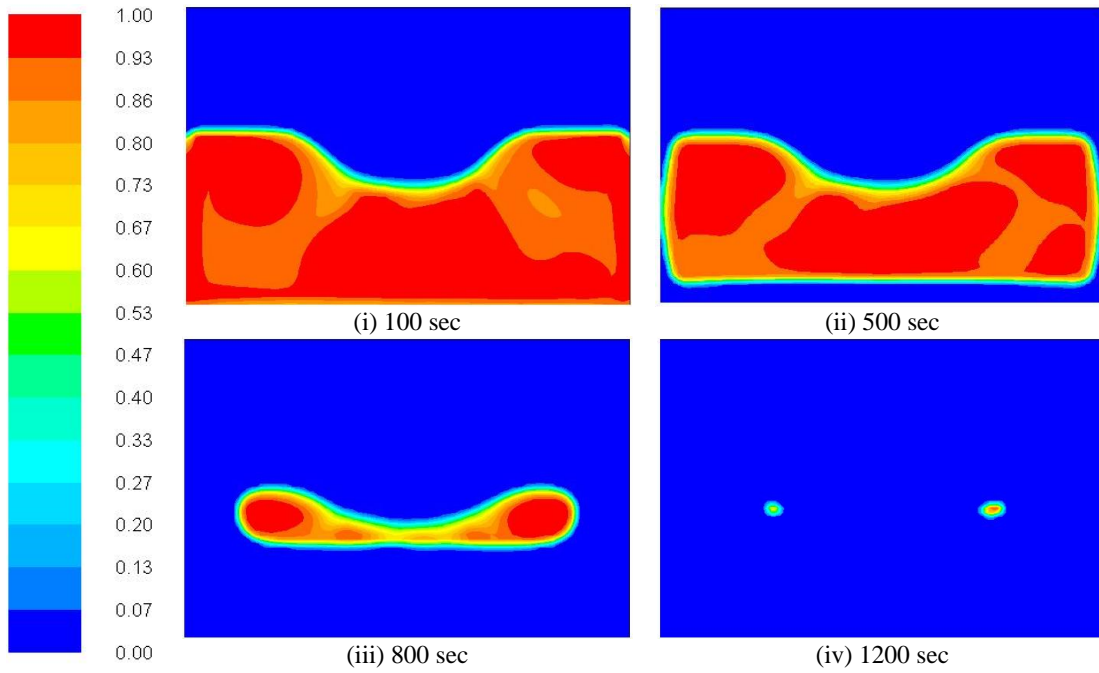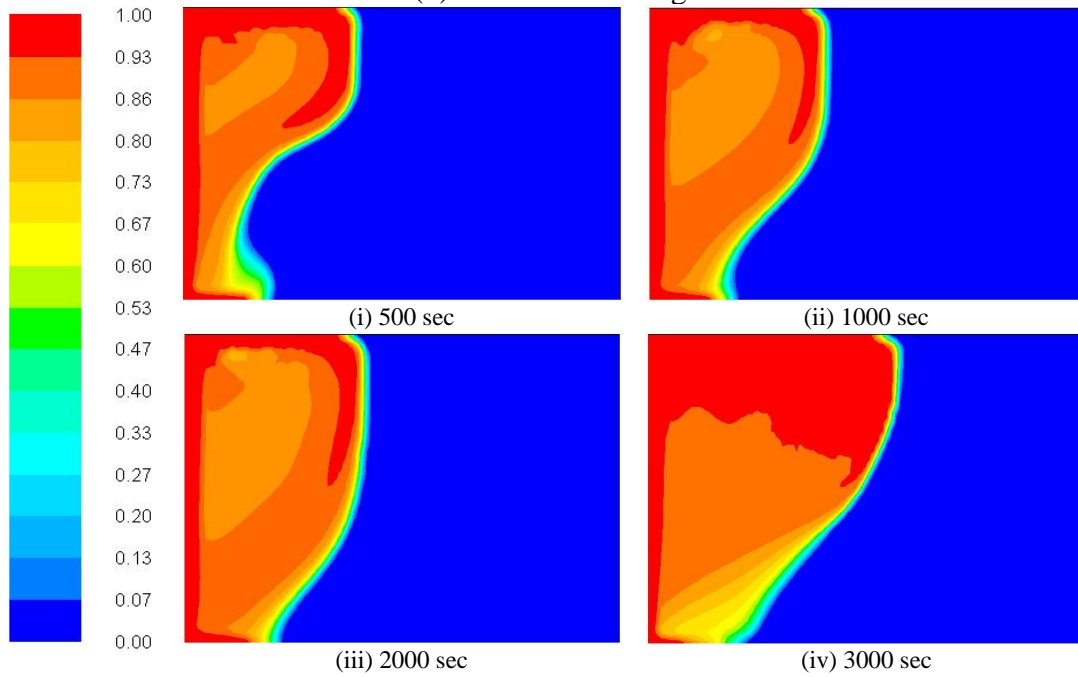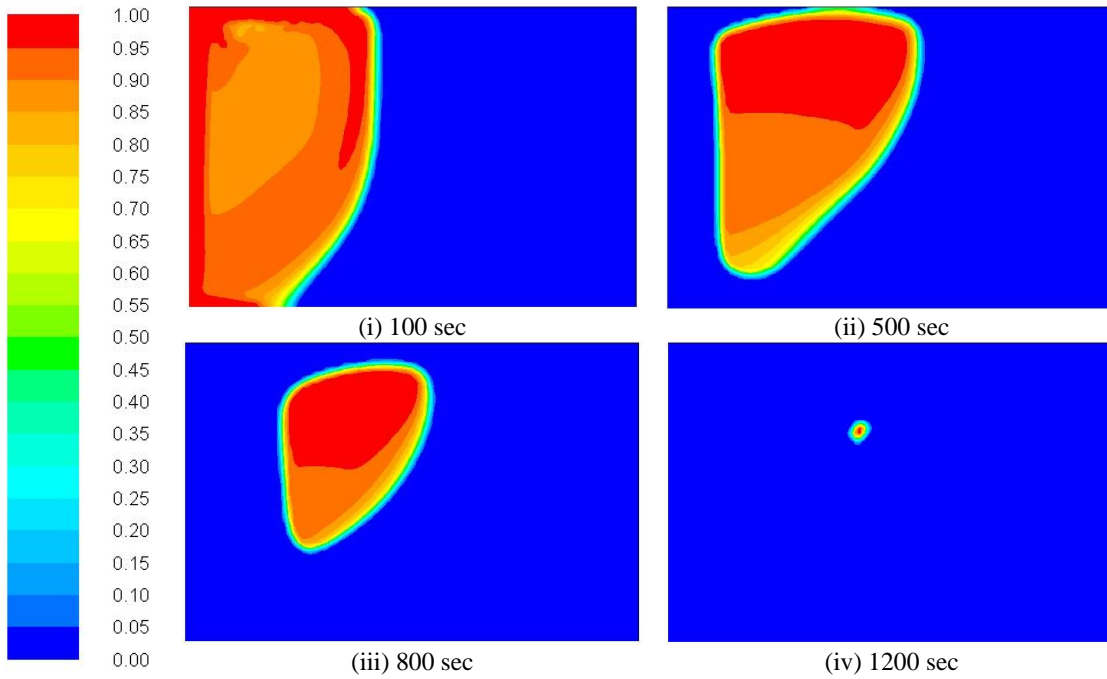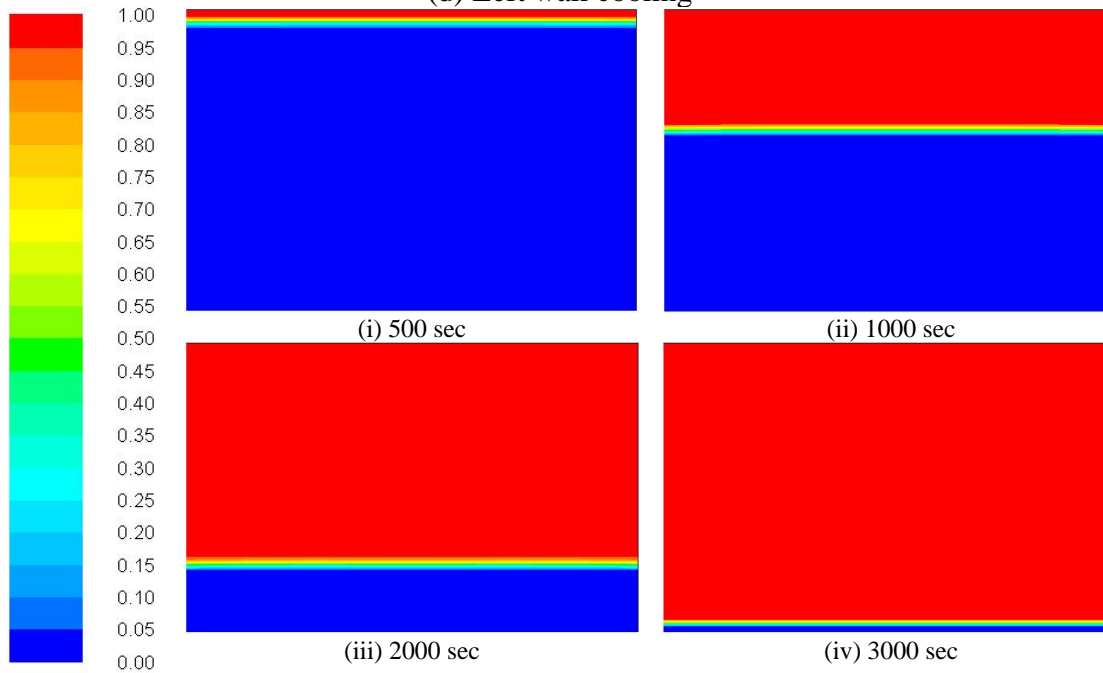
(e) Top wall heating
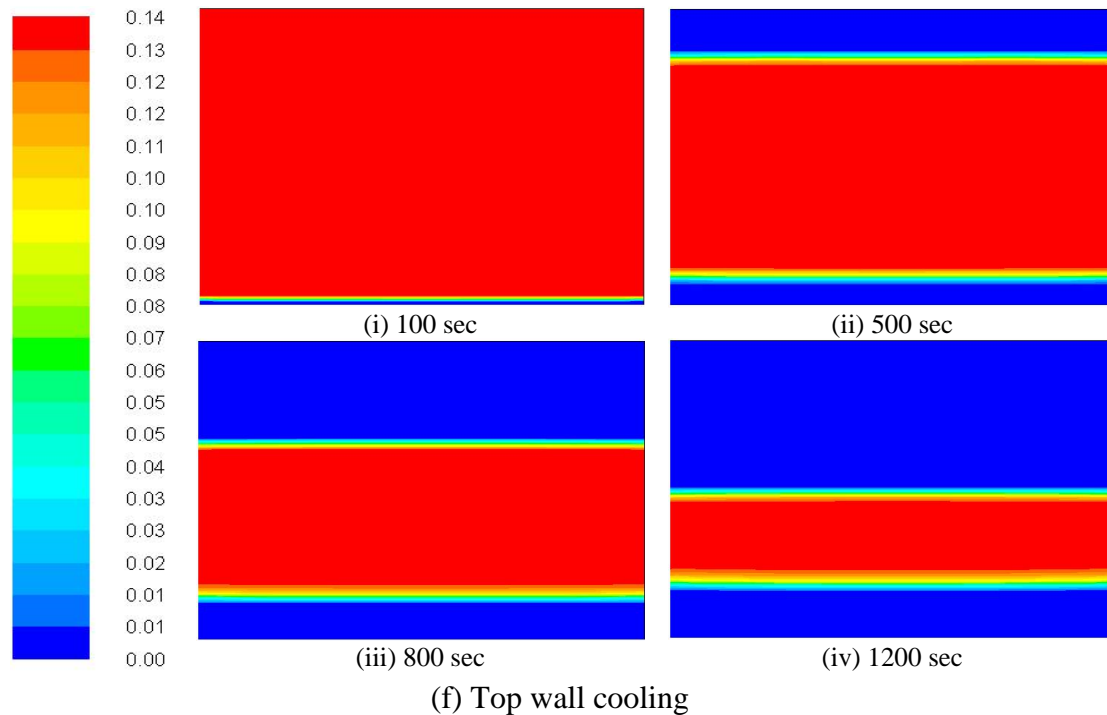
(f) Top wall cooling

Figure 4.14: Variation of melting fraction (a) base wall, (c) left wall and (e) top wall heating and (b) base wall, (d) left wall (f) top wall cooling process.

Melting fraction variation during top wall heating and cooling are shown in figures 4.14 (e) and (f). The heat transfer coefficient becomes very low and convection becomes insignificant. The effect of gravity on molten phase causes settlement on the base wall and buoyancy effect is not enough to reach the remaining portion of domain. The solid-liquid interface becomes steady and uniform along the surface of the hot wall. As time progresses, the melt layer thickness builds, and the increase in buoyancy effect dominates the viscous effect. The top portion of the solid-liquid interface initiates the natural convection currents in the melting region and starts to dissolve due to erosion. The solidification occurs fast due to reconnection and accumulation of eroded dissolved particles. Solid-phase formation is quicker at the upper portion of the domain and rejects heat from the mushy zone. As the solid CPCM shrinks and its pinnacle point moves down along the left wall, the temperature of molten CPCM at the top portion of domain expands which affirms the contiguity of the ineffective velocity field.

4.4.5 Variation of Temperature in Shallow Domain for Heating and Cooling

Figure 4.15 shows the variation of temperature for heating and cooling processes. Initially, temperature patterns are almost parallel to the heating wall and heat transfer is predominant. At a later stage, the temperature of the liquid CPCM near the heating wall increases and molten CPCM travels along vertical sides due to succession of buoyancy effect over the viscous force. Temperature distribution for base wall heating and cooling processes are shown in figures 4.15 (a) and (b). The liquid CPCM travels until it reaches the upper portion of domain and diverts towards the solid region. The impingement of molten CPCM enhances the local heat transfer coefficient and the melting rate is increased. The melting rate at the bottom portion of domain is low compared to the upper portion. This indicates the temperature reduction of molten CPCM as it drops along with the interface and results in low heat transfer to the solid CPCM.

As time progresses, the solid CPCM shrinks and its pinnacle point moves down along the left wall. The temperature of molten CPCM at the upper portion of domain expands which affirms the contiguity of the ineffective velocity field. The growth of molten CPCM at the upper part of domain shows heat absorption by molten CPCM from the heated wall. It indicates the upper part of domain without the solid CPCM. Temperature distribution replicates the isothermal wall because the heat has not reached till that point and it remains in the sub-cooled form with uniform temperature distribution. Figures 4.15 (c) and (d) shows temperature distribution for left wall heating and cooling processes. During the solidification process, the temperature distribution changes completely at initial phases, it surrounds the molten CPCM in which heat is distributed gradually. The size of the region get reduces, and it disappears completely at the end.

The left wall heating provides uniform temperature distribution all over the surface of the domain. The temperature contours are linear with the heating wall, and it carries to base wall. Temperature distribution for top wall heating and cooling processes as shown in figures 4.15 (e) and (f). Except for the sub-cooled region, the contours are uniform and impingement of molten CPCM to the solid-liquid interface quickens the melting rate. The melting rate at the lower portion of the domain is less than that of the upper portion. The

temperature of molten CPCM reduces as it falls along with the interface, and results in low heat transfer to the solid CPCM at the lower portion of the domain. A consistent change in the melting layer thickness and average variation in patterns of the solid-liquid interface shows the development of a prodigious flowing current in the liquid.

(i) 500 sec   (ii) 1000 sec

(iii) 2000 sec   (iv) 3000 sec

(a) Base wall heating

(i) 100 sec   (ii) 500 sec

(iii) 800 sec   (iv) 1200 sec

(b) Base wall cooling

(i) 500 sec   (ii) 1000 sec

(iii) 2000 sec   (iv) 3000 sec

(c) Left wall heating

(i) 100 sec

(ii) 500 sec

(iii) 800 sec

(iv) 1200 sec

(d) Left wall cooling

(i) 500 sec

(ii) 1000 sec

(iii) 2000 sec

(iv) 3000 sec
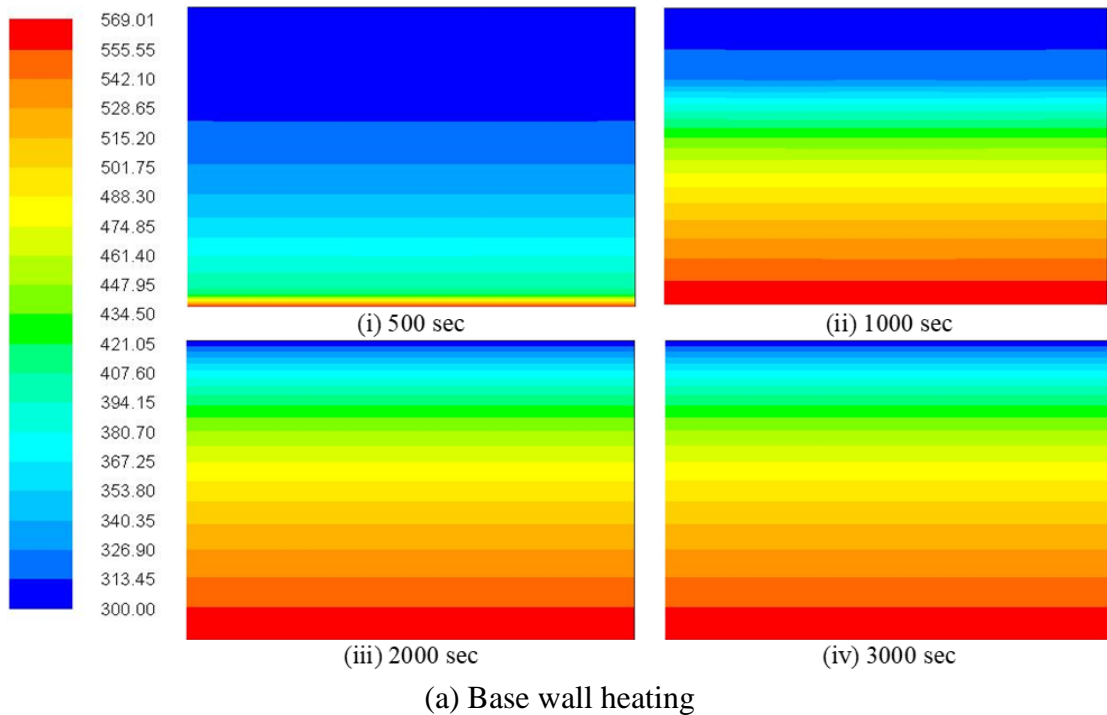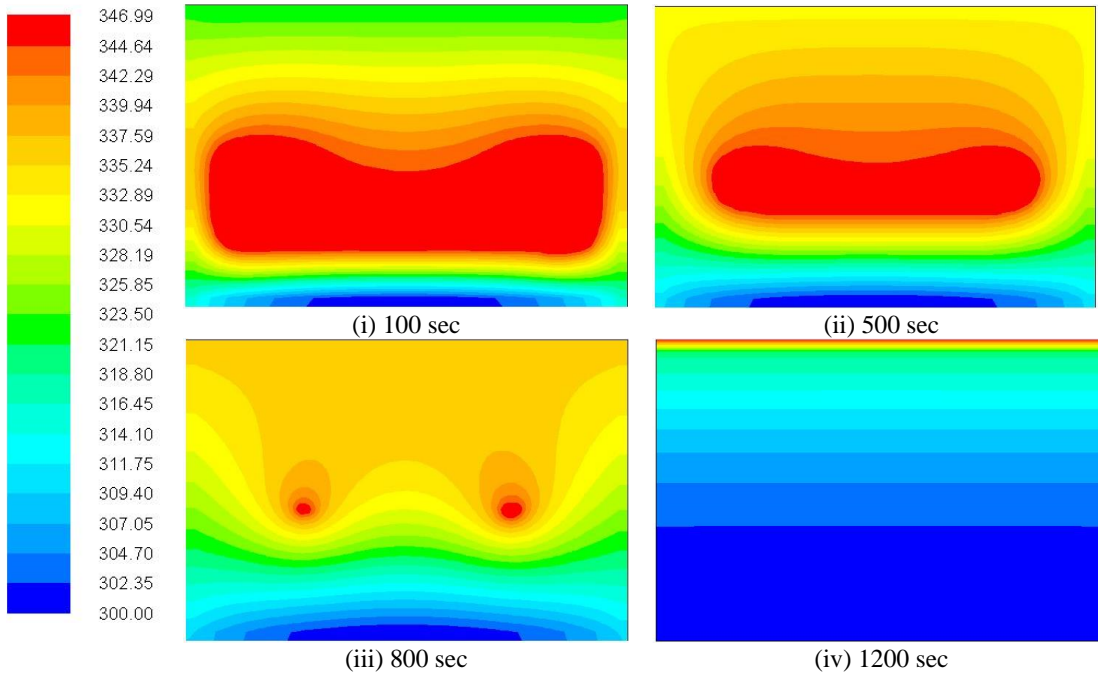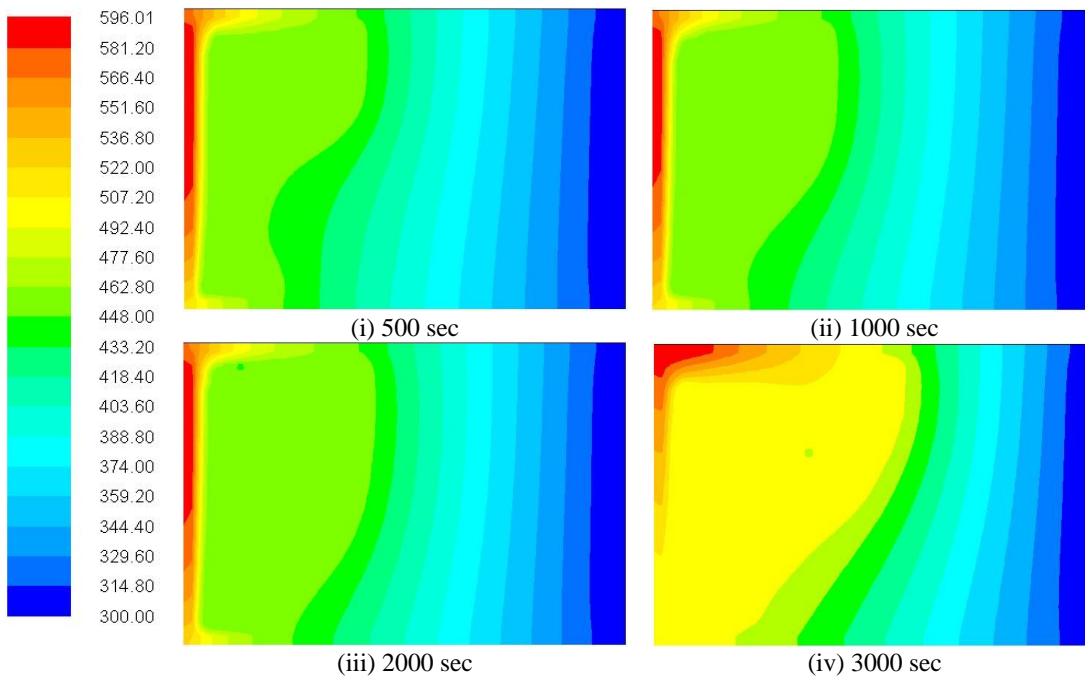
(e) Top wall heating
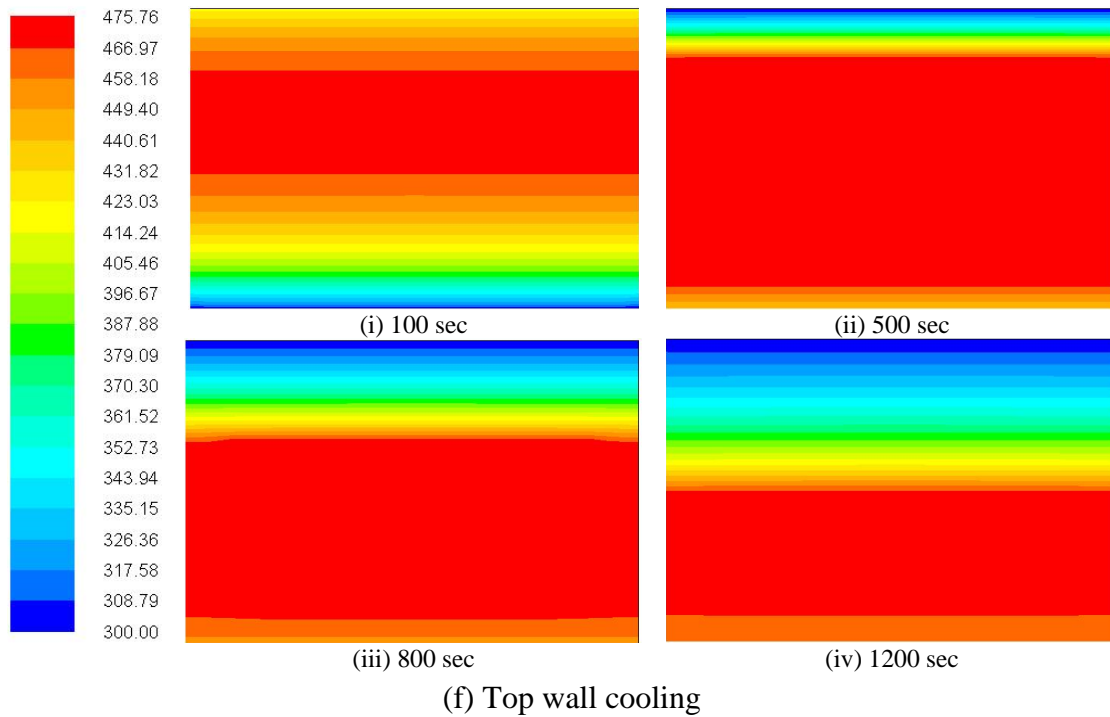
(f) Top wall cooling

Figure 4.15: Variation of temperature (a) base wall, (c) left wall, (e) top wall heating and, (b) base wall, (d) left wall and (f) top wall cooling processes.

The heating from the top surface is an efficient way to achieve faster melting and solidification. During solidification, the solid phase formation is quicker due to the availability of a high area of exposure. Heat transfer through base wall makes streamline patterns to form circular vortices adjacent to the hot wall, which is purely due to the development of melting front and movement of fluid flow velocities. The progression of buoyancy effect causes the growth of circular currents at adjacent to the hot wall, makes sunken shape at the upper portion of the melt front while in the upper portion of the interface is linear. For enough time duration, it covers half of the domain, and there is no change in the streamline patterns due to non-penetration of melting layer. Heat rejection process reduces the vortex formation during the melting process, as time progresses, patterns disappear, and uniform velocity distribution generated.

70

4.4.6 Flow Characteristic Study in Deep Domain for Left Wall Heating and Cooling

(a) Left wall heating
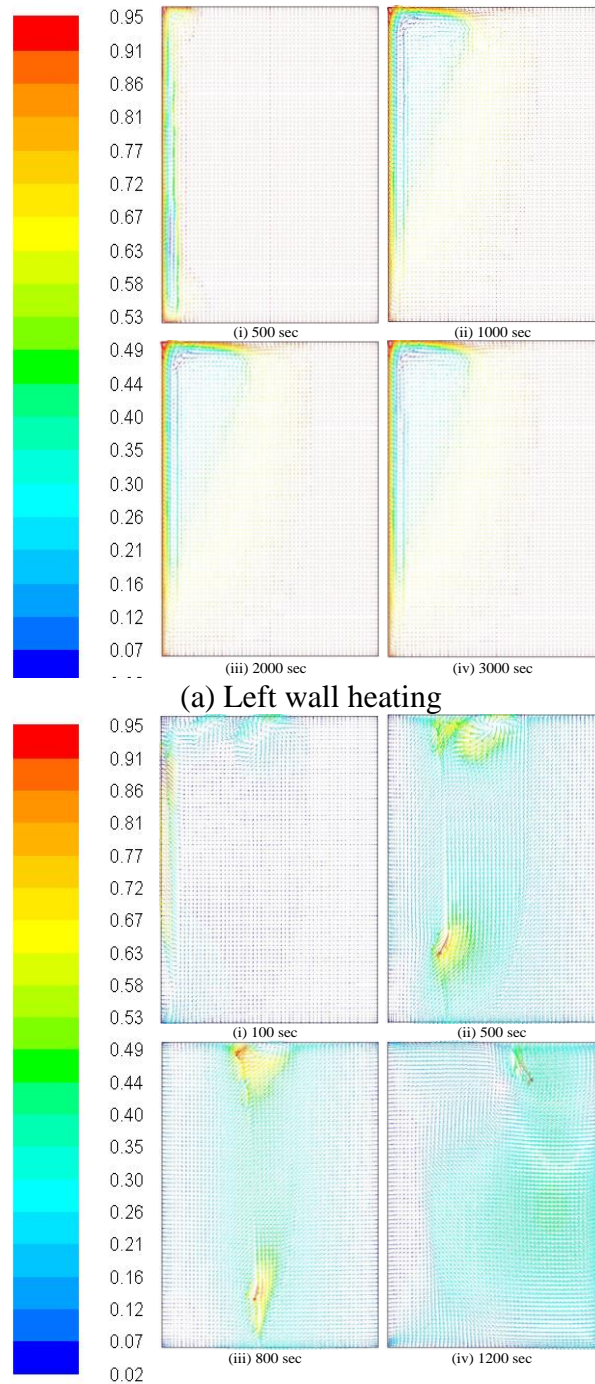
(b) Left wall cooling

Figure 4.16: Variation of streamline patterns for left wall (a) heating and (b) cooling in the deep domain.

Figures 4.16 (a) and (b) shows the variation of streamline patterns for left wall heating and cooling. In the melting process, the flow patterns move towards the entire bounded domain, which results in quick heat transfer rate. During the initial phase of the melting process melting rate is high, due to the high temperature difference between the molten and solid CPCM. As time progresses, the heat transfer rate drops, and heat reduces and the melting process breaks with uniform streamline patterns. Initially, in the solidification process, the molten CPCM circulates inside domain completely by occupying the whole domain. Flow patterns break and spread the whole domain, which indicates the complete solidification of the CPCM and completion of the solidification process.

4.4.7 Variation of Mass Fraction in Deep Domain for Left Wall Heating and Cooling

Figures 4.17 (a) and (b) shows the variation of meting fraction for left wall heating and cooling in the deep domain. In the initial stages of the melting process, the liquid interface imitates the hot wall due to the domination of conduction heat transfer in the melting zone. The viscous effect opposes the fluid motion and succeeds the conduction with a uniform melting. As the process continues, the liquid fraction increases and spreads all over the domain. As molten fluid starts flowing downwards along the interface, heat transfer takes place from hot molten fluid to solid CPCM. The heat interaction between the thin molten layer to the thick solid CPCM is quicker due to overlapping of complete solid surface. The dominant circulating currents are formed due to the consistent variation of melting layer thickness and changing phase from solid to liquid. As time succeeds, similar patterns retain until CPCM completely gets melted. In the cooling process, solidification begins from the hot and cold wall by concentrating the molten phase in the center, the continuous growth of solid-phase makes shrink and gets dissolves by completing the cooling process.
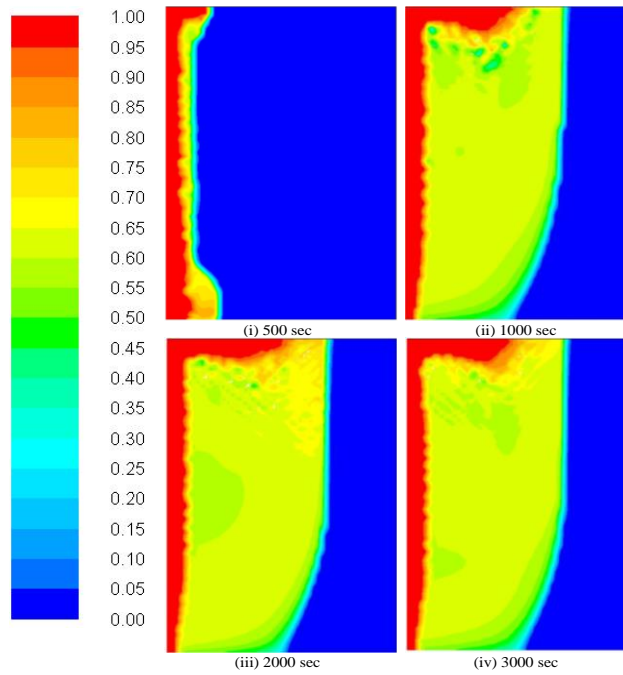
(a) Left wall heating
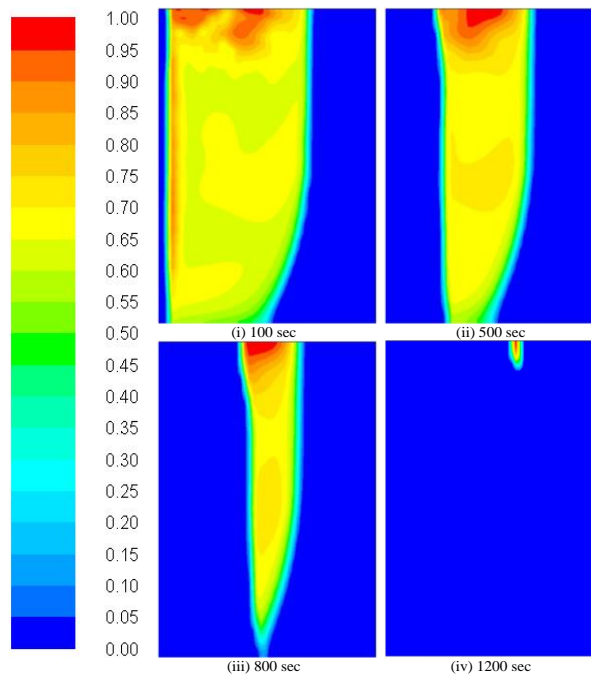
(b) Left wall cooling

Figure 4.17: Variation of meting fraction for left wall (a) heating and (b) cooling in deep domain.

4.4.8 Variation of Temperature in Deep Domain for Left Wall Heating and Cooling

Figures 4.18 (a) and (b) shows the variation of temperature for left wall heating and cooling in the deep domain. The temperature is non-uniformly distributed all over the surface of domain other than the sub-cooled region. At the upper portion, the temperature is naturally high and travels with a gradual decrease through the vertical walls. The other two heating cases, top wall heating gave a uniform temperature distribution for complete melting and solidification processes. These patterns indicate the proper melting and traveling of uniform melting front.
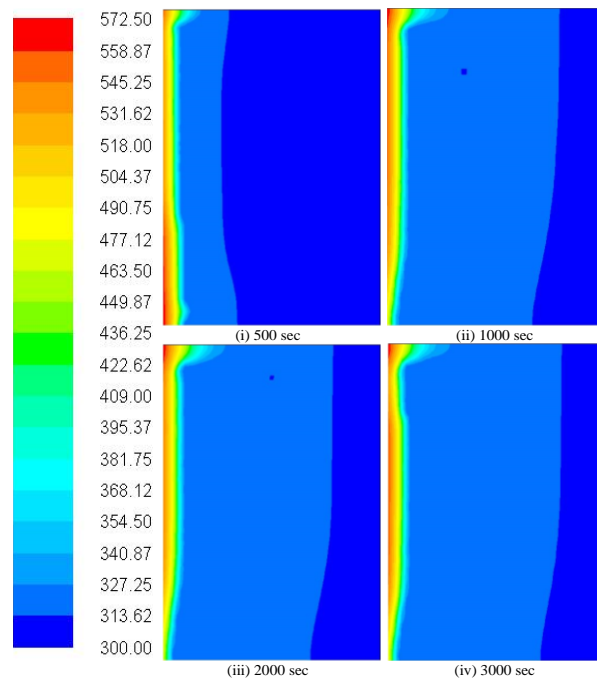
(a) Left wall heating
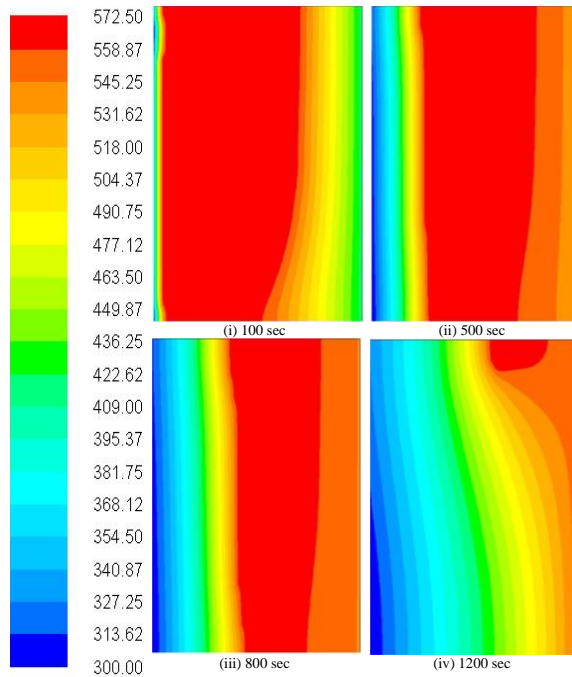
(b) Left wall cooling

Figure 4.18: Variation of temperature for left wall (a) heating and (b) cooling in the deep domain.

4.4.9 Flow Characteristic Study for 45° Orientation with Left Wall Heating and Cooling

Figure 4.19 (a) and (b) shows the variation of streamline patterns for 45° orientation with left wall heating and cooling. Flow characteristics for all the three wall heating cases are studied, it shows uniform distribution of streamline patterns. The heat transfer mechanism adjacent to the hot wall by conduction and the CPCM starts to absorb the heat and initiates the melting process. After saturation limit, begins to change its physical state and forms a liquid layer over the solid surface. The molten layer gets separated from the hot wall, and convection plays a vital role.
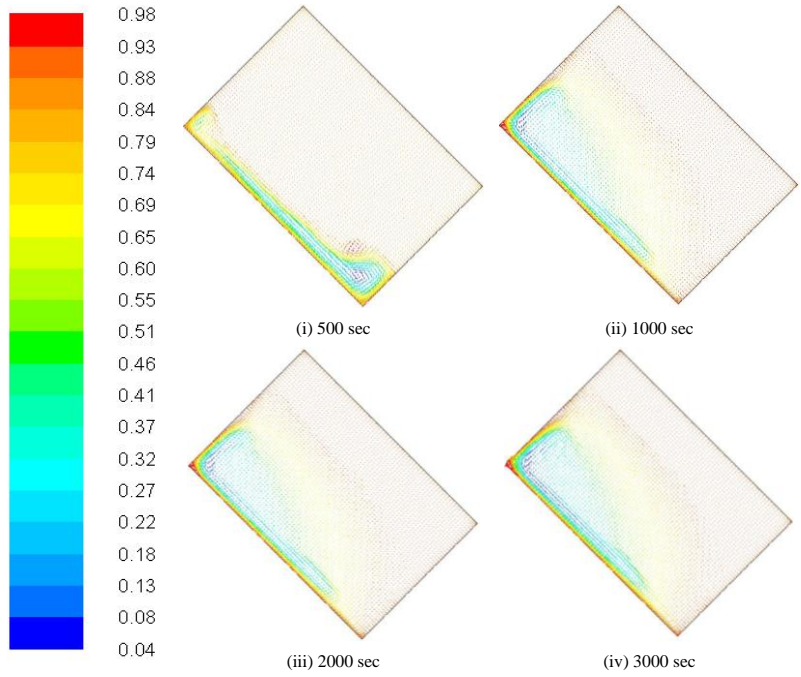
(a) Left wall heating
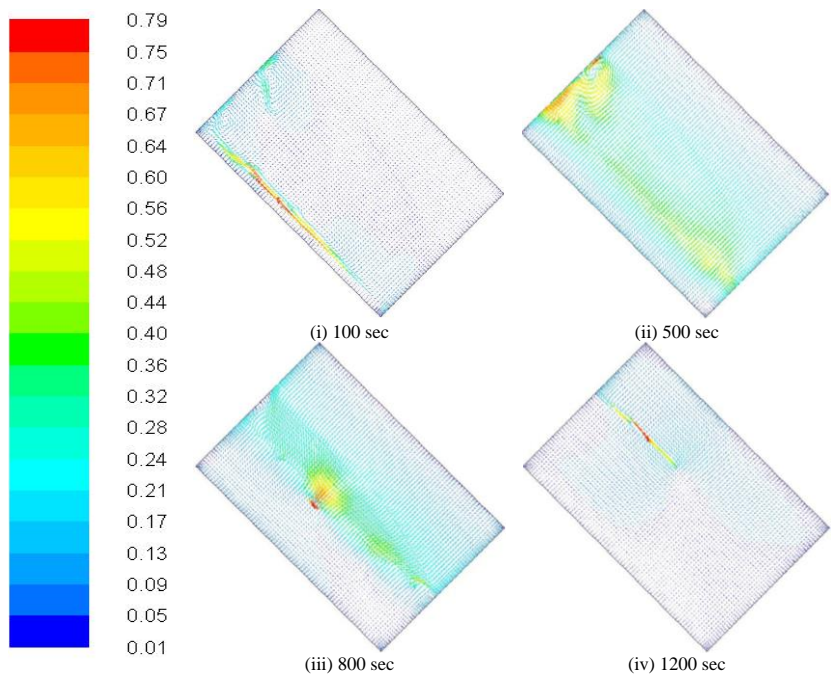
(b) Left wall cooling

Figure 4.19: Variation of streamline patterns for left wall (a) heating and (b) cooling in 45°orientation.

Heat transfer takes place through the convection mode in molten liquid, and CPCM flows in the downward direction because of gravity and melting process. It gets accelerated, movement of flow can be visualized from figure 4.19. A consistent change in the melting layer thickness and variation in patterns of the solid-liquid interface shows the development of flowing current in the liquid CPCM.

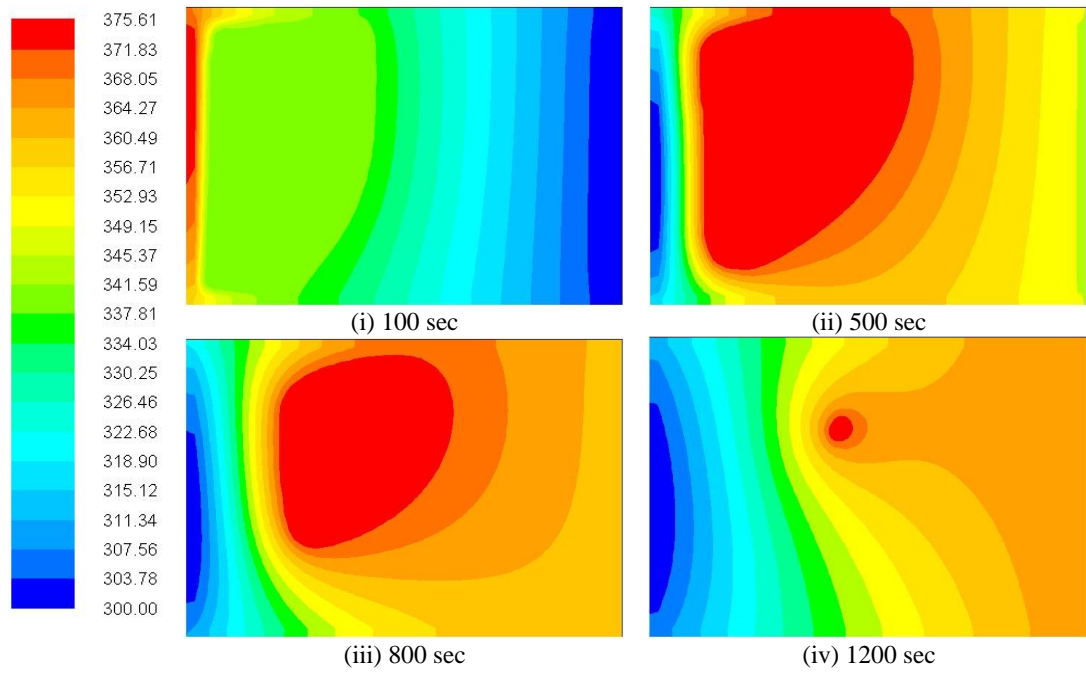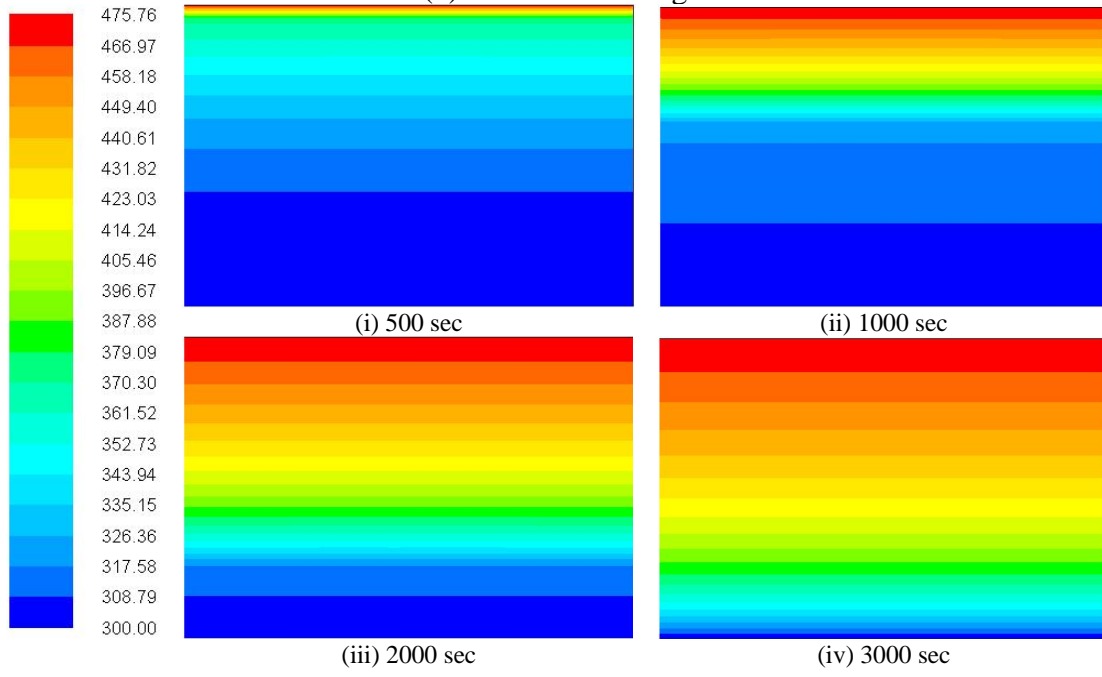The melting front shows articulate bulge along the hot wall due to impact of the convection in the mushy zone. The streamline patterns are too far from the cold wall, it increases the heat loss, increases the bulge size in the cooling region. The returning streamline patterns from the hot wall impedes the development of the mushy zone at the upper portion of domain making bulge more intense at the center. At the initial stages, the flow field is slightly close to the hot wall because of the no-slip condition of walls. Thus, remarkable solidification occurs around there, at a later stage, more significant moment of the liquid creates higher flow fields near the hot wall and solidification proceeds. The solidification behavior is observed for the transient transformation of the flow field. Finally, the circular vortex shrinks and disappears completely as the freezing process completes.

4.4.10 Variation of Melting Fraction for Domain of 45° Orientation with Left Wall Heating and Cooling

Figures 4.20 (a) and (b) shows the variation of melting fraction for left wall heating and cooling in 45° orientation. The energy transportation over the fluid layer is only by conduction mode. In the melting region, natural convection also influences, and it plays a crucial role in heat transfer processes and convection predominates in the melting phase. Visualization of patterns confirms the melting process and no variation in solid-liquid interface patterns. This demonstrates the natural convection of liquid CPCM and retains two-dimensional amid the entire melting process. At this stage, the viscous effect and gravity together overcome the buoyancy effect and causes no further movement of the melting front. In the cooling process as heat rejection starts molten CPCM initiates shrinking and all particles encounter each other. This physical contact results domination of conduction heat transfer and forms bulged shape.

(i) 500 sec   (ii) 1000 sec

(iii) 2000 sec   (iv) 3000 sec

(a) Left wall heating

(i) 100 sec   (ii) 500 sec

(iii) 800 sec   (iv) 1200 sec
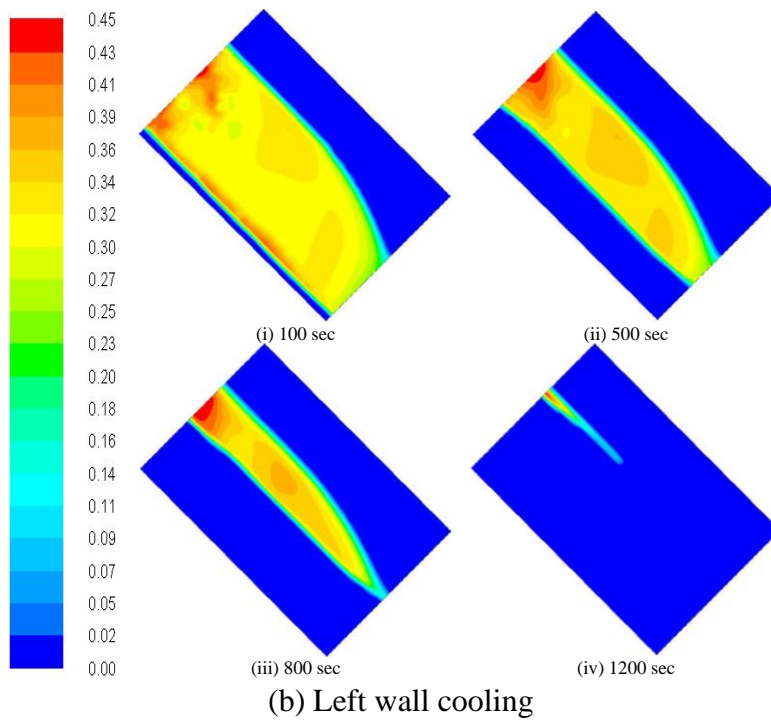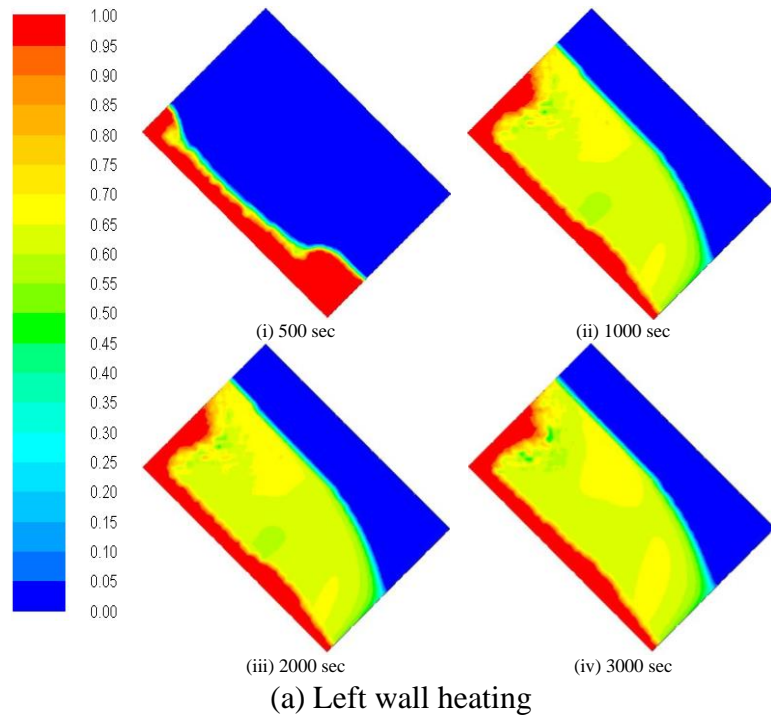
(b) Left wall cooling

Figure 4.20: Variation of melting fraction for left wall (a) heating and (b) cooling in 45˚

orientation.

4.4.11 Variation of Temperature for domain of 45° Orientation with Left Wall Heating and Cooling

Figures 4.21 (a) and (b) shows the variation of temperature for left wall heating and cooling for 45° orientation. There are no significant changes in the temperature distribution with time, at adjacent to the hot wall some wavy shapes are formed but the opposite side remained in the sub-cooled state. These wavy patterns indicate the uneven distribution of temperature over the surface of domain. Temperature distribution values are maximum at the hot wall where molten CPCM is accumulated, temperature distributions at other parts are slightly uniform due to the solid phase of CPCM. When the heat rejection process starts molten CPCM settles near the walls. It results in the uniform temperature profile, as time progresses hot spot or molten CPCM starts squeezing towards the center.

(i) 500 sec   (ii) 1000 sec

(iii) 2000 sec   (iv) 3000 sec

(a) Left wall heating

(i) 100 sec   (ii) 500 sec

(iii) 800 sec   (iv) 1200 sec
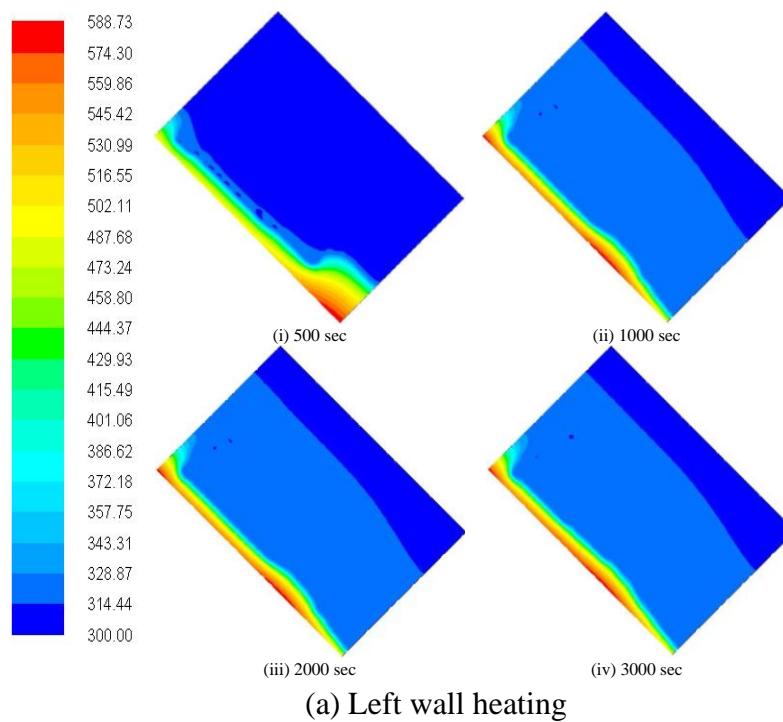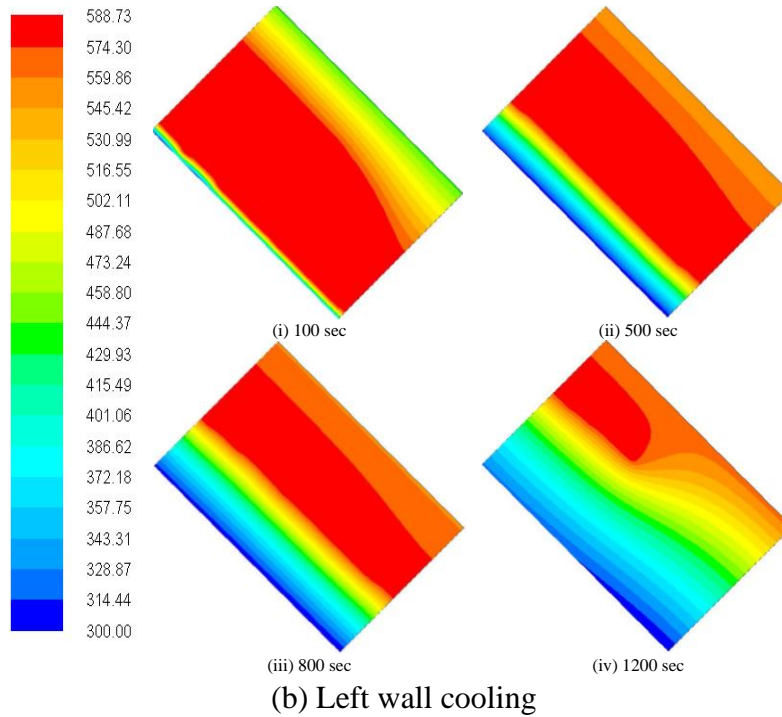
(b) Left wall cooling

Figure 4.21: Variation of temperature for left wall (a) heating and (b) cooling in 45˚ orientation.

4.4.12 Flow Characteristic Study for domain of 135˚ Orientation for Left Wall Heating and Cooling

Figures 4.22 (a) and (b) shows the variation of streamline patterns for left wall heating and cooling in 135˚ orientation. The melting process starts with the predominant effect of conduction, due to the absence of natural convection and shows vertical interface patterns among liquid and solid phases. As time proceeds, the hot fluid ascents upwards and the cold liquid next to the solid succeeds. A recirculation vortex forms on the upper half of domain and natural convection plays a dominant role. But at the bottom, conduction remains predominant in half portion of domain. The natural convection turns out to be significant and the melting rate gets faster on the upper half of domain. The CPCM changes its phases and melting rate marginally reduces in the bottom portion of domain, as the reduction of heat conduction decreases due to the expansion of fluid layer thickness and thermal resistance. The anisotropy of thermal conductivity and the crystallographic effects plays a dominant role in controlling the interface patterns.
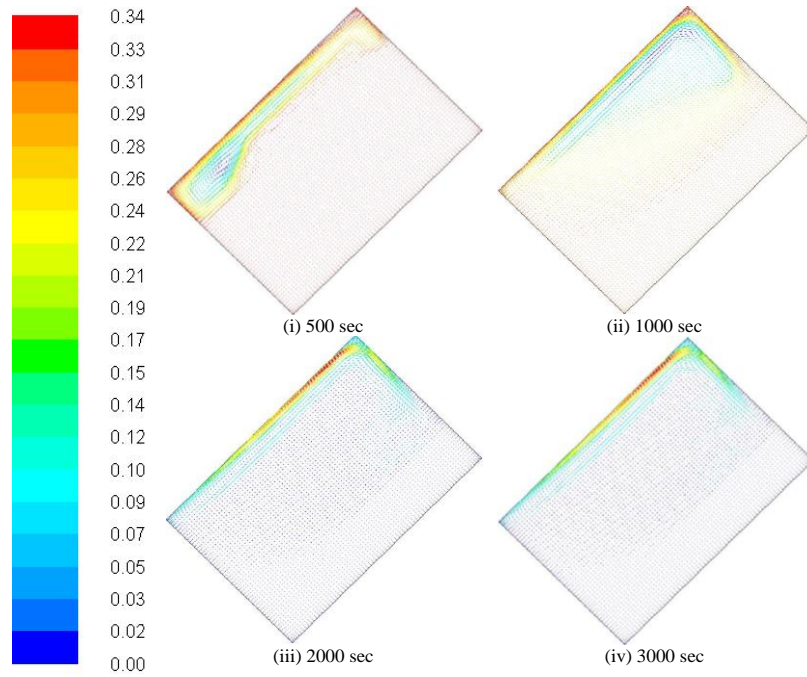
(a) Left wall heating
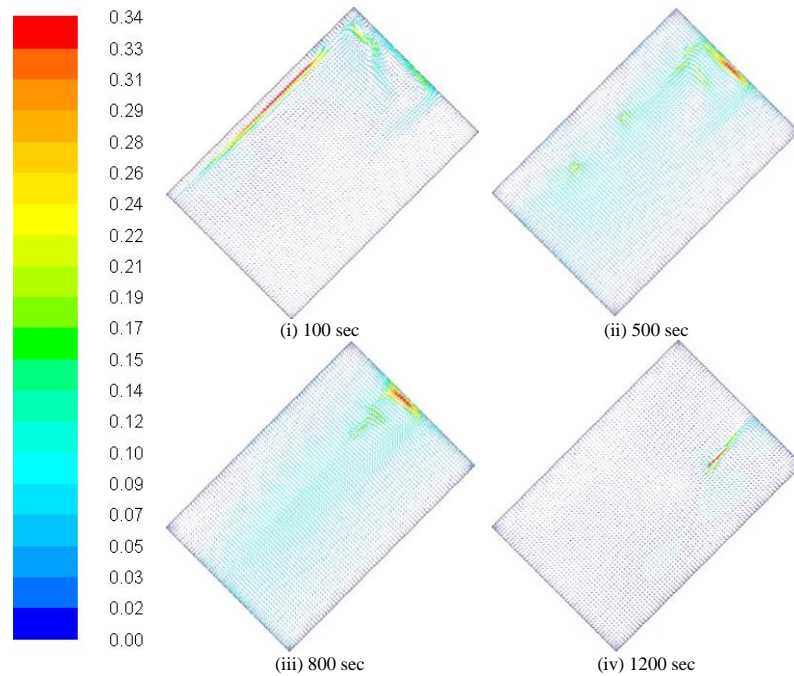
(b) Left wall cooling

Figure 4.22: Variation of streamline patterns for left wall (a) heating and (b) cooling in 135° orientation.

Completely molten CPCM forms circular vortex patterns when heat is rejected, at the completion of solidification process the streamline patterns distribute uniformly all over the domain.

4.4.13 Variation of Melting Fraction for domain of 135° Orientation for Left Wall Heating and Cooling

Figures 4.23 (a) and (b) shows the variation of melting fraction for left wall heating and cooling in 135° orientation. The highest temperature is at the hot wall and the CPCM starts melting from the hot wall since natural convection zone forms and further melts to result in the expansion of CPCM. The left wall heating is an efficient way to achieve faster melting, at the intermediate stage a small portion of the CPCM melted and the majority of domain is covered with the partial molten mushy zone.

(i) 500 sec   (ii) 1000 sec

(iii) 2000 sec   (iv) 3000 sec

(a) Left wall heating
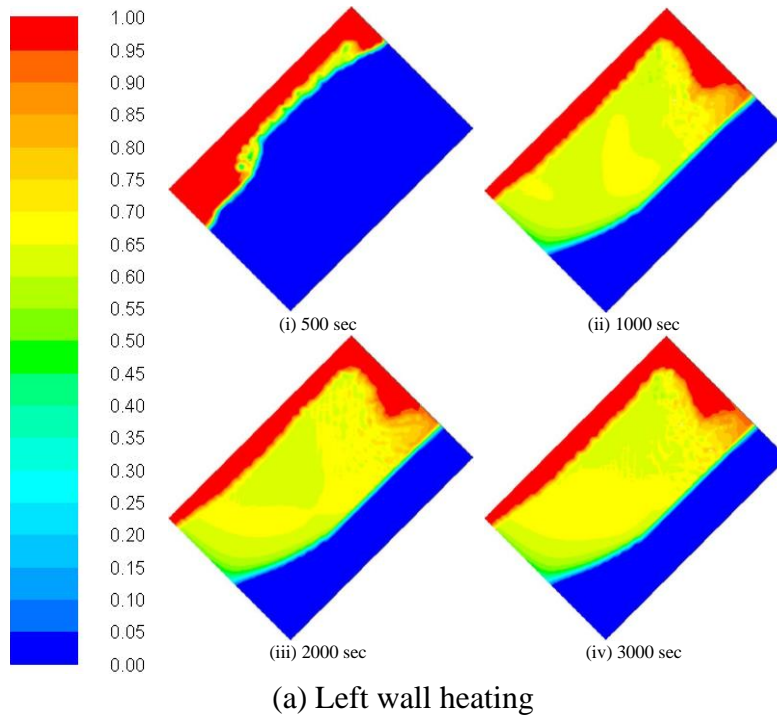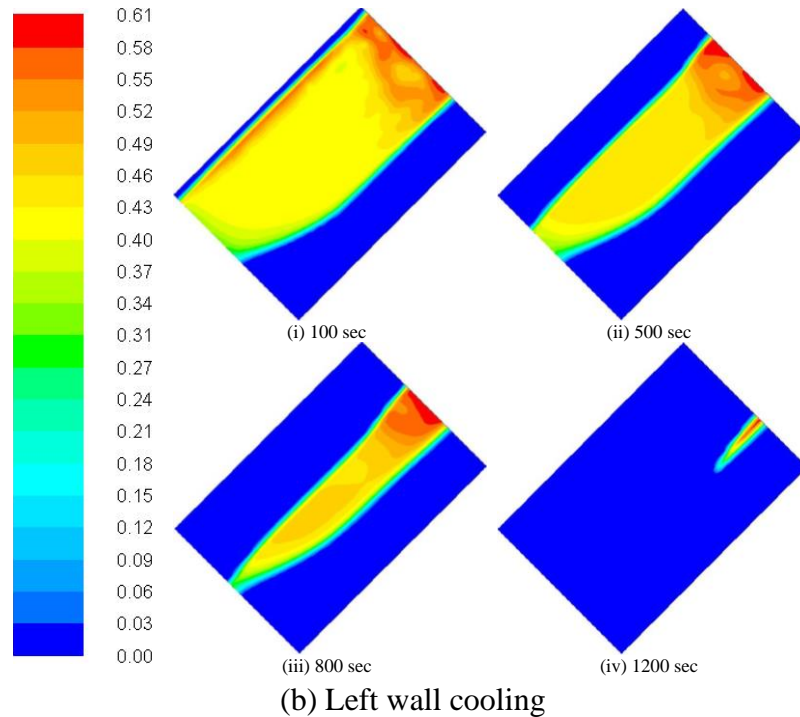
(b) Left wall cooling

Figure 4.23: Variation of melting fraction for left wall (a) heating and (b) cooling in 135˚ orientation.

4.4.14 Variation of Temperature for Domain of 135° Orientation for Left Wall Heating and Cooling

Figures 4.24 (a) and (b) shows the variation of temperature for left wall heating and cooling in 135˚ orientation. For the left wall heating, the temperature distribution is completely single sided, it shows hotspot only along the left vertical wall. The temperature distribution mimics hot wall and it spreads uniformly over the domain. The steady temperature distribution, amid the early time of the melting process. They are almost parallel to the hot wall shows that heat is transferred in the perpendicular direction to the hot wall and dominated by conduction. There is no change in the temperature distribution at the sub-cooled regions near the isothermal wall. During the cooling process, the temperature distributions are disturbed in nature and form circular patterns all around molten CPCM.

(i) 500 sec   (ii) 1000 sec

(iii) 2000 sec   (iv) 3000 sec

(a) Left wall heating

(i) 100 sec   (ii) 500 sec

(iii) 800 sec   (iv) 1200 sec
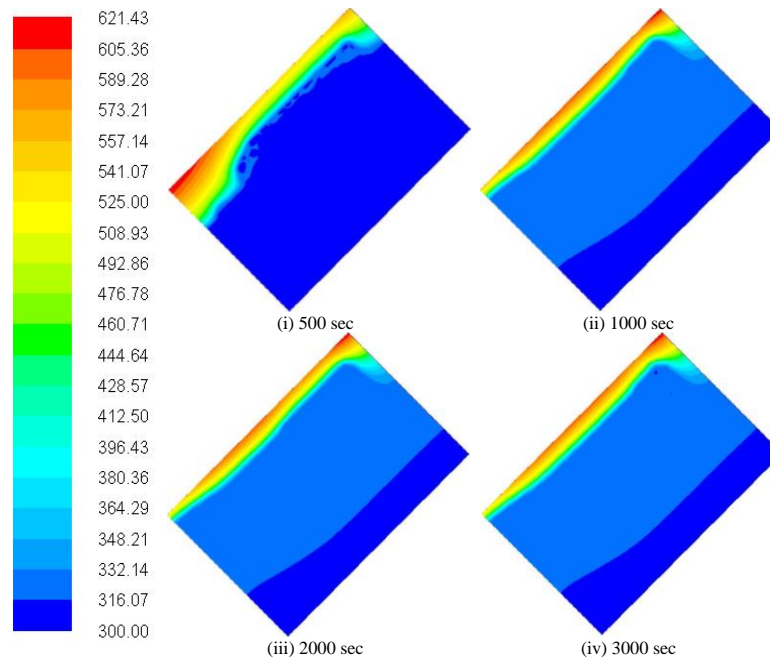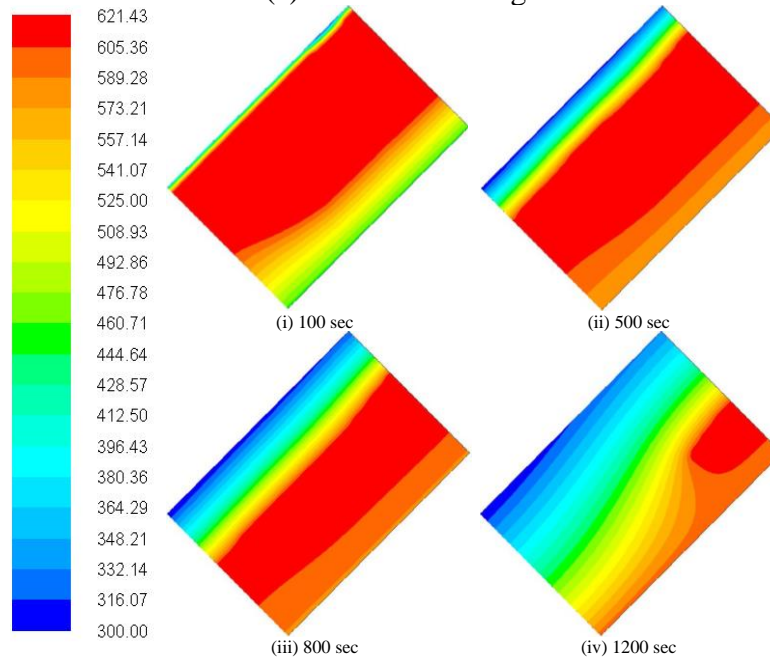
(b) Left wall cooling

Figure 4.24: Variation of temperature for left wall (a) heating and (b) cooling in 135˚

orientation.

84

4.4.15 Effect of 45° orientation and different wall heating on Thermophysical Properties

The density variation for different wall heating of 45° orientation is shown in Figure 4.25 (a). The maximum density difference is clearly observed for base wall heating compared with another wall heating. The thermal conductivity variation for 45° orientation is shown in figure 4.25 (b). For left wall heating thermal conductivity increases as time progresses, top wall heating overtakes and reaches the maximum for the same operating conditions.
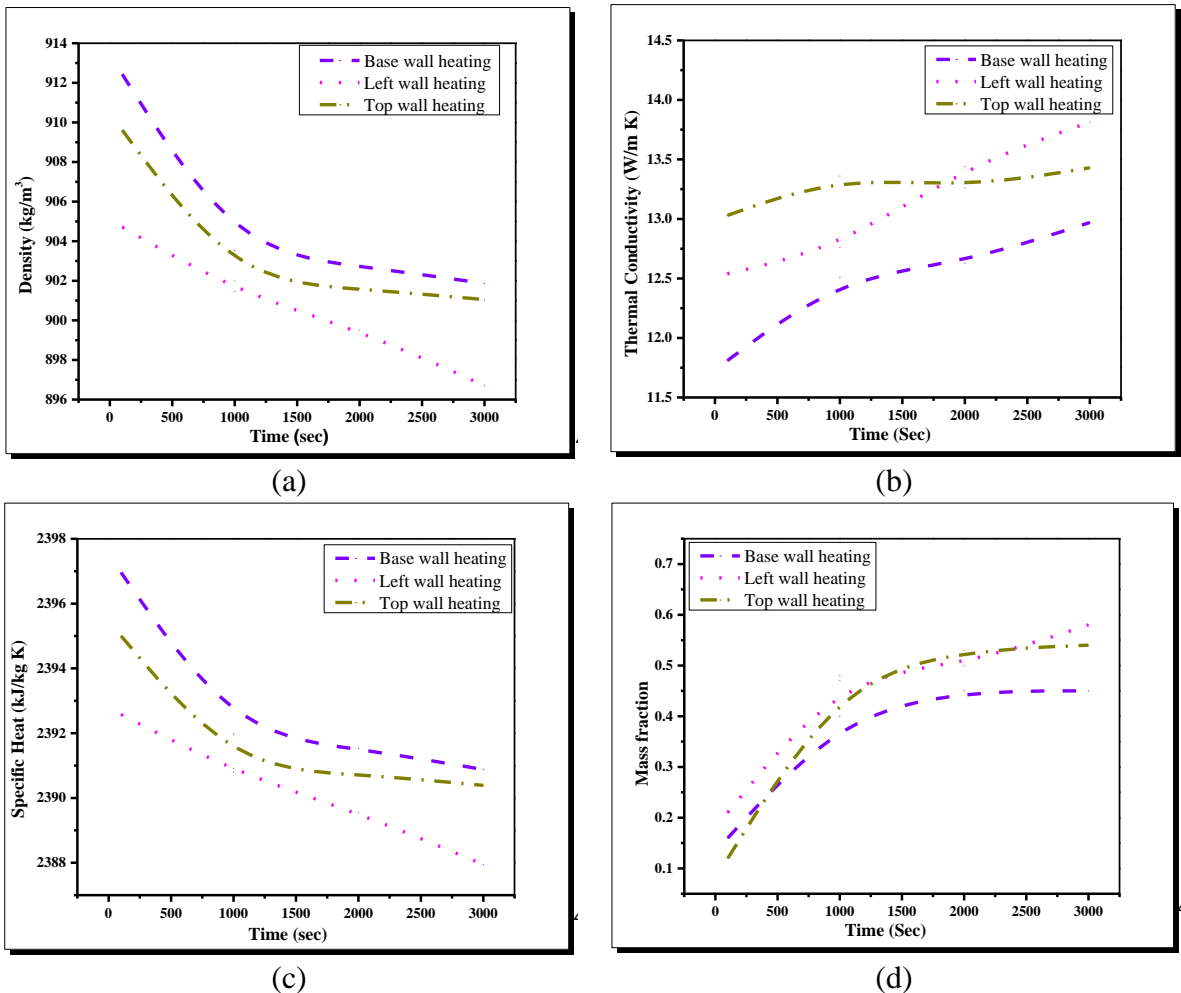
Figure 4.25: Variation of thermophysical properties in 45° orientation for different wall heating (a) density (b) thermal conductivity (c) specific heat and (d) mass fraction.

Figure 4.25 (c) shows the variation of specific heat for different wall heating, among the three, base wall heating is shown an insignificant effect. The specific heat has an inverse effect on the thermal conductivity due to higher thermal conductivity the specific heat reduces and the heat transfer within the CPCM increases. Compared to the other two cases better storability can be achieved through base wall heating. Figure 4.25 (d) shows the mass fraction variation for different wall heating. The mass fraction variation at the initial time step is almost linear for all cases, but as time progresses to 2000 sec, left wall heating shows faster melting rate. The area of melting front generated by molten CPCM is relatively more. The same amount of heat is supplied, the melting rate is slow due to lack of contact between the melting front and the sub-cooled fluid.

4.4.16 Effect of Shallow Domain for different wall heating

The effect of the shallow domain for different wall heating is discussed in this section. Figures 4.26 (a) and (b) shows the density and thermal conductivity variations for different wall heating. The heat interaction area is more so that the formation of molten layer is high. Increase in melting fraction leads to density reduction for left wall and the same for the base and top wall. Figures 4.26 (c) and (d) shows the specific heat and mass fraction variations for different wall heating. Mass fraction developed is high for the left wall heating, and it is same to right wall heating. For thermal conductivity variation, left and right wall heating causes the same effect on domain, the highest value for thermal conductivity is same.

(a) (b)

Specific Heat (kJ/kg K)

2410
2400
2390
2380
2370
2360
2350
2340

--- Base wall heating
···· Left wall heating
—·— Top wall heating

0   500   1000   1500   2000   2500   3000
Time (sec)

Mass fraction

0.7
0.6
0.5
0.4
0.3
0.2
0.1

--- Base wall heating
···· Left wall heating
—·— Top wall heating

0   500   1000   1500   2000   2500   3000
Time (Sec)

(c) (d)
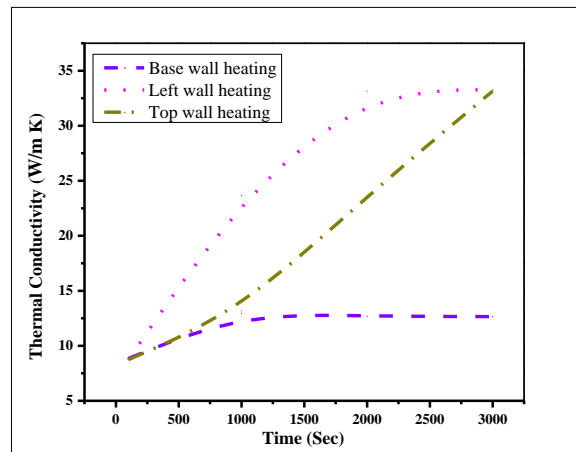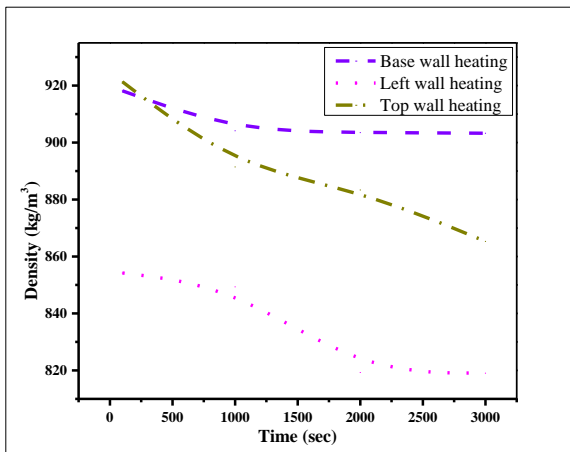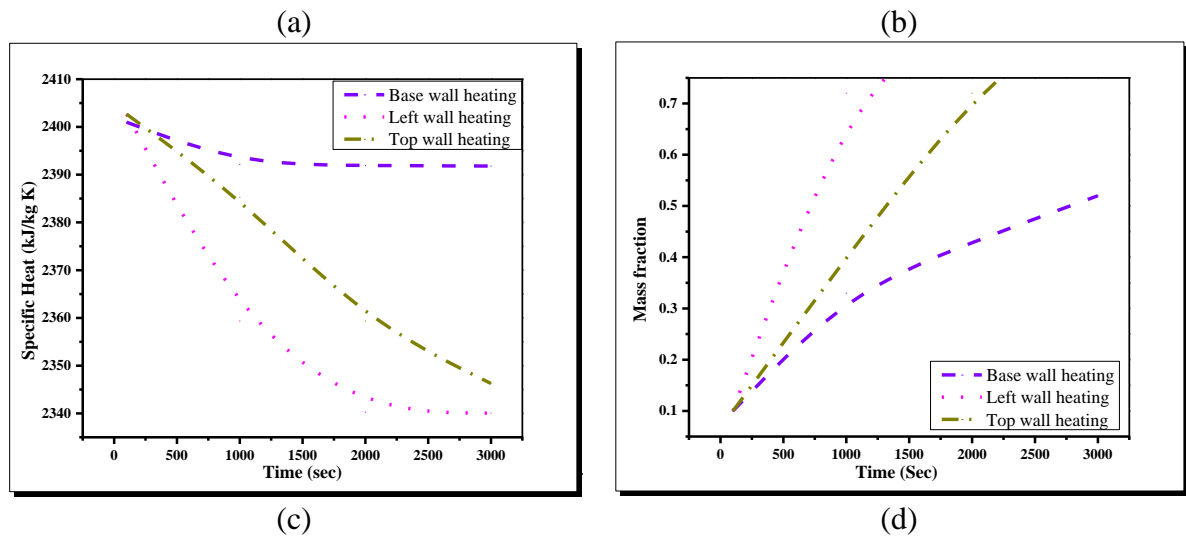
Figure 4.26: Variation of thermophysical properties in 180° orientation for different wall heating (a) density (b) thermal conductivity (c) specific heat and (d) mass fraction.

As thermal conductivity increases the CPCM releases the stored heat efficiently, and it leads to faster discharging of heat. Among the three, top wall heating is shown moderate values for the melting and heat-releasing duration by storing heat for a more extended period.

4.4.17 Top wall heating characteristics for different orientations

The top wall heating exhibits comparatively better results, as compared to base and left wall heating. Top wall heating for all the orientations are further analyzed as shown in figures 4.27 (a)-(c). The mass fraction variation in deep and shallow domains are much better and reaches maximum (0.9) at 2000 sec, as seen in figure 4.27 (a). The mass fraction for 45° and 135° orientations are not shown any significant change and maximum value reaches upto 0.65 after 3000 sec of heating time.

The variation in specific heat for 45° and 135° are almost constant for all cases of heating time as shown in figure 4.27 (b). The variation in deep and shallow domain shows changes and decreases with heating time. The specific heat value drastically reduces for deep domain and reaches to least value at 3000 sec. The increase in liquid phase thermal conductivity is due to the increase in mass fraction. For deep domain, the increase in mass fraction upto heating time 1500 sec is linear (0.1 to 0.4) and thermal conductivity also

linearly increases (7 to 15 W/m K). After 1500 sec to 3000 sec mass fractions increases drastically (0.4 to 1.0) and thermal conductivity also follows the same trend (15 to 45 W/mK).

(a)

(b)

(c)
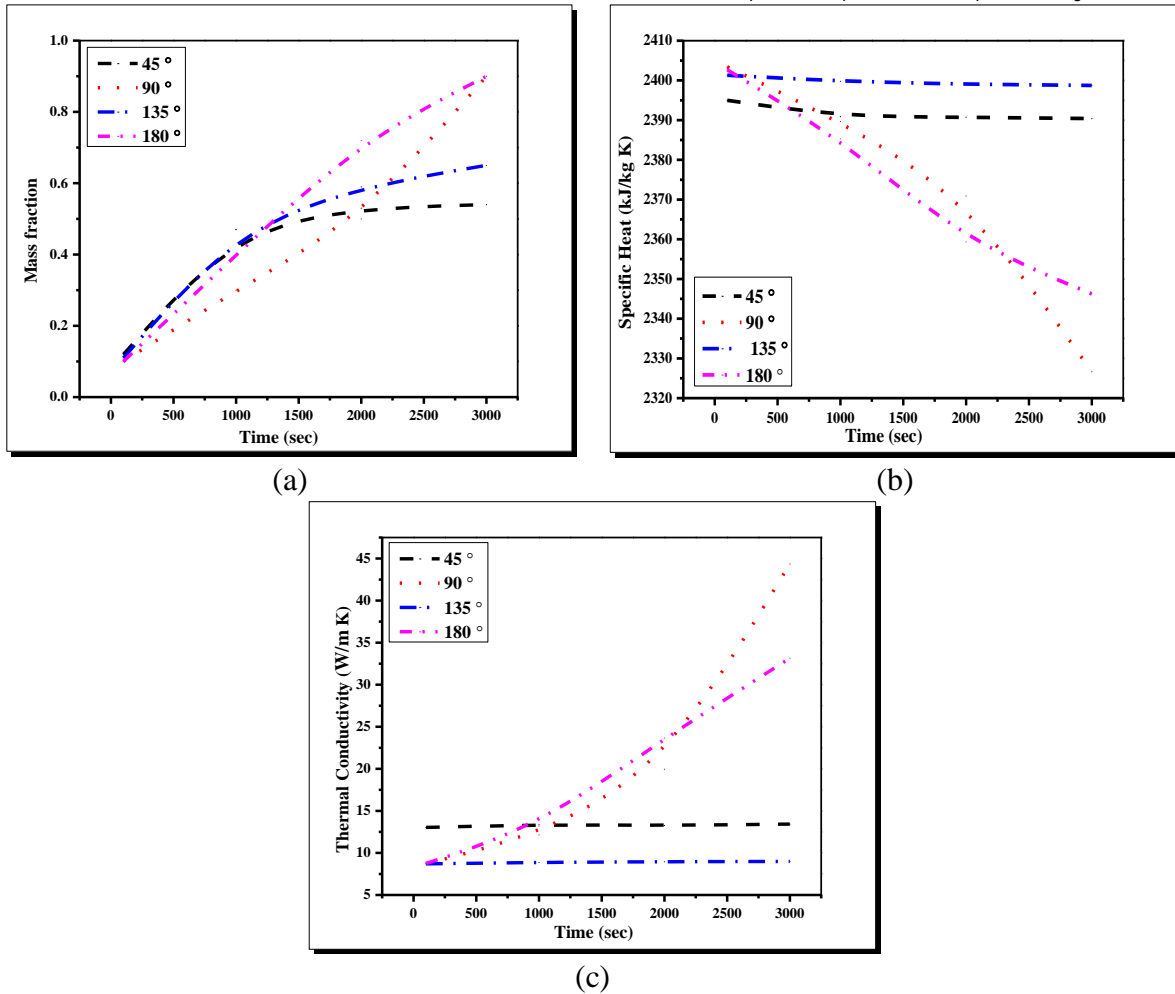
Figure 4.27: Comparison of melting characteristics for top wall heating (a) mass fraction (b) specific heat and (c) thermal conductivity variation with different orientations.

Thermal conductivity and specific heat are inversely proportional properties, for deep and shallow domains thermal conductivity is maximum and reaches up to 45 and 35 W/mK. After 3000 sec of heating time for 45° and 135° orientations, the variation of thermal conductivity is negligible and remained constant throughout the melting process. All the cases studied are listed in Table 4.2, which shows comparative results of melting / solidification characteristics of CPCM for different orientations and wall heating cases.

4.5 EFFECT OF DOMAIN GEOMETRY ON MELTING AND SOLIDIFICATION CHARACTERISTICS

Next, a numerical study is continued for different domain geometries to analyze the melting/solidification characteristics of CPCM. Thermal energy storage units are modeled with three different domains such as square, pentagon, and hexagon, to study the effect of domain geometry on heating and cooling characteristics.

4.5.1 Problem Description

Three different domains are modeled such as square, pentagon, and hexagon to study the effect of geometry on heating and cooling characteristics as shown in figure 4.28. The TSM used for the investigation is CPCM (a mixture of 98% of paraffin and 2% Al_2O_3 nanoparticles). The volume of the domain is constant (0.01 m^3), and the amount of heat supplied is 1000 W for all cases.
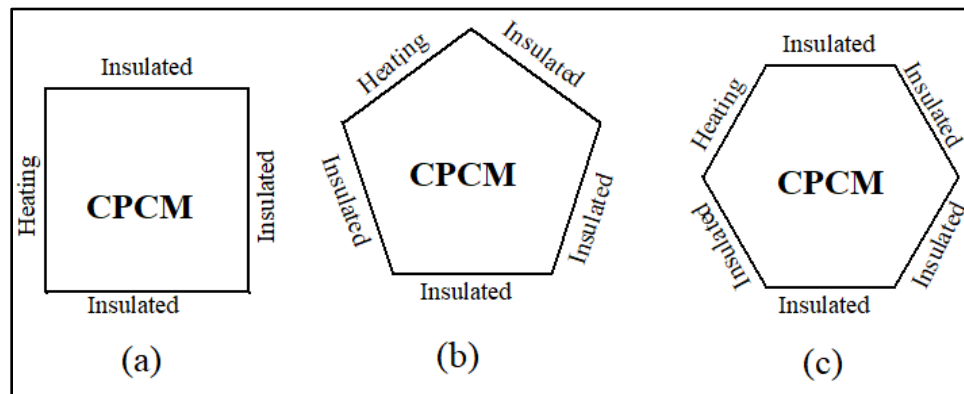
Figure 4.28: Geometrical representation of computational domains, (a) square, (b) pentagon and (c) hexagon domains.

4.5.2 Boundary Conditions

For heating cycle, constant heat is supplied through the left wall for square domain, the upper left wall for pentagon, and hexagon domain. For cooling cycle, heat is rejected through the right wall for square domain and lower right wall for pentagon and hexagon domain. Remaining walls are kept insulated condition.

Table 4.1: Comparison of melting/solidification characteristics of CPCM for different orientation and wall heating cases.

Parameters	Time (sec)	45° Orientation			90° Orientation			135° Orientation			180° Orientation		
		Base wall heating	Left wall heating	Top wall heating	Base wall heating	Left wall heating	Top wall heating	Base wall heating	Left wall heating	Top wall heating	Base wall heating	Left wall heating	Top wall heating
Average density (kg/m^3)	500	912	905	910	923	909	923	919	903	921	918	854	921
	1000	903	901	902	900	902	900	916	896	919	904	849	891
	2000	903	900	902	852	902	869	916	894	917	904	819	883
	3000	905	897	901	800	902	800	915	893	916	903	819	865
Average thermal conductivity (W/m K)	500	11.81	12.54	13.03	8.73	12.37	8.73	8.88	14.30	8.70	8.85	8.75	8.75
	1000	12.51	12.76	13.36	12.15	13.22	12.15	8.94	15.08	8.88	12.96	23.66	13.19
	2000	12.63	13.44	13.26	25.01	13.18	19.95	8.97	13.66	8.96	12.69	33.15	23.66
	3000	12.97	13.81	13.43	44.24	13.12	44.35	9.08	14.30	8.99	12.65	33.27	33.15
Average specific heat (kJ/kg K)	500	2397	2393	2395	2403	2395	2403	2401	2393	2401	2401	2403	2403
	1000	2392	2391	2391	2390	2391	2390	2400	2389	2400	2392	2359	2385
	2000	2392	2390	2391	2361	2391	2371	2400	2388	2399	2392	2340	2359
	3000	2394	2388	2390	2327	2391	2327	2399	2388	2399	2392	2340	2346
Average mass fraction	500	0.16	0.21	0.12	0.10	0.15	0.10	0.13	0.18	0.11	0.10	0.10	0.10
	1000	0.40	0.48	0.47	0.30	0.44	0.30	0.40	0.51	0.47	0.33	0.72	0.40
	2000	0.45	0.50	0.53	0.61	0.46	0.50	0.49	0.57	0.59	0.43	0.90	0.72
	3000	0.45	0.69	0.54	0.90	0.47	0.90	0.53	0.68	0.65	0.52	0.90	0.90

4.5.3 Flow Characteristic Analysis of different Domains during Heating Process

The complete heating and cooling processes are analyzed by dividing it into four-time steps such as 1000, 2000, 3000, and 4000 sec. The streamline patterns developed during the complete melting process is shown in figure 4.29. It is seen that for different geometries at different time intervals are not similar. In the square model, the streamline pattern movement starts from the top portion of the hot vertical wall and spreads the upper region of the domain. As melting progresses, the streamline patterns occupy a half portion of the domain, which indicates the movement of convection currents. At the beginning streamline patterns form circulation vortices as time progresses it enlarges and forms two different circulation vortices.
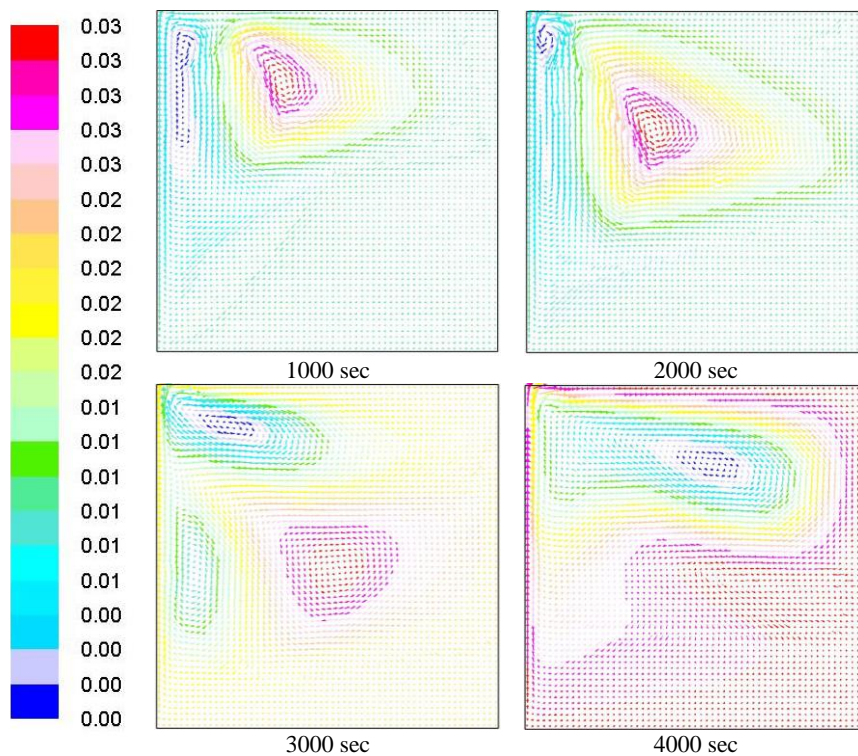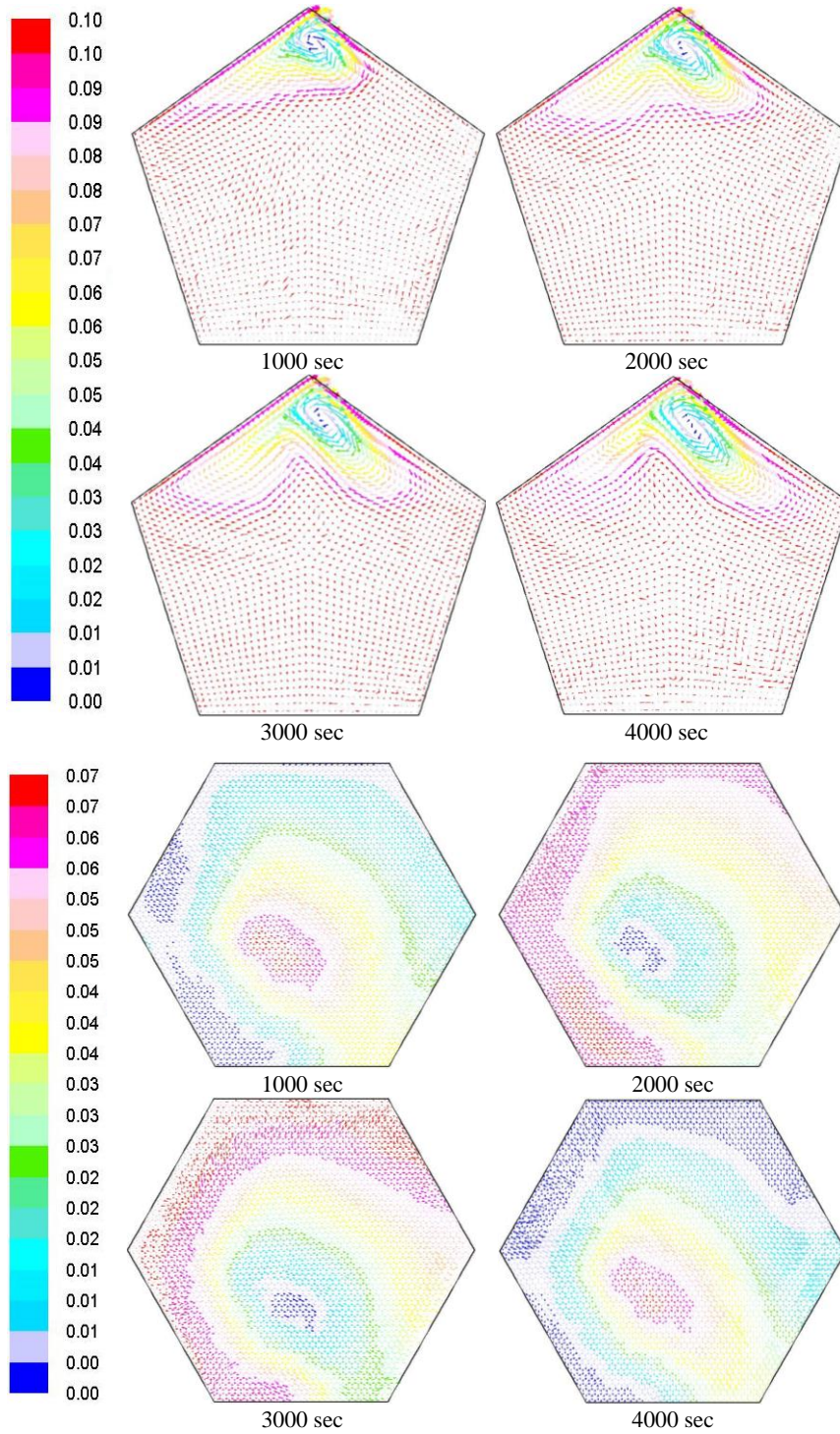
Figure 4.29: Streamline patterns developed in different geometrical models during the
heating process.

The streamline patterns in the pentagon model is varies and concentrate at the top edge of the domain. Continuous convection currents make the streamline patterns to circulation and concentrate at the top edge portion of the domain. The circulation vortices form cyclone like structures. The heating process proceeds, the vortex size starts enlarging and forms symmetry from the top edge. This circulation vortex indicates the transfer of convection currents through the hot region to colder region of the domain. Streamline patterns of hexagon model does not show any change throughout the melting process due to uniform structure and uniform temperature distribution. As the supplied heat gets absorbed immediately without creating any turbulence in the domain.

4.5.4 Variation of Liquid Fraction in different Domains during Heating Process

Figure 4.30 shows the variation of liquid fraction in different domains during the heating process. The conduction dominated melting process yields similar liquid fraction irrespective of the geometry. In the melting process, natural convection influences significantly, and it changes the melting rate depends on the geometries. The square geometry provides complete melting within the time interval with non-uniform patterns of molten CPCM. The pentagon domain takes a longer time for completion due to the low melting rate. The hexagon model initially shows a slow melting rate, as time progresses, the melting front travels quicker and completes the melting process uniformly. It is desirable to select the hexagon model to maintain and improve heat transfer through natural convection.

The analysis of liquid fraction is carried out to understand the faster heating capability of different models. Among three models, the square model reaches an average liquid fraction of 0.43, 0.78, 0.81, and 0.91 for time intervals of 1000, 2000, 3000, and 4000 sec respectively. Pentagon model reaches average liquid fraction quickly, at a later stage it drastically reduces the average liquid fractions for different time duration are 0.65, 0.34, 0.54 and 0.59 for 1000, 2000, 3000 and 4000 sec of time intervals respectively. The maximum value obtained is 0.59, and heating continued till 8000 sec, but the average liquid fraction reaches 0.66 only. The hexagon model initially reaches a low value of the liquid fraction, but as heating progresses, it abruptly increases and reaches to highest value among

the three models. The average liquid fraction values at different time intervals are 0.45, 0.72, 0.86 and 1.0 for 1000, 2000, 3000 and 4000 sec respectively. To achieve complete and uniform heating, the hexagon model can be preferred.
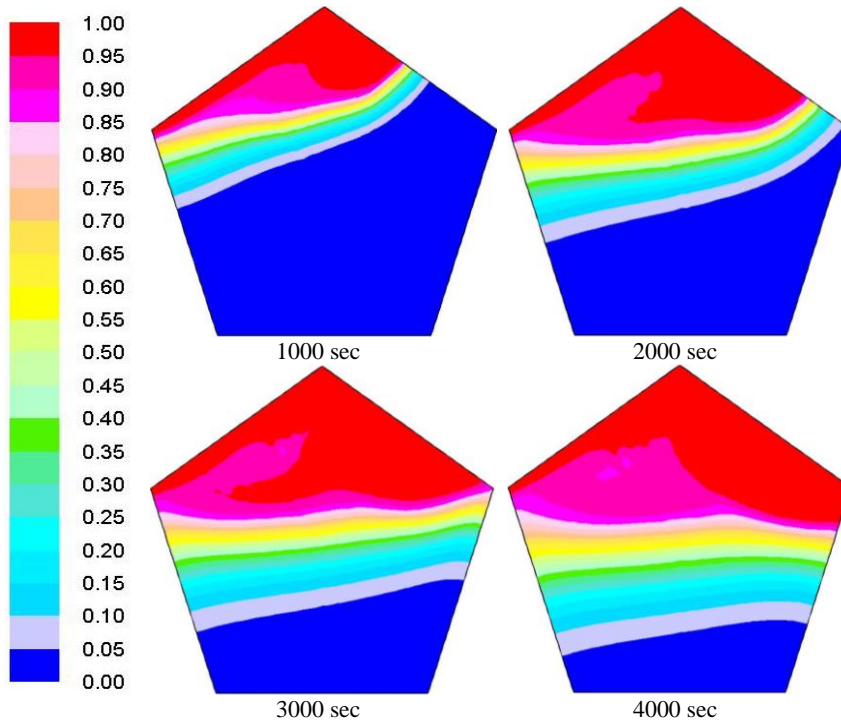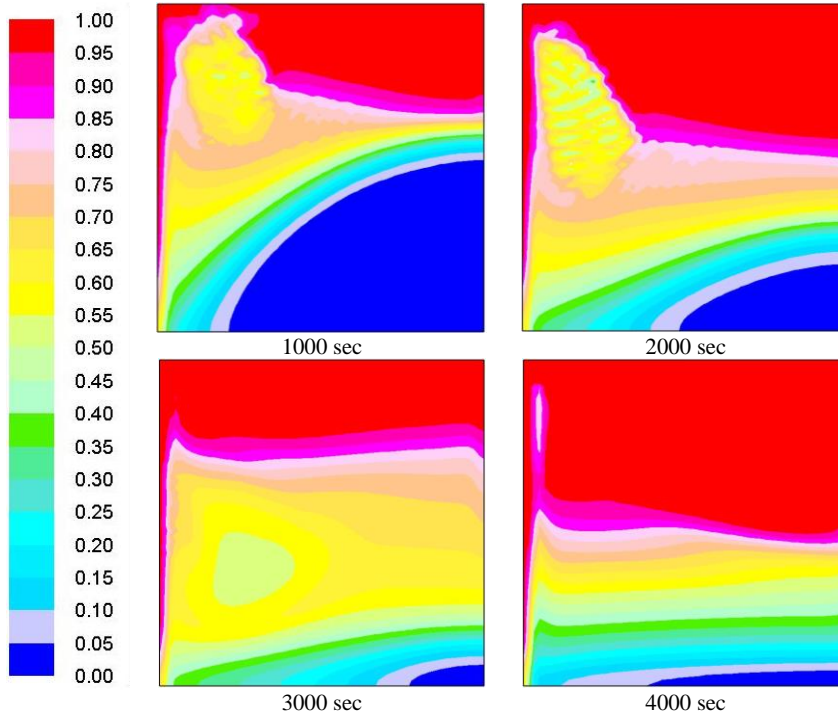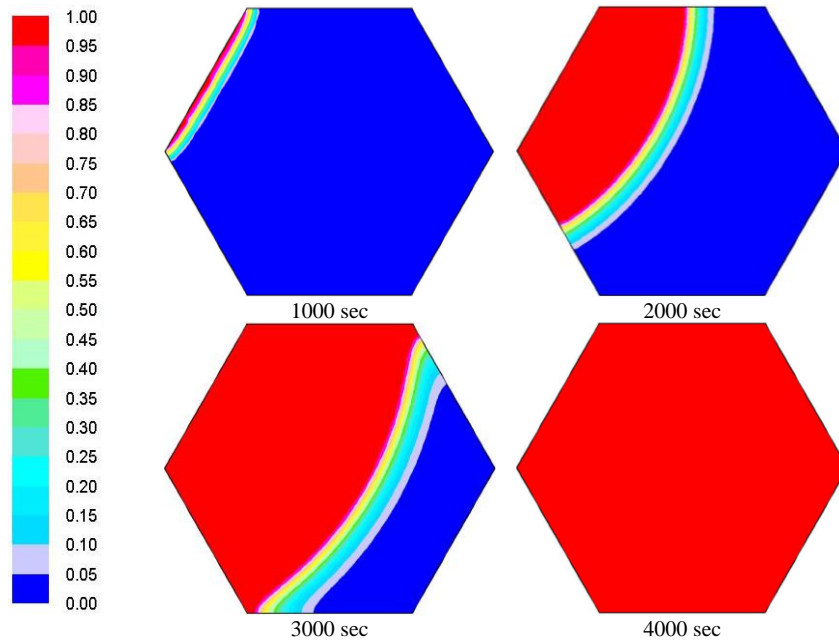
Figure 4. 30: Variation of liquid fraction in different domains during the heating process.

As heating proceeds, the melting front develops and gets intensified due to buoyancy-driven convection heat transfer. A flow pattern of natural convection accelerates the phase change process, the hot fluid moves away from the wall. The melting layer flow deflects and slopes along with the solid-liquid interface with higher melting rates at high temperatures regions. As the melting layer occupies the upper surface of the solid material and it gets accelerated due to high thermal conductivity. The recirculation of natural convection currents developed in the molten CPCM becomes more intense with time and reduces the melting rate adjacent to the cold region.

4.5.5 Variation of Temperature in different Domains during Heating Process

For all the geometrical models the interface patterns and the flow field near the hot wall, the temperature distributions are the same for melting and solidification due to formation of natural convection currents. The maximum temperature is observed along the hot wall, and the reverse trend of temperature distribution is seen at the solid-liquid interface. The temperature along the hot and cold wall is almost steady at the center of the domain and it

forms irregular structure. Uniform temperature distribution along the hot and base walls are observed due to heat conduction in the solid region. Natural convection initiates and plays a significant role in controlling the melting process at later stages when the temperature gradient in the solid is relatively low.

The temperature distribution is uniform for all models, the temperature is maximum for the hexagon model. In square model, temperature variation occurred is 318.08, 326.07, 328.32, and 329.07 K for 1000, 2000, 3000, and 4000 sec of time intervals respectively. Pentagon model shows temperature variation in the order of 331.85, 333.95, 334.83 and 336.6 K respectively for different time intervals. Hexagon model shows a maximum temperature of 323.07, 349.19, 362.24, and 390.35 K respectively for different time intervals. The temperature values represent the amount of heat energy stored in the hexagon model is relatively high compared to the remaining two models.
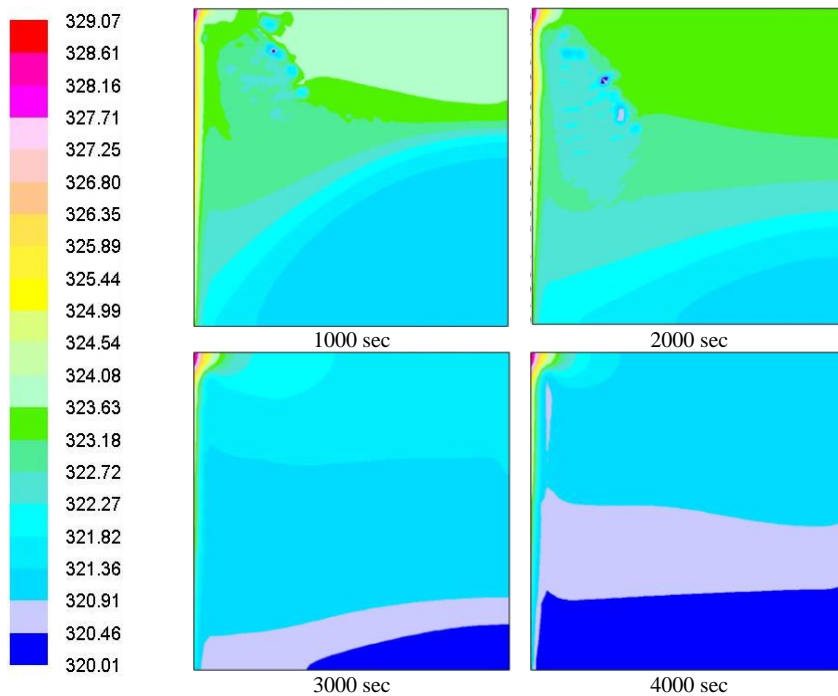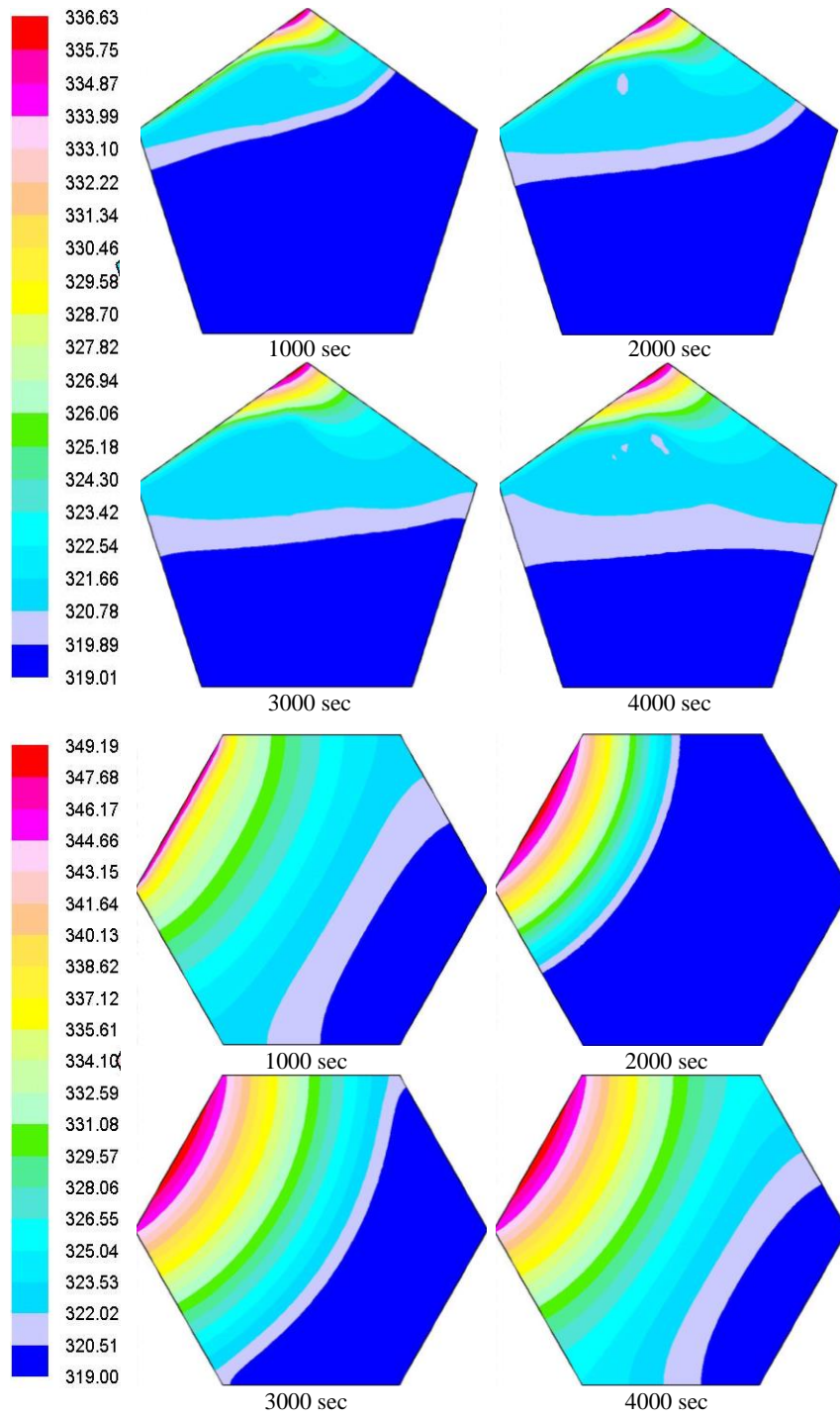
Figure 4.31: Variation of temperature in different domains during the heating process.

The temperature distribution in the square model is entirely chaotic and non-uniform patterns. Pentagon model also exhibits the non-uniform patterns, but the hexagon model

shows a uniform and regular pattern for all the stages of the melting process. Temperature distribution patterns from the cold wall (base wall) are the same for all the cases, and it can be visualized from figure 4.31. It is understood that to achieve a uniform and efficient heating hexagon model is a favorable one.

4.5.6 Flow Characteristic Analysis in Different Domains during Cooling Process

The cooling process is initiated by stopping the heat supply and insulating the hot wall, on the other hand, constant heat rejection is applied from the right wall (for square model) and the lower right wall (for pentagon and hexagon model). The Streamline patterns developed in different geometrical models during the cooling process is shown in figure 4.32. To understand the physics involved in the complete cooling mechanism is divided into 4-time steps such as 1000, 2000, 3000 and 4000 secs respectively.
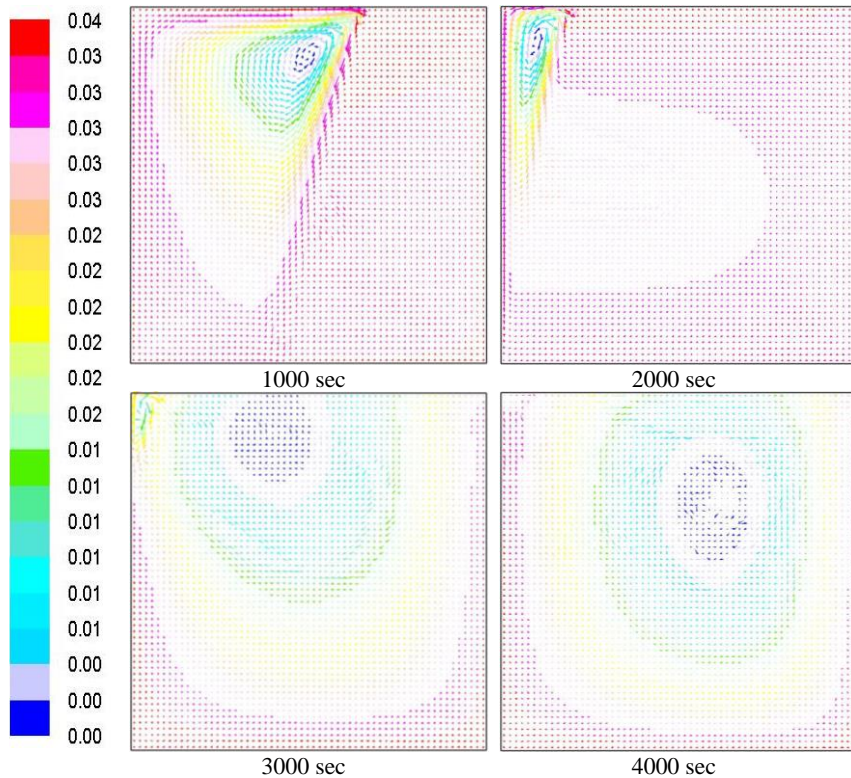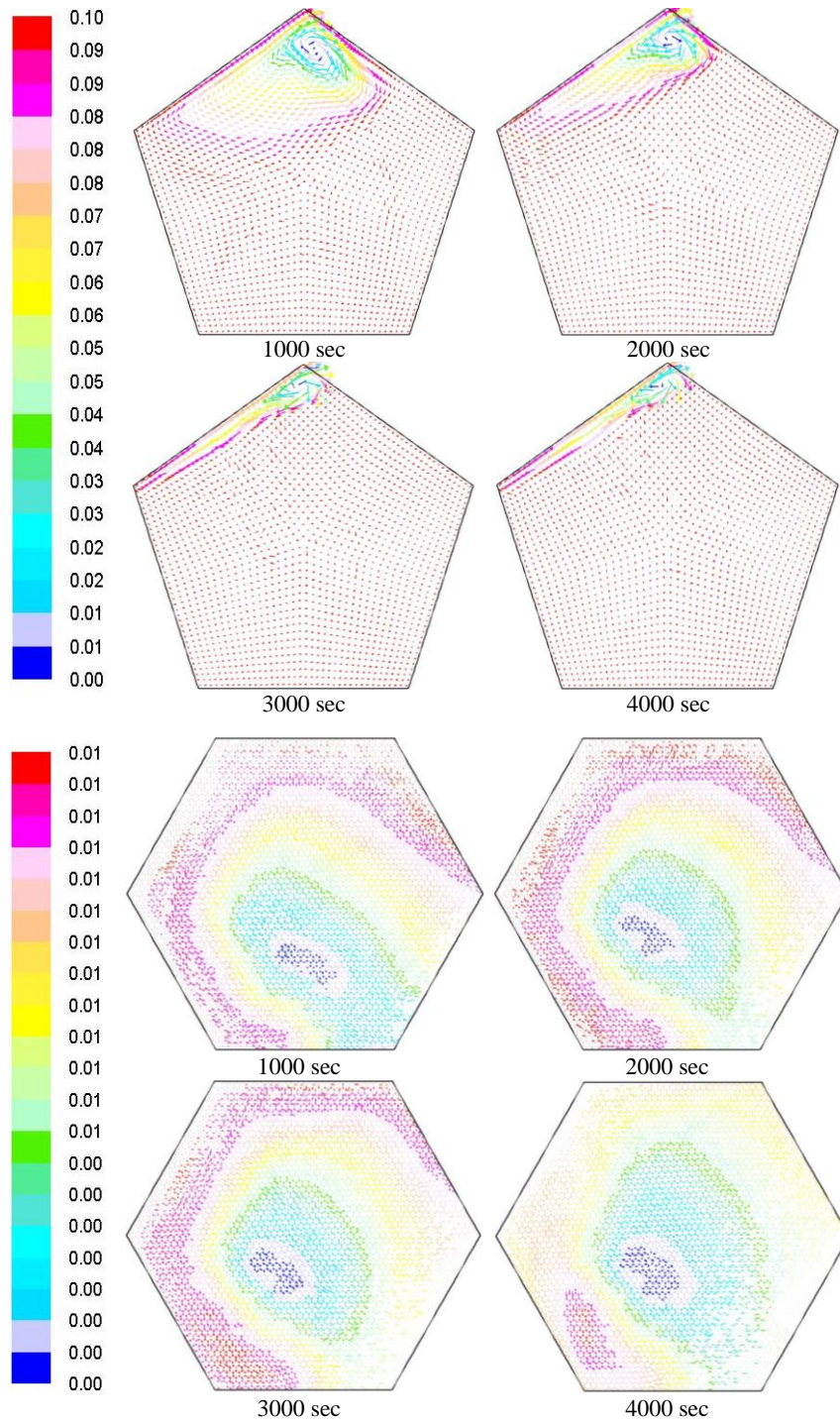
Figure 4.32: Streamline patterns developed in different geometrical models during cooling process.

In square model streamline patterns start contracting with quicker rate, the flow occupies around half portion of the domain, and it forms cyclic/ circulation vortices. As time proceeds, the streamline patterns are concentrated at the top portion of the left wall and at the completion of the cooling process it disappears. For the pentagon model initially, the streamline patterns are distributed at the top center position in circulation vortex formation. As time progresses the streamline patterns accelerate parallel to the hot wall, continuous cooling reduces to the chaotic distribution of streamline patterns and restricts their movements. The hexagon model does not show any changes in the streamline patterns throughout the cooling process. This is due to the uniform distribution of temperature and streamline patterns seems to be insignificant for the hexagon model.

4.5.7 Variation of Liquid Fraction in different Domains during Cooling Process

The liquid fraction variation during complete cooling process for different models can be seen from figure 4.33. The square model exhibits a faster rate for the cooling process by freezing quickly the average liquid fraction during the complete cooling process is 0.70, 0.38, 0.07, and 0.01 for 1000, 2000, 300, and 4000 sec respectively.
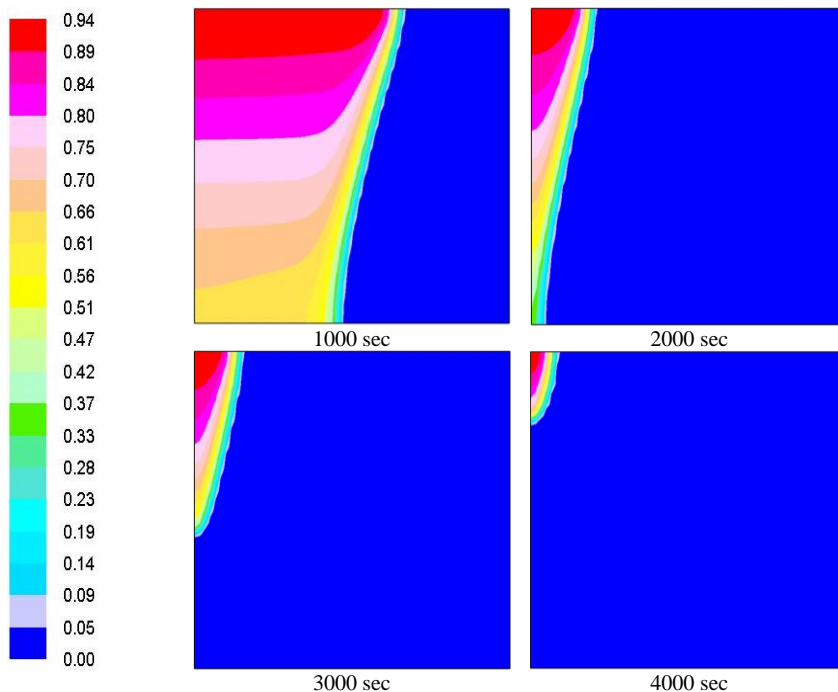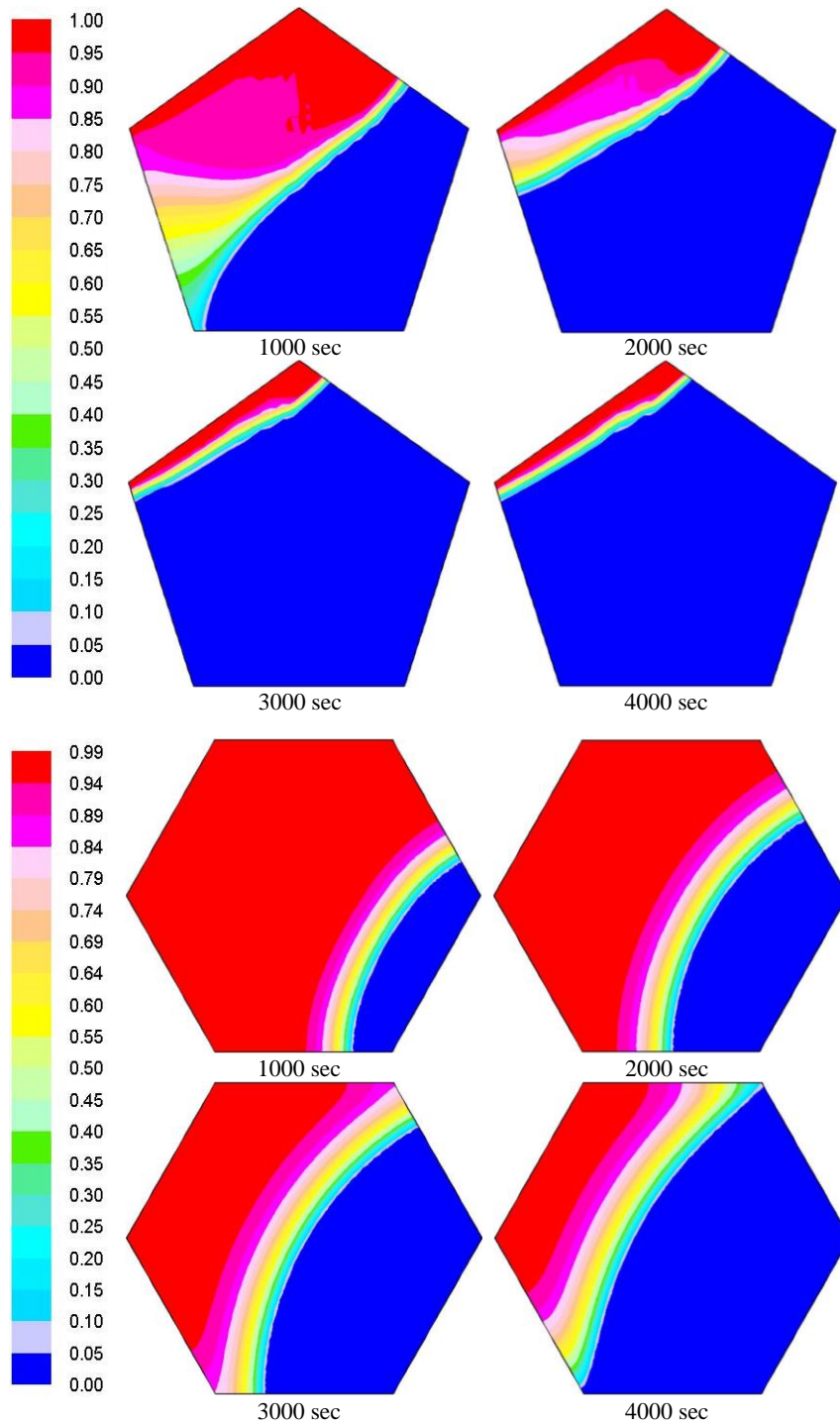
Figure 4.33: Variation of liquid fraction in different domains during the cooling process.

Pentagon model shows lower values for the cooling process such as 0.41, 0.21, 0.17, and 0.09 respectively for different time intervals. This model requires more time to reach the minimum liquid fraction. Hexagon model exhibits better results among three models by providing uniform and complete cooling. Compared to square hexagon model takes more time to discharge compared to the pentagon model because it rejects heat with a faster rate. The average liquid fraction values are 0.80, 0.63, 0.48, and 0.36 respectively for different time intervals, and the cooling process completes after 6000 sec of time interval.

4.5.8 Variation of Temperature in different Domains during Cooling Process

The Temperature distribution patterns in different geometrical models during the cooling process are shown in figure 4.34. In the square model, the temperature distribution is uniform and parallel to the cold wall, and the maximum temperature drops 320.29 to 203 K for complete cooling. In the pentagon model, the temperature distribution is uniform and gradually varying from the cooling wall, the average temperature drops 312.62 to 291.2 K.
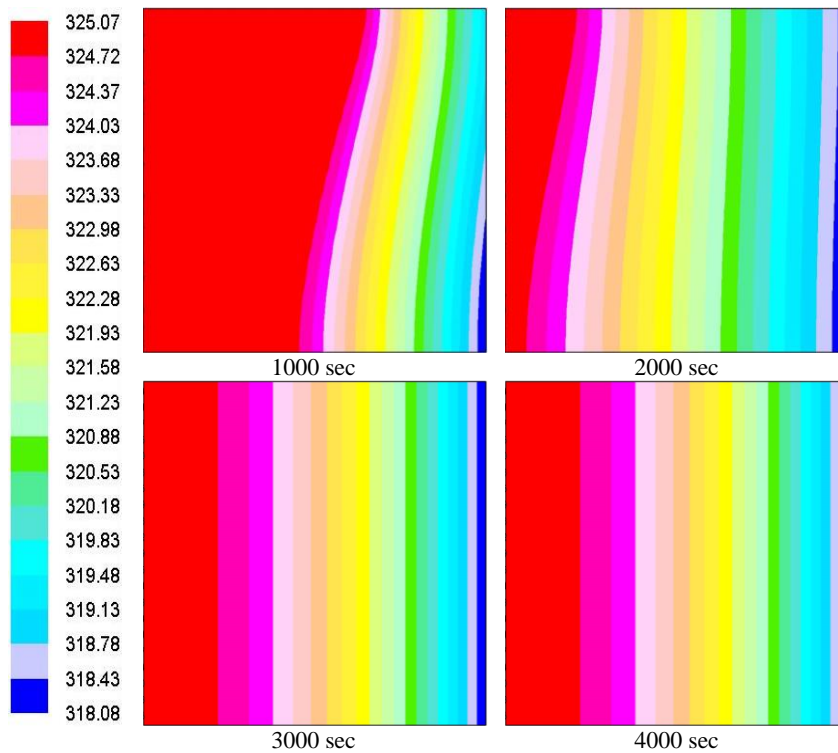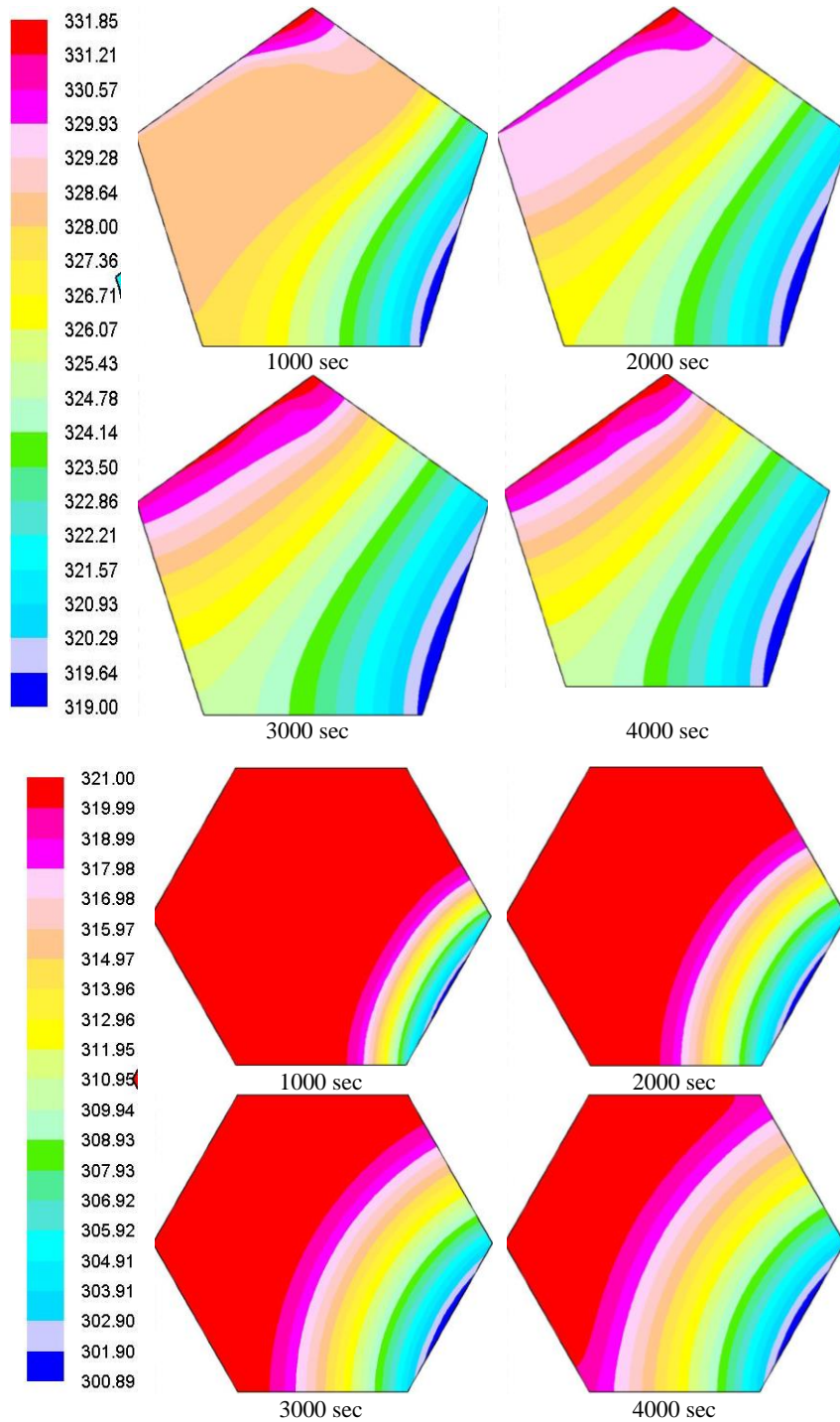
Figure 4.34: Variation of temperature in different domains during cooling process.

In hexagon model temperature distribution is uniform than the other two models. The average temperature reduced from 320.17 to 314.72, it lies in between the square and pentagon models. Among the three model's maximum temperature drop is observed for the square model around 36%, for a pentagon it is around 6, and for hexagon, it is around 3.38% during the complete cooling process. The temperature drop is least due to the storage of heat energy in the form of latent heat.

4.5.9 Comparison of Heating and Cooling Characteristics

The average mass fraction variation with time for heating and cooling cycle can be visualized from Figures 4.35 (a) and (b). Square model absorbs heat very quickly, and it rapidly increases with the liquid fraction. Complete melting of the square, pentagon, and hexagon model requires 3500, 8000, and 4000 sec of time duration respectively. Faster melting rate occurs in the square model compared to pentagon and hexagon models. For optimum heating and cooling applications, the hexagon model is preferred due to the low-temperature drop and low melting time requirement.

(a)   (b)
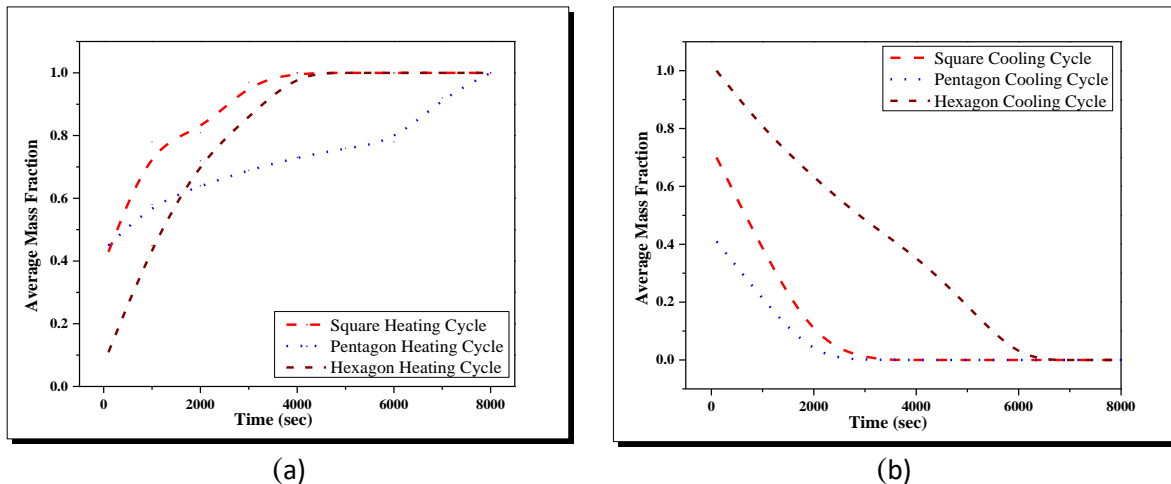
Figure 4.35: Variation of liquid fraction during (a) heating and (b) cooling process in different domains.

In the cooling cycle, the liquid fraction of square is 0.67 and hexagon is 1.0 whereas pentagon is taken as 0.40. The square model is very steep and reaches solid-state rapidly as compared to pentagon and hexagon models. Square and pentagon model follows the

same trend, but pentagon requires more time duration. In hexagon model cooling is uniform vary with a maximum time requirement of 6000 sec.

4.6 CLOSURE

In this chapter, the effect of different parameters such as nanoparticle concentration, domain geometries, and domain orientations with different wall heating conditions on melting and solidification characteristics are discussed in detail. The computational models and the numerical procedure also provided.

CHAPTER 5

MATERIAL CHARACTERIZATION AND THERMAL STORAGE ANALYSIS OF CPCM

5.1 INTRODUCTION

In the present chapter, different analysis is carried to ensure specific functionality and properties. Fourier transform infrared spectrometry analysis is performed for graphene and functionalized graphene to confirm the carboxyl group functionalization. Scanning electron microscopy analysis is carried out to ensure the uniform particle distribution, and differential scanning calorimetry analysis is performed to understand the thermophysical properties variation with different concentrations of nano additives such as 1, 3, 5% and these are referred as CPCM-1, CPCM-2, and CPCM-3.

5.2 FOURIER TRANSFORM INFRARED SPECTROMETRY (FTIR) ANALYSIS

The FTIR spectra of pure graphene and carboxyl functionalized graphene are estimated using Jasco FTIR 4200 series spectrometer.

(a)   (b)
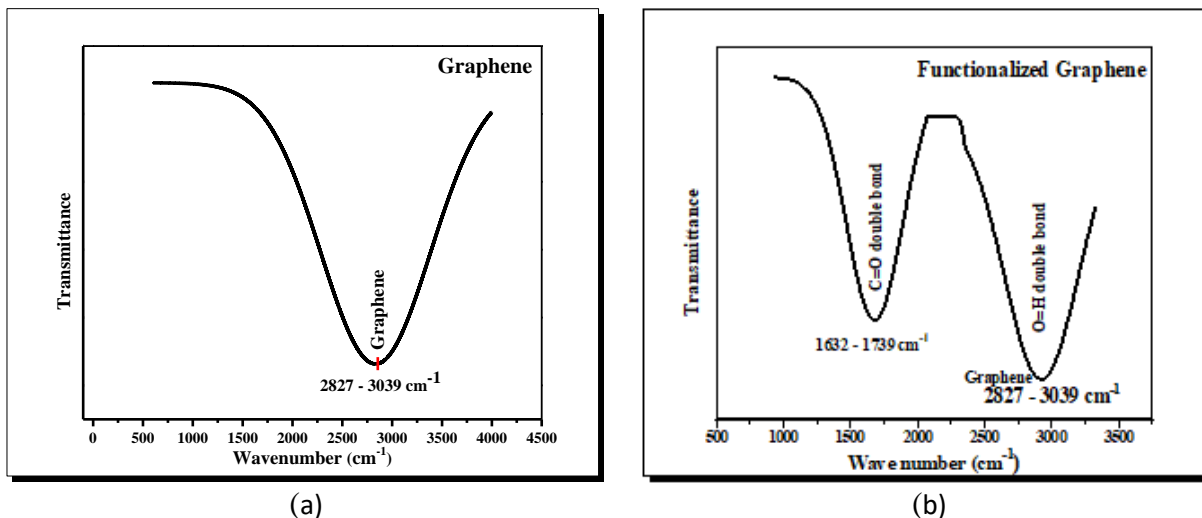
Figure 5.1: FTIR spectroscopy of (a) graphene and (b) carboxyl functionalized graphene.

The FTIR spectroscopy of graphene and carboxyl functionalized graphene results are shown in Figure 5.1. For pure graphene, a strong adsorption band is observed between the wavenumber of 2827-3039 cm^{-1} as shown in figure 5.1 (a). The band obtained from the functionalized graphene is strong adsorption band between the wavenumber of 1560-1800 cm^{-1} relating to O–C stretching vibration and another adsorption band between the wavenumber of 3567-3735 cm^{-1} due to the presence of O–H bond. O–H stretching vibration shows up at 3680 cm^{-1} and bending vibration of double peak appears at 3777 cm^{-1}. The sharp band between 1632 and 1739 cm^{-1} is due to C– O double bond stretching vibration. O −H bond shows broad spectrum due to hydrogen bonding between 3000-3500 cm^{-1}. The successful carboxylation of the graphene is confirmed by FTIR analysis as shown in Figure 5.1 (b). The absorption bands at 1800 cm^{-1} is identified to C=O stretching of –COOH and C–O stretching of C–OH/C–O–C group. The FTIR spectrum demonstrated a wide band at 3420 cm^{-1}, associated to the vibration and deformation bands of OH and COOH. The absorption bands between 1632 and 1739 cm^{-1} are recognized as aromatic C=C and carboxyl groups, another absorption band at1378 cm^{-1} indicates C−O (1066 cm^{-1}) groups and C−OH (1378 cm^{-1}) (Ma et al. 2013).

5.3 SCANNING ELECTRON MICROSCOPY (SEM) ANALYSIS

Optimal thermophysical properties can only be achieved through uniform dispersion of the nanoparticles in the LLDPE matrix. The particle distribution depends on the quantity of nanoparticles added, and surface area associated with it. The SEM images reveal that the microstructures are identical even after addition of nanoparticles which indicates the proper binding of particles. The binding is excellent due to intermolecular forces of π–π electronic bonds between the nanoparticles and the LLDPE matrix. At lower percentage loading, the π–π interaction is very good but as the loading percentage increases, it gets weaken due to segregation of nanoparticles. Conventional melting methods cannot avoid the re-stacking and accumulation of f-Gr because of the strong π–π interaction and van der Waals interface between f-Gr flakes which causes re-stacking. This significantly lowers the specific surface

area of f-Gr and delay the load transfers from the matrix to the fillers nanoparticles and leads to a substantial drop in the mechanical properties (Wei and Bai 2015).

Surface morphology of graphene, f-Gr, LLDPE, CPCM-1, CPCM-2, and CPCM-3 are shown in figure 5.2 a–f respectively. The mass fraction of f-Gr to LLDPE in CPCM-1, CPCM-2 and CPCM-3 are 1, 3, and 5 wt% respectively. The SEM analysis is carried out for different magnifications, only 1μ for nano additives and 1 and 5μ for CPCMs shown. Pure graphene SEM images indicate the packed flake-like structures where many layers are strongly bounded due to intermolecular forces SEM images of pure graphene can be seen in figure 5.2 (a). The SEM images of functionalized graphene can be visualized from figure 5.2 (b). Modification with functionalized carboxylic group breaks the layers and forms flake-like structures and its results bundles of broken structures of packed flakes.
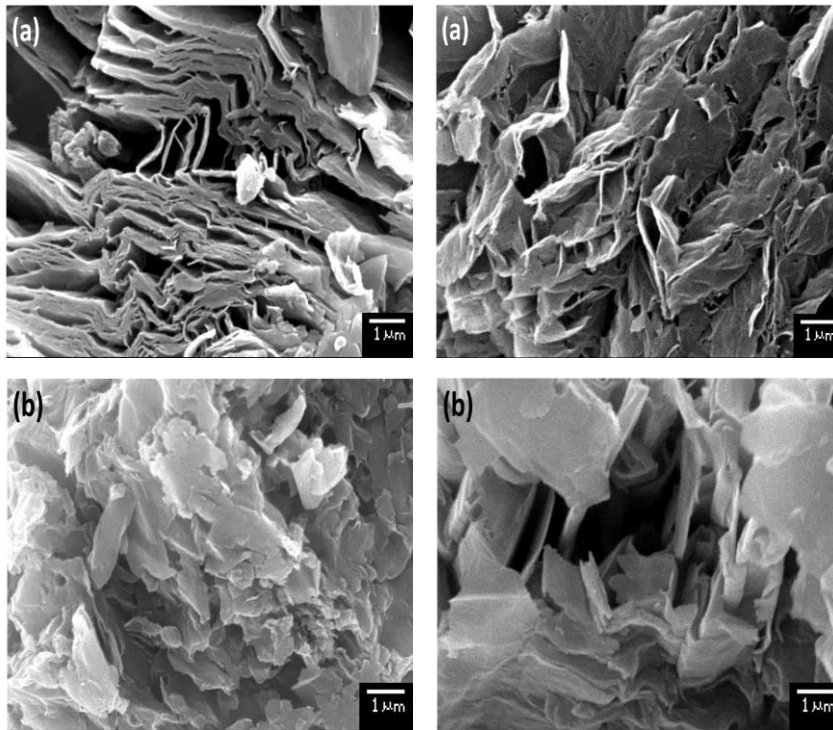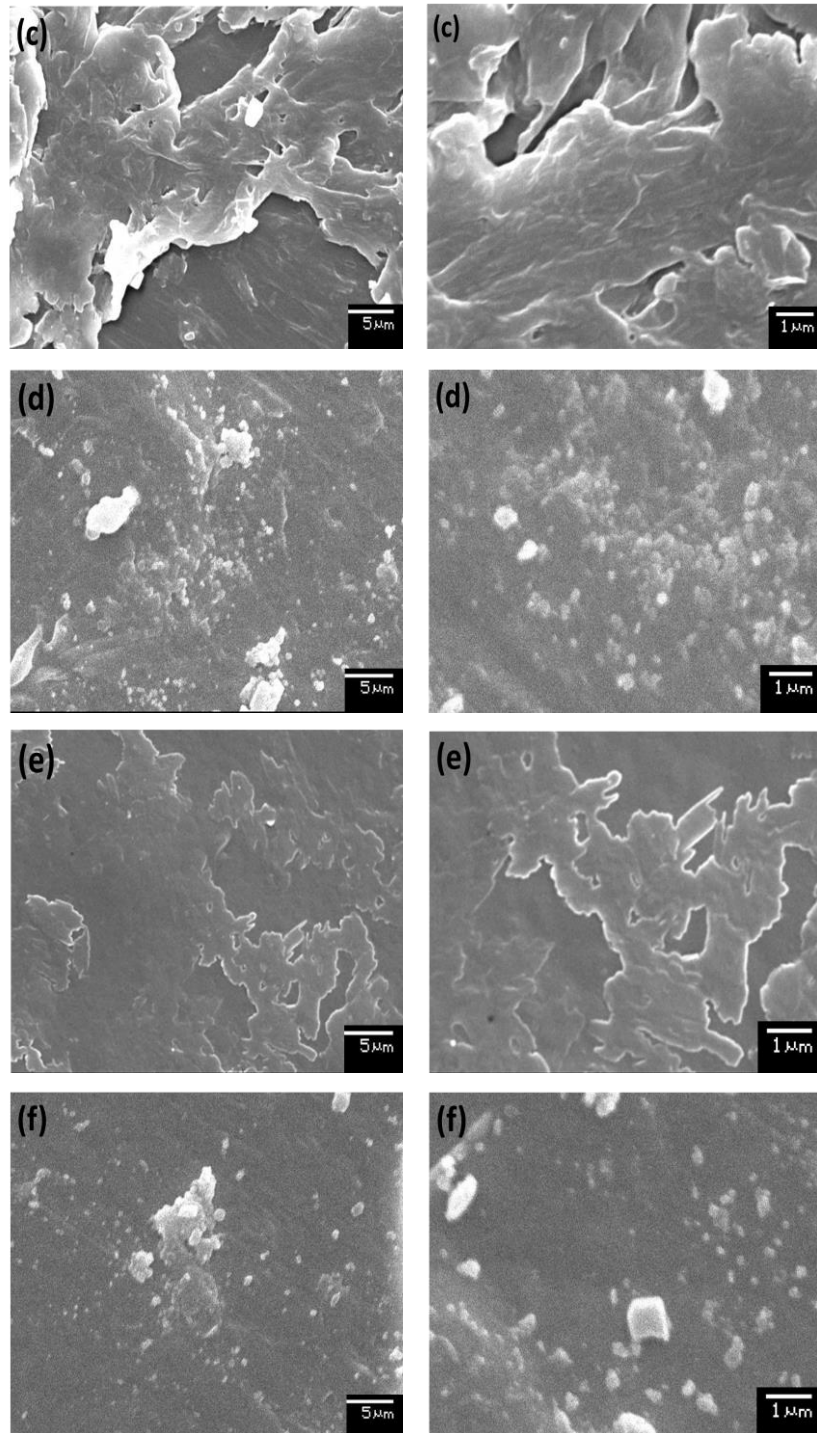
Figure 5.2: SEM images of (a) Pure graphene, (b) Functionalized graphene, (c) Base material (LLDPE), (d) CPCM-1 (1 wt%), (e) CPCM-2 (3 wt%) and (f) CPCM-3 (5 wt%).

The breaking of packed flakes helps in uniform distribution of nanoparticles in the composite material. The f-Gr is homogenously covered by the network structure of the LLDPE, which avoids the leakage. The structures in figure 5.2 (c) shows the fractures on the surface of the material, and the result of the reflection of light on the fractured surface. The surfaces are plain and smooth with uneven marks and small perturbations. Figure 5.2 (d) shows the accumulation of f-Gr, and CPCMs indefinite interface jointly shows proper distribution and strong interfacial adhesion between f-Gr and base material (Yang et al. 2018b). As f-Gr have much high thermal conductivity compared to the base material, which enhances the thermal conductivity and reduces the specific heat of the CPCMs. This is advantageous for the thermal storage applications the present analysis shows there is an improvement in thermal performance with better thermal stability.

The LLDPE completely bounds lower concentrations of f-Gr nanoparticles with significant adhesion in the interface of two components. Figure 5.2 (e) shows no perturbations, good interface and good coupling between f-Gr – LLDPE, and mainly this adhesion is due to the surface characteristics of nanoparticles (Tang et al. 2016b) and (Moreno and Saron 2017). Some cluster structures are also observed in CPCM-3, as shown in figure 5.2 (f), as it conveys the non-uniform distribution of the f-Gr filler. Some filaments are vertical to the screen, which represents white dots in the SEM images. Filaments with different alignments also form an uneven fibrous structure. Compatibility attributes the f-Gr and LLDPE composites to provide uniform dispersion, mixing and influence the structure with reduced thermal contact resistance (Guo et al. 2018).

5.4 DIFFERENTIAL SCANNING CALORIMETER (DSC) ANALYSIS

DSC curves in the heating and cooling methodology are illustrated in figure 5.3, which shows the effect of nanoparticle addition with temperature on the heat of fusion. A peak point is seen during every charging process between the temperature range of 118–125°C, due to the melting of the CPCMs. The onset heating and cooling temperature of each sample is reduced compared to pure LLDPE, due to the abridged interaction of LLDPE molecules and nano additives broad absorbing curve is seen for CPCM-1. The higher peak

denotes solid–liquid phase change process, and it is used to estimate the latent heat value in the cooling process. As f-Gr mass fraction reduces, the heating/cooling temperature and latent heat capacity of CPCMs reduces consequently. Mixing of nanoparticles modifies the crystallization ability of the composites, and the crystallite size become smaller during crystal growth by acting as an impurity. This changes the heat of fusion and it may increase or decrease (Maxwell's mixture model), however, in the present work it increases.

The thermal conductivity of the pure LLDPE are 0.32 and 0.33 W/mK in solid and liquid phases respectively, which is ranging from 0.392 – 0.886 W/mK in the solid phase and 0.351 – 0.687 W/mK in the liquid phase for CPCM-1, CPCM-2 and CPCM-3 respectively. The f-Gr nanoparticles can expressively enhance the thermal conductivity of the CPCMs with the increase in percentage loading (Lin et al. 2018). The specific heat values are obtained from three repetitive DSC experiments and the average values are recorded for different CPCMs.
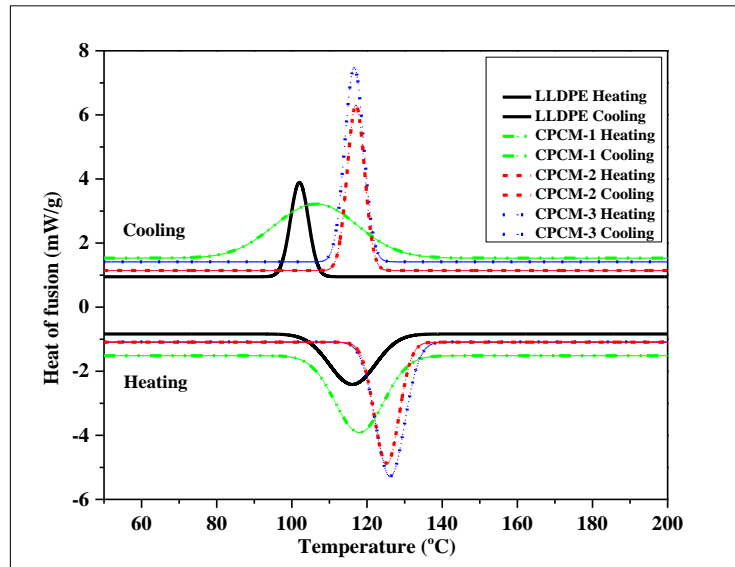
Figure 5.3: Effect of nanoparticle addition on the heat of fusion with temperature.

Figure 5.4 shows the effect of nanoparticle addition with temperature on specific heat capacity. The weight of all samples is between 3.5 to 8 mg. The heating and cooling DSC curves of pure LLDPE and CPCMs are portrayed. The crystallization temperature (T_c) also

decreases from 117.80, 116.68, 115.08 and 101.35°C for CPCM-1, CPCM-2, CPCM-3 and LLDPE respectively.
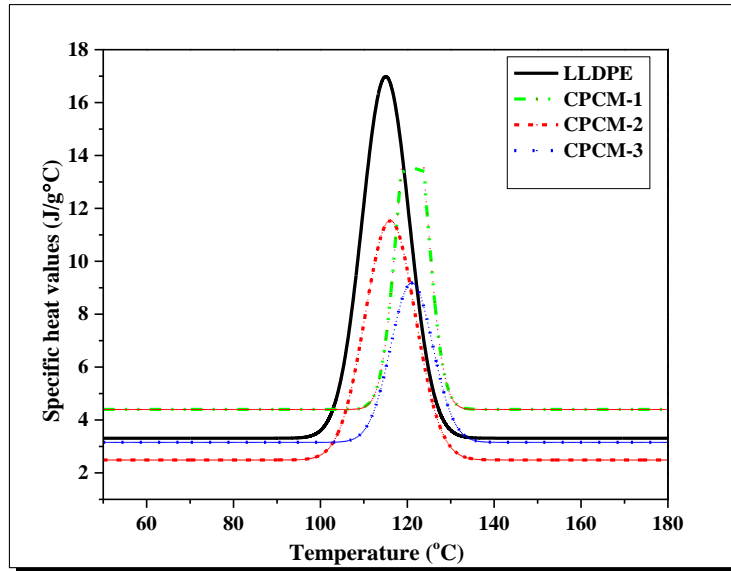
Figure 5.4: Effect of nanoparticle addition on specific heat capacity with temperature.

The crystallization temperature of CPCMs may increase or decrease with percentage loading of nanoparticles depends on the processing conditions (Cruz-Aguilar et al. 2018). The specific heat of the CPCM reduces with increase in nanoparticle concentration. During melting and solidification, specific heat values are proportional to the mass fraction of the nanoparticles in the CPCMs, and the relationship can be written as

$$\Delta H_c = \eta \Delta H_o \tag{4.1}$$

where ΔH_C and ΔH_0 are the melting / solidification specific heat of CPCMs and pure LLDPE respectively. The term η represents the nanoparticles mass fraction. The specific heat of CPCM-1, CPCM-2 and CPCM-3 reduces with nanoparticle concentration.

The nanoparticle concentration can be limited to optimum concentration (3 wt% in the present case) to maintain high specific heat. The thermal energy storage system should completely change the material phase to achieve better thermal storage and release capabilities. The melting temperature of the CPCM is to obtain the maximum thermal

storability and enhanced performance of TES system. The melting and solidification properties of CPCMs are determined by using DSC analysis.

DSC analysis is carried out to determine the specific heat of the material, three times and found the solidification temperatures are 83.25, 98.51, 112.55, 112.92˚C for LLDPE, CPCM-1, CPCM-2, CPCM-3 respectively. The latent heat absorbed and rejected during heating and cooling cycle data are listed in Table 5.1.

Table 5.1: Latent heat absorbed and rejected during the heating and cooling cycle.

Materials	Heating			Cooling		
	Onset temperature (̊C)	End temperature (̊C)	Enthalpy (kJ /kg)	Onset temperature (̊C)	End temperature (̊C)	Enthalpy (kJ/ kg)
LLDPE	105.45	124.12	76.82	105.77	98.51	71.95
CPCM-1	109.31	126.03	82.90	123.28	112.55	73.03
CPCM-2	117.03	129.34	95.75	126.27	113.25	91.75
CPCM-3	119.68	131.66	96.84	120.38	114.92	94.04

The phase change temperature is determined from onset points of the heating curve peaks of DSC thermograms. The lower temperature with lesser intensity indicates the solid-liquid phase conversion process. The heating curve peaks indicate the solid-liquid phase conversion, which contributes towards the thermal storage capacity. The latent heats of fusion of composites gradually increase with nanoparticles concentration.

5.5 THERMAL CONDUCTIVITY CALCULATION

Thermal conductivity of composite phase change materials is calculated using the expression given in equation (4.2). There are different methods to measure the thermal

conductivity, which depends on the suitability of material properties and the medium temperature.

Thermal diffusivity is a combination of thermal and physical properties (such as thermal conductivity, density, and specific heat) with respect to temperature. It is defined as the ratio of the thermal conductivity to the specific heat capacity of the material (Yánez et al. 2013).

$$\alpha = \frac{k}{\rho \times Cp} \tag{4.2}$$

where α, ρ, k and C_p are thermal diffusivity, density, thermal conductivity and specific heat respectively. The values of density, diffusivity, and specific heat are measured experimentally and substituted in the diffusion equation to calculate the thermal conductivity as shown in equation (4.2).

5.6 THERMOPHYSICAL PROPERTIES VARIATION OF CPCM

The thermophysical properties show a good response to the f-Gr nanoparticle addition for thermal conductivity and heat of fusion. The details of the thermophysical property variation for different materials can be visualized from Table 5.2.

Table 5.2: Thermophysical properties of different materials.

Sl. No.	Thermophysical properties		LLDPE	CPCM-1	CPCM-2	CPCM-3
	Percentage loading (%)		*0% f-Gr*	*1% f-Gr*	*3% f-Gr*	*5% f-Gr*
1	Density ρ (kg/m^3)		928.00	928.02	928.05	929.00
2	Specific heat C_p (J/kg K)	Solid	5380	3700	3680	3400
		Liquid	3240	2800	2600	2390
3	Thermal conductivity k (W/mK)	Solid	0.33	0.392	0.876	0.886
		Liquid	0.32	0.351	0.620	0.687
4	Heat of fusion (kJ/kg)		71.75	91.75	92.90	97.00

The heat of fusion changes considerably from 71.75 – 97 kJ/kg for the minimum to maximum percentage loading as shown in figure 5.5 (a). The characterization study shows enhancement in thermal conductivity of CPCMs from 0.32 to 0.886 W/mK for the base material to CPCM-3 respectively. The specific heat capacity is decreased from 10 to 30% for liquid and solid phases.

(a)

(b)

(c)
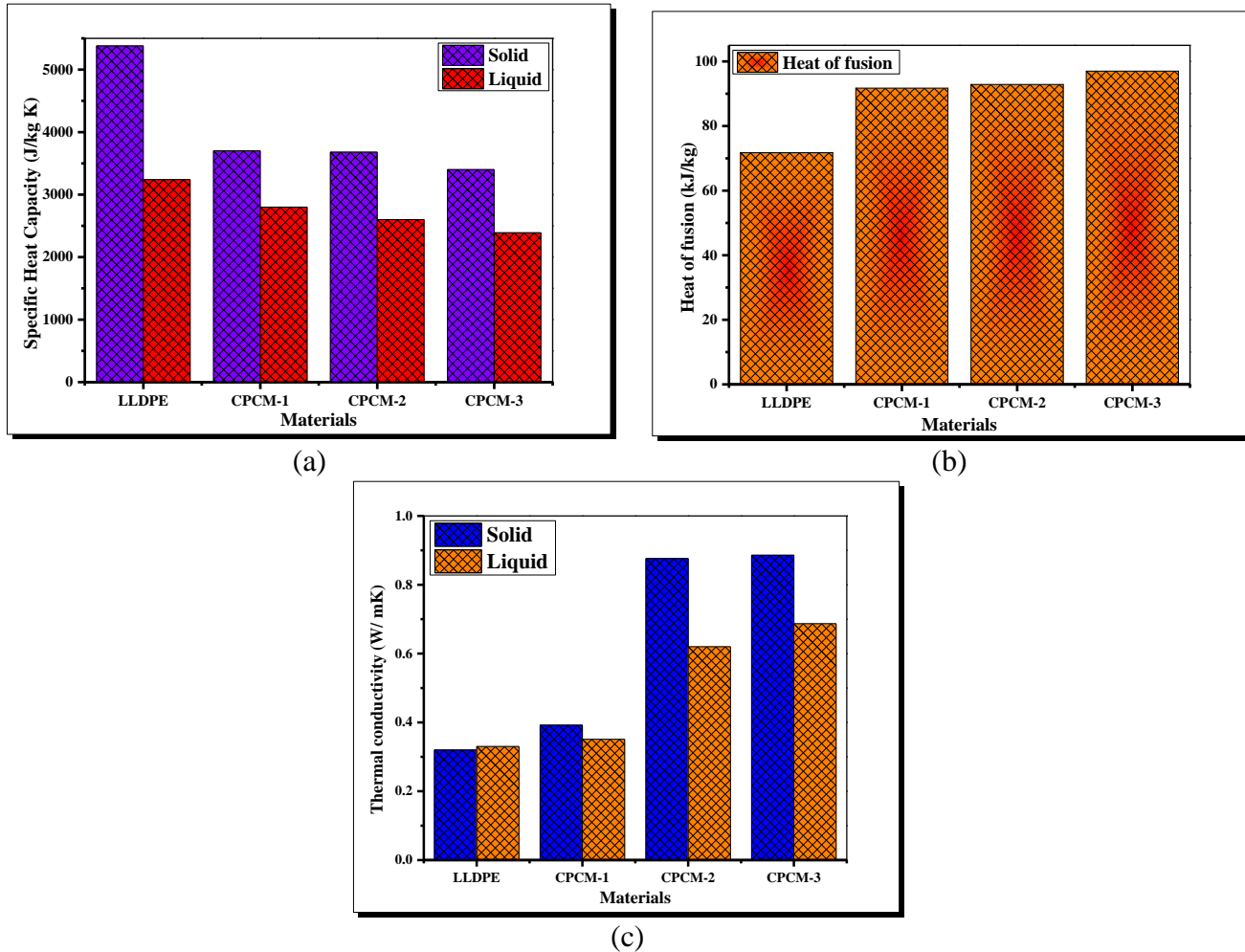
Figure 5.5: Variation of thermophysical properties (a) heat of fusion, (b) specific heat, and (c) thermal conductivity with nanoparticles concentration.

The specific heat variation with percentage blending of f-Gr nanoparticles in LLDPE and thermal conductivity variation are shown in figure 5.5 (b) and (c). The percentage loading of f-Gr improves the thermal conductivity, but it has an adverse effect on specific heat. The

suitable thermal energy storage material should possess high thermal conductivity and specific heat capacity.

5.7 THERMAL STORAGE ANALYSIS USING 2-D NUMERICAL STUDY

5.7.1 Model Description

In this section, the thermal storage model is the bounded square domain to analyze the thermophysical property enhancement. The thermal storage medium used for the present study is composite phase change materials with enhanced thermophysical properties. The boundary conditions applied are (i) Constant heat supply applied to the left wall and (ii) Insulation to the other three walls. Figure 5.6 shows the geometrical and computational model of the square domain.
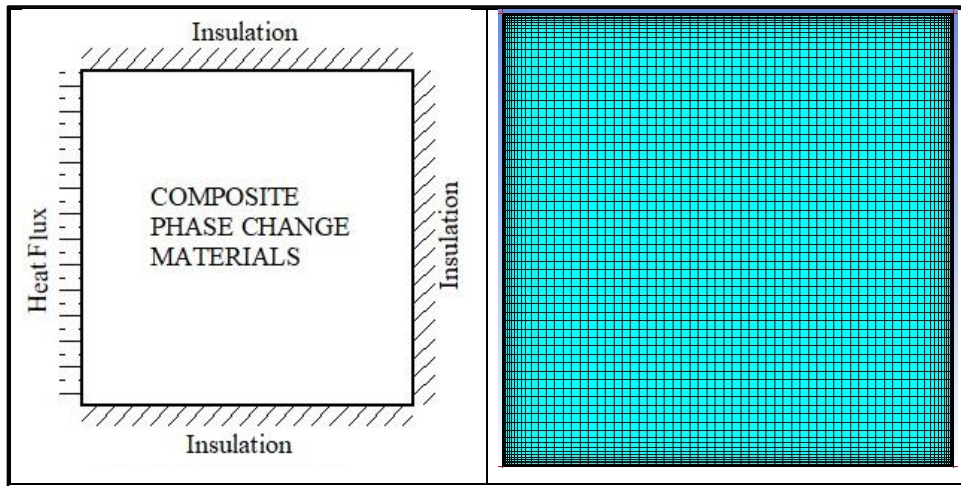
(a) Geometrical model   (b) Computational model

Figure 5.6: Representation of (a) geometrical model and (b) computational model of the square domain.

5.7.2 Grid Independence Study

A detailed grid dependence study is carried out for selecting the optimum grid size, and it is observed that the grid size of 130×130 shows least deviation (0.0029) on maximum temperature compared to other three grid (100×100, 150×150, 160×160) sizes. The grid

size of 130 × 130 is considered as optimal grid, and the same is used for numerical computations. The computational procedure is same as mentioned in chapter 3.

5.7.3 Thermal energy storage capacity analysis of CPCMs

Numerical analysis is carried out for complete melting of the materials, and the time taken for complete phase change is 2700, 2500, 2400, and 2300 sec for LLDPE, CPCM-1, CPCM-2, and CPCM-3 respectively. The composite materials which filled into the square domain are heated by applying constant heat supply of 800 W. The CPCM absorbs the heat and changes its phase from left to right wall and the mass fraction variation as shown in figure 5.7. The time intervals selected are 500, 1000, 2000, and 2500 sec to understand the complete melting process. It is observed that the melt front motion of the solid-liquid interface depends on the nanoparticle concentration and hot wall of the domain.
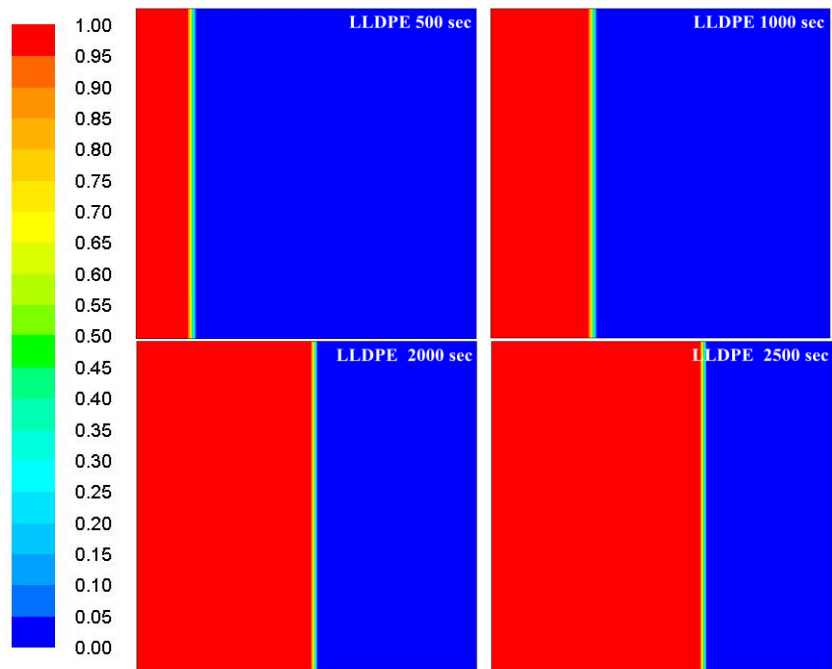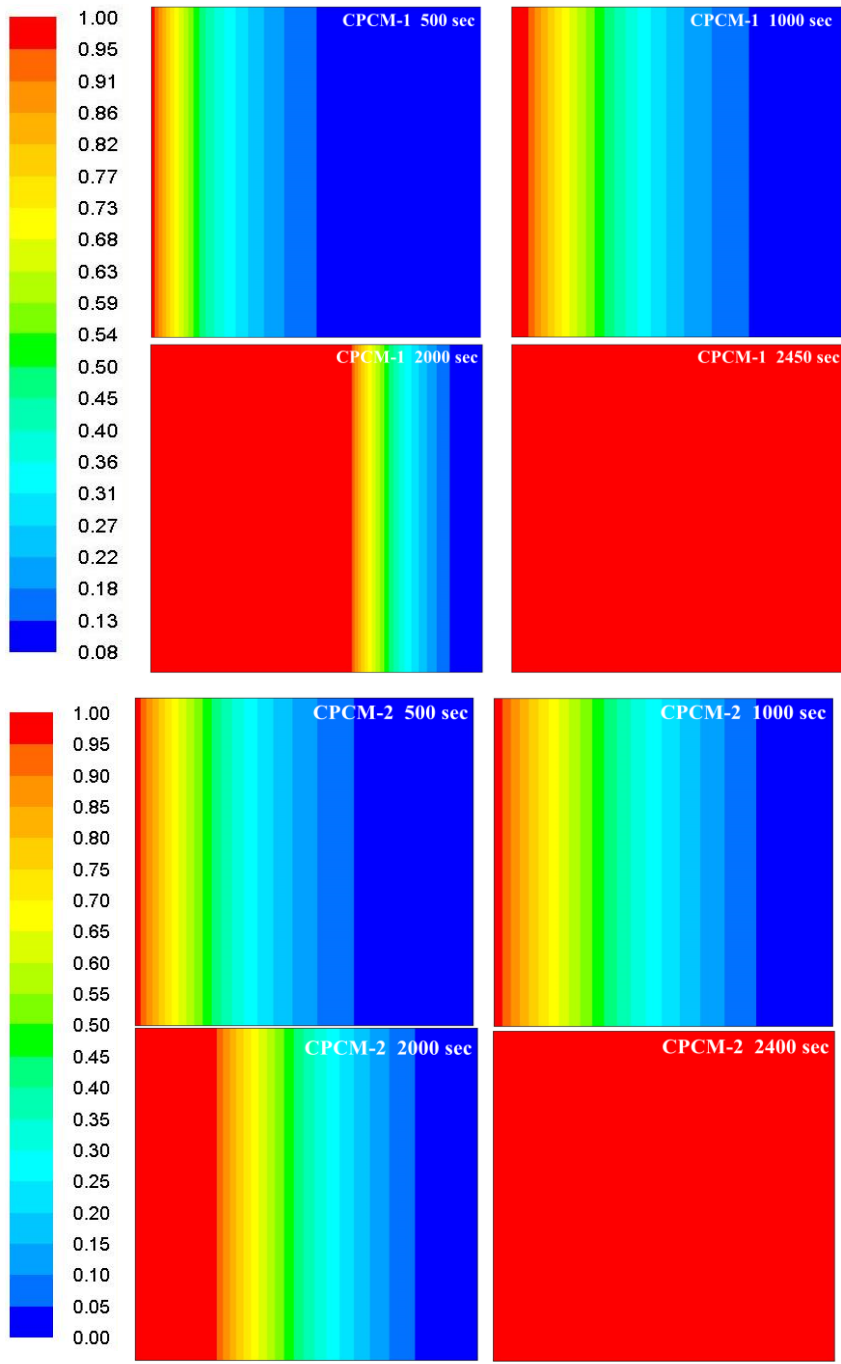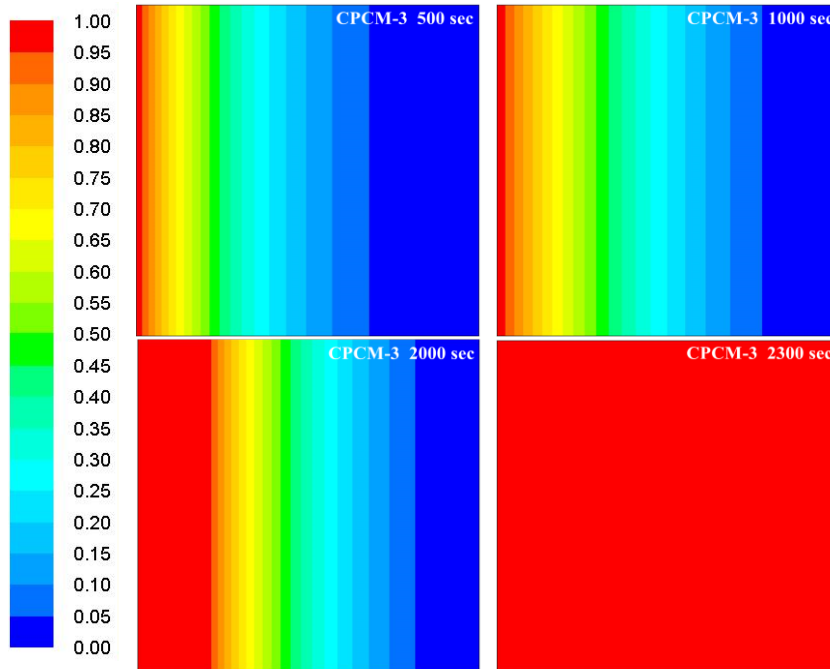
Figure 5.7: Variation of mass fraction during the melting process of LLDPE, CPCM-1, CPCM-2, and CPCM-3.

As concentration increases the melting front moves with faster rate, the nanoparticle concentration increases the thermal conductivity of the CPCMs and results in faster melting rate. In the melting process, a large amount of heat is absorbed and stored in the form of latent heat, and it can be accelerated by mixing the nanoparticles in the base material. The blending of nanoparticles also reduces the degree of supercooling due to heterogeneous nucleation.

Figure 5.8 shows the complete details of heat absorbed and heat loss during the phase change process. During the heating cycle, pure LLDPE, CPCM-1, CPCM-2, CPCM-3 are absorbed 76.82, 95.75, 72.90, 96.84 kJ/ kg of heat, and changes its phase to the liquid state. The maximum loss of heat is observed in CPCM-1 with 8.52% during the phase change process, and minimum loss of 2.5% of heat is observed for CPCM-3.
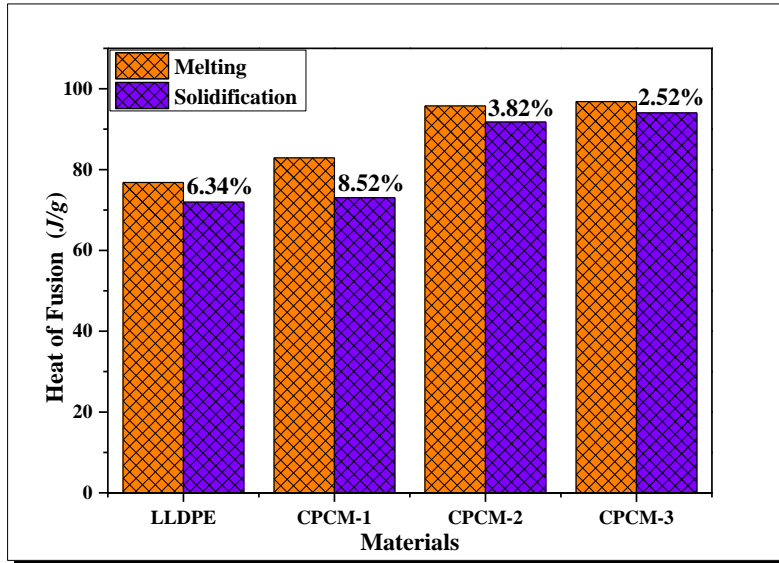
Figure 5.8: Absorption and rejection of heat during the heating and cooling process.

5.7.4 Average Mass Fraction Analysis

In this section, average mass fraction analysis is carried out through numerically. Figure 5.9 shows the mass fraction variation with nanoparticle concentration. Heat is supplied to all materials initially, 500 sec of heat supply CPCM-1 shows faster melting rate (0.38) and other materials are slow with mass fraction values of 0.3, 0.34 and 0.34 for LLDPE, CPCM-2, CPCM-3 respectively. As time proceeds the nanoparticles moves and enhances the thermal conductivity of material due to faster heat transfer rate and CPCM-3 takes over the other materials with maximum mass fraction value of 0.68. The LLDPE, CPCM-1, and CPCM-2 materials show slower melting with mass fraction values of 0.42, 0.62 and 0.64 respectively. At 2000 sec, mass fraction of LLDPE, CPCM-1, CPCM-2, CPCM-3 increases 19, 28.73, 24.70 and 20.93%.
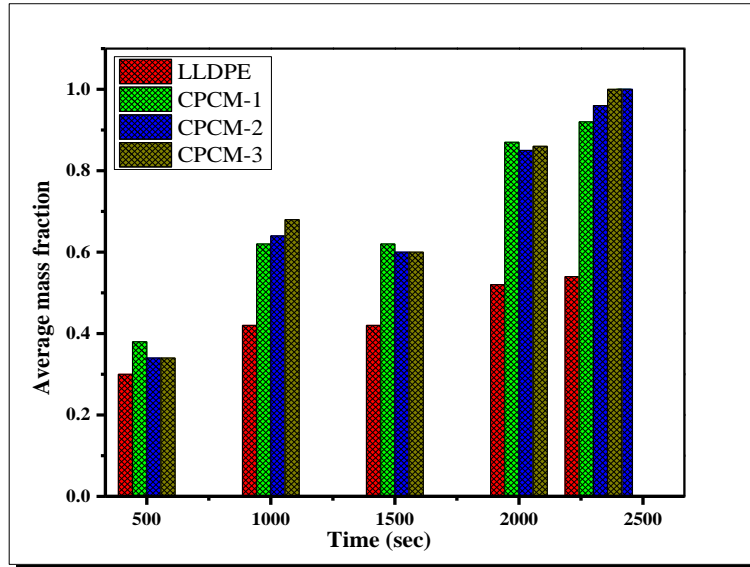
Figure 5.9: Variation of the mass fraction with nanoparticle concentration.

All the materials show complete melting at different time intervals, but LLDPE shows 60% of melting when heated up to 3000 sec. After 2000 sec, LLDPE shown 500 sec for melting, CPCM-1 completes melting in 450 sec. CPCM-2 completes 400 sec, and CPCM-3 completed melting at 300 sec, which is the fastest among all materials, 5% addition of nanoparticles reduces the melting time by 42%. Selecting the optimum concentration will provide feasible results for better storability and to increase the material performance. The 3 wt% of nanoparticles concentration is optimal, and it can be preferred for commercial applications.

5.7.5 Temperature Distribution Study

The minimum and maximum temperature ranges are obtained during the melting process are tabulated in Table 5.3. The minimum and maximum temperature limits are reached by LLDPE during the complete melting process from 398.82 to 582.51 (31.51%) and 395.01 to 574.31 (31.18%) respectively.

Table 5.3: Minimum and maximum temperature variation during melting process.

Time (sec)	Materials	LLDPE	CPCM-1	CPCM-2	CPCM-3
500	T_{max} [K]	398.82	396.08	395.53	395.52
	T_{min} [K]	395.01	395.01	395.01	395.01
1000	T_{max} [K]	401.12	397.17	396.19	396.15
	T_{min} [K]	395.15	395.17	395.39	395.43
1500	T_{max} [K]	403.44	398.41	396.72	396.67
	T_{min} [K]	396.72	395.51	395.91	395.95
2000	T_{max} [K]	415.52	400.12	397.36	397.29
	T_{min} [K]	406.43	396.12	396.44	396.47
2500	T_{max} [K]	582.51	541.93	439.93	405.8
	T_{min} [K]	574.31	539.32	439.12	405.07
% Increase	T_{max}	31.51	26.91	10.09	2.53
	T_{min}	31.18	26.76	10.05	2.48

From the table, as the nanoparticle concentration blending increases the maximum temperature range decreases to 26, 10, and 2.5% for CPCM-1, CPCM-2, and CPCM-3 respectively. The minimum temperature range is the same with negligible variations compared to the maximum temperature range. The reduction in temperature range indicates effective latent heat storage mechanism where the temperature variation is minimal. To retain the thermal energy storage stored in the material the surface temperature should be constant. The increase in surface temperature loses the stored energy through sensible heat. The increase in temperature causes the intense particle motion in the CPCMs, and the molecular forces get reduced.

5.8 THERMAL ENERGY STORAGE ANALYSIS THROUGH ANALYTICAL CALCULATIONS

To compare the thermal characteristics, analytical calculation is also carried out, and the results are compared and analyzed for numerical and analytical calculations. Analytical calculations are made by the data obtained through characterization study.

Amount of heat required for complete melting is calculated using the following correlation.

Amount of thermal energy stored = (Amount of heat supplied to raise the material temperature from $30°C$ (room temperature) to its melting point) + (Amount of heat supplied during complete phase change) + (Heat required to increase the emperature from melting temperature to maximum temperature).

$$Q = mCp(T_{melt} - T_{room}) + mH_{fus} + mCp(T_{max} - T_{melt}) \tag{4.3}$$

Where Q is the total amount of heat stored, m is mass, C_p is Specific heat, H_{fus} is Latent heat of fusion of the CPCM. T_{melt}, T_{room} and T_{max} are melting temperature of CPCM, room temperature and maximum temperature reached during melting process respectively.

Figure 5.10 shows the comparison of heat-storing capacity by analytical calculation and simulation results. The difference between the analytical calculation and simulation results are ranging from 11–25%. The analytical calculation results show low thermal storage capacity compared to simulation results due to the consideration of physical effects.
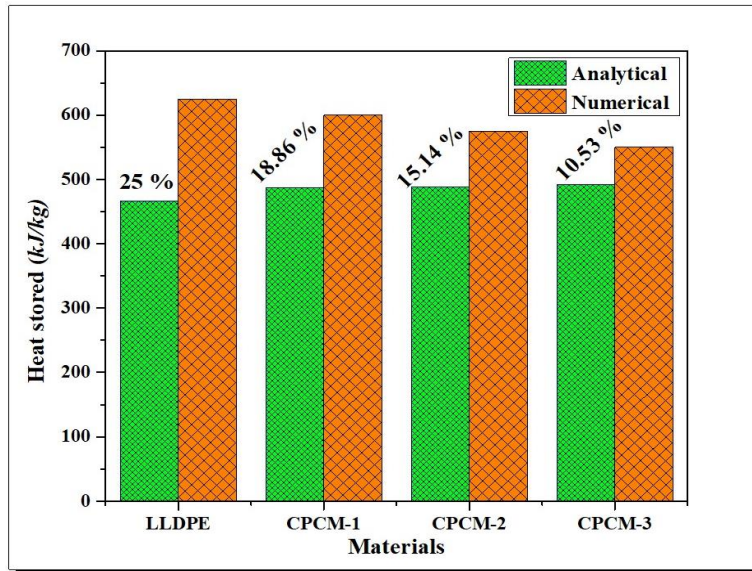
Figure 5.10: Comparison of heat-storing capacity by analytical calculation and simulation.

5.9 CLOSURE

To make use of waste plastics as recycled composites for thermal energy storage material CPCMs are prepared. Plastic based composites are studied with different concentrations of nano additives such as 1, 3, 5% and it referred to as CPCM-1, CPCM-2, and CPCM-3 respectively. The characterization of CPCMs are also carried out to analyze the relationship between the base material, and the nano additive concentration on thermophysical properties and thermal energy storage capacity evaluation is discussed in detail.

CHAPTER 6

NUMERICAL AND EXPERIMENTAL ANALYSIS OF COMPOSITE PHASE CHANGE MATERIALS

6.1 INTRODUCTION

Numerical and experimental analysis is carried out for thermal performance and thermal energy storage capacity evaluation of CPCMs. The numerical study consists of a 3-D model of thermal energy storage unit filled with CPCM, and suitable boundary conditions are imposed. The experimental setup is also fabricated for the same dimensions to make heat flow thermal storage unit, and it is insulated. Present work also focuses on enhancing the heat energy storage capability of polyethylene-based composite materials, both experimental and numerical approaches are chosen for the analysis.

6.2 THERMAL ENERGY STORAGE ANALYSIS THROUGH NUMERICAL STUDY

Thermal energy storage model considered is a square prism domain of 150 mm × 50 mm × 150 mm (x, y, z) dimensions. Composite phase change material is used as thermal storage material in the numerical study. The constant heat supply is applied to the base wall of the domain, and other walls are insulated.

6.2.1 Problem Description

To obtain the results, assumptions are made for study. (i) The molten TSM acts as Newtonian fluid, and the flow is incompressible, (ii) The phase conversion takes place in laminar form with least viscous dissipation rate, (iii) The thermophysical properties of TSM are temperature dependent, (iv) Conduction and convection heat transfer rates are controlled, (v) Volume remains same during phase conversion and (vi) the TSM always

remains in contact with the boundary walls of the domain. The representation of the geometrical and computational domain as shown in figure 6.1.

(a) Geometrical model   (b) Computational model
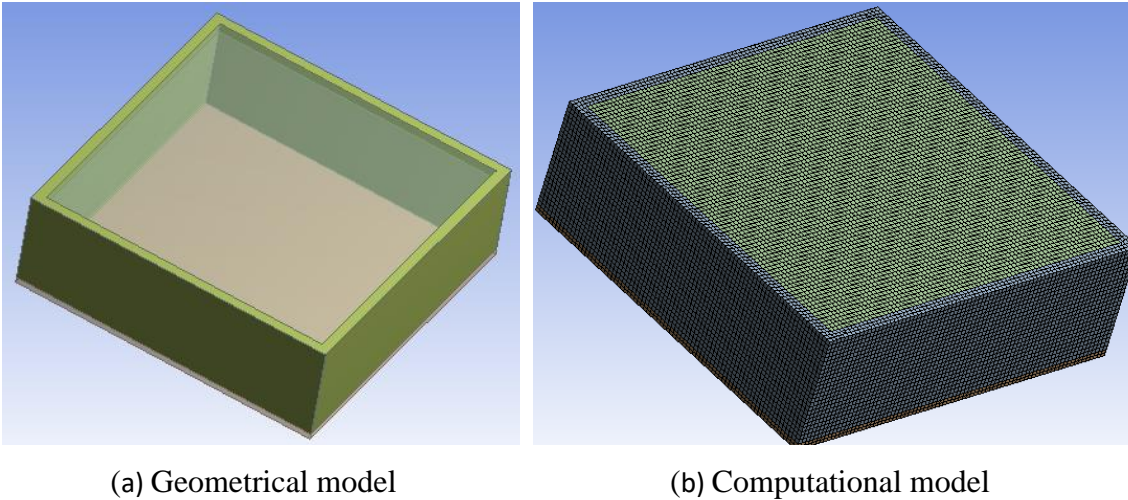
Figure 6.1: Representation of the (a) geometrical and (b) computational domain.

6.2.2 Boundary Conditions

The numerical study is carried out by imposing the constant heat supply boundary condition at the base wall, and other walls are insulated. Heat is supplied through the ceramic based electric heater. A constant rate of heat coming out of heater is absorbed by the composite phase change materials and store it in the form of latent heat. Number of thermocouples are inserted at different parts of the domain to ensure the temperature distribution and confirm the completion of the melting process. Once all the temperature attains the same temperature it is to be assumed that the thermal storage material is completely melted. All four materials are observed and investigated for thermophysical property variation, and thermal energy storage capacity during melting and solidification processes.

6.2.3 Grid Independence Study

A detailed grid independence study is carried out to find the optimum grid size for the computational investigation. Table 6.1 shows the comparison of maximum temperature at

1500 sec of computational time. The least percentage deviation value is chosen to be the optimum element size, and it is selected for the numerical calculations.

Table 6.1: Comparison of maximum temperature at 1500 sec for different grid sizes of the domain.

Element size (mm)	Number of grid cells	Maximum Temperature after 1500 sec	% Deviation
0.004	17797	1205.00	47.50
0.003	36864	644.24	01.83
0.0025	38416	682.24	07.30
0.002	69620	644.24	01.83
0.01	140625	632.39	Base

The two-dimensional numerical analysis of CPCMs is extended to three-dimensional analysis. Different components are appropriately modeled and defined all the required parameters, which are significantly affecting the thermal storage capacity of the composite phase change materials. The 3-D computational procedure is also the same as 2-D analysis as discussed in Chapter 3.

6.3 THERMAL ENERGY STORAGE ANALYSIS THROUGH EXPERIMENTAL STUDY

To validate the numerical results an experimental study of thermal energy storage analysis is also carried out. The experimental setup consists of a voltage regulator, thermal storage unit (TSU) filled with CPCM, thermocouples, data acquisition system (DAQ), computer unit. The melting temperature of the CPCMs used in this experiment is in range of 120-125º C. The CPCM is filled in a stainless-steel unit which can withstand high temperature.

6.3.1 Experimental Setup used for Thermal Energy Storage Evaluation

Figures 6.2 (a) and (b) shows the schematic of the complete experimental setup of the block diagram and actual representation of components. The TSU is coupled with measuring and

controlling devices which are voltage regulator, electric heater, data acquisition system, and finally a computer unit to process the obtained data.
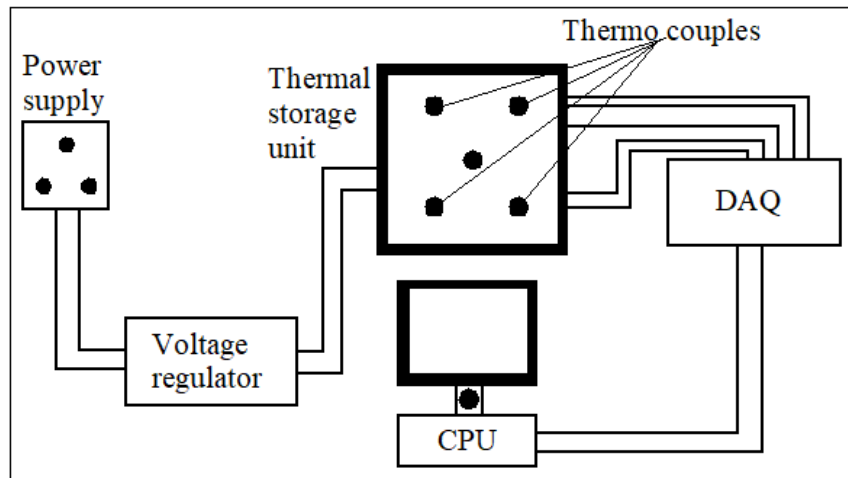
(a) Schematic representation of complete experimental setup.
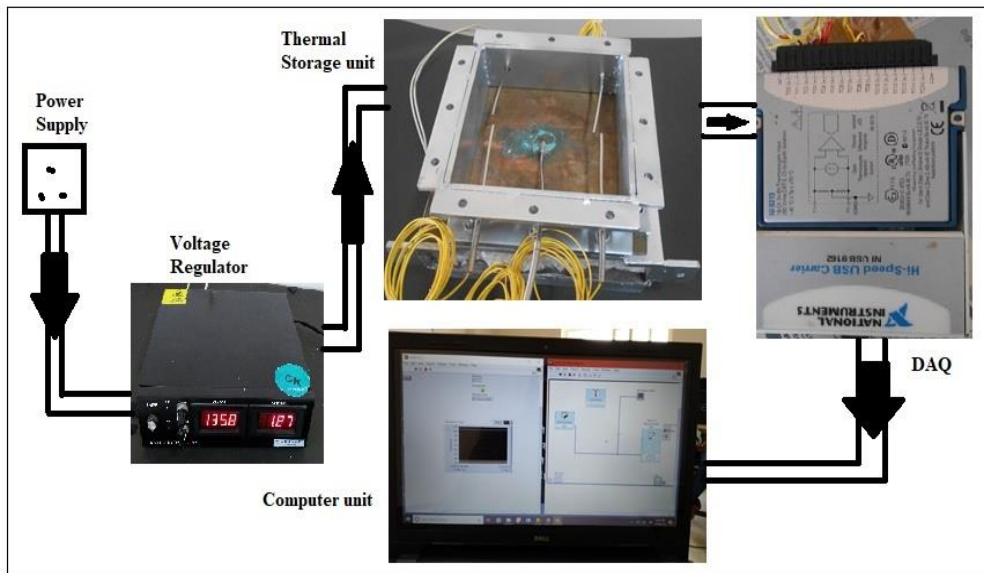
(b) Actual representation of experimental setup.

Figure 6.2: Experimental setup of (a) block diagram (b) actual representation.

6.4 HEAT SUPPLY CALCULATIONS DURING MELTING PROCESS

Constant rate of heat (250 W) is supplied by controlling the voltage because the voltage is a variable parameter to regulate the heat supply.

$$Q_{supply} = V \times I \tag{6.1}$$

The total amount of heat supplied is for different time intervals for different materials till it attains the complete molten state. Here V and I are voltage and current in volts and amps respectively as seen in equation (5.2). Throughout the experimental operation, temperature variations are recorded under constant heat supply condition. Experimental, numerical, and analytical comparison of heat supplied and time requirement for melting by different materials are listed Table 6.2.

Table 6.2: Experimental, numerical and analytical comparison of heat supplied and time consumed for melting by different materials.

Materials	Heat Supplied for Melting (kJ)			Time taken for Melting (sec)	
	Experimental	Numerical	Analytical	Experimental	Numerical
LLDPE	1800	1460	1144.40	3600	2400
CPCM-1	1925	1570	1268.52	3850	2600
CPCM-2	2050	1650	1443.14	4100	3150
CPCM-3	2025	1610	1302.90	4050	2800

The amount of heat supplied for complete melting of CPCM is higher for experimental results, compared to numerical and analytical results. The experimental setup contains the different components which absorb some amount of energy before transferring to the thermal energy storage domain. In numerical study, boundary conditions are applied impeccably to the system which transfers heat energy without any leakage. Analytical calculations show low values due to assumptions made for solving the equations. Time requirement during the experiment for complete melting is high compared to the numerical analysis due to non-achieving of perfect insulation, and it causes a discrepancy between the two results. The amount of heat absorbed during the experiment is 1800, 1925, 2050 and 2025 kJ and time taken is 3600, 3850, 4100, 4050 sec by LLDPE, CPCM-1, CPCM-2, and CPCM-3 respectively. In numerical analysis, the amount of heat absorbed is 1460, 1570, 1650, and 1610 kJ and time taken for complete melting is 2400, 2600, 3150, 2800 sec respectively.

6.5 HEAT REJECTION ANALYSIS DURING SOLIDIFICATION PROCESS

The heat rejection is taking place by combined mode of heat transfer viz convection and radiation.

$$Q_{Total} = Q_{convection} + Q_{radiation} \tag{6.2}$$

$$Q_T = (hA\Delta T) + (\sigma A\varepsilon(T_1^4 - T_2^4)) \tag{6.3}$$

Heat transfer through convection

$$Q_c = (hA\Delta T) \tag{6.4}$$

where h is the heat transfer coefficient determined by using Nusselt number correlation.

$$h = \frac{Nu \times k}{L} \tag{6.5}$$

Correlations for heated surface facing upwards given by Mc Adams (1954) and Lloyd & Moron (1974)

Nu= 0.54 x $Ra^{1/4}$ for $10^4 < Ra < 10^7$

Nu= 0.15 x $Ra^{1/3}$ for $10^7 < Ra < 10^{10}$

$$Ra = \frac{g\beta\Delta TL^3}{v^2} \times Pr \tag{6.6}$$

Where g, β,v, Pr are properties of air at a mean temperature T_m. A is area, h is heat transfer coefficient, Nu, Pr and Ra are is Nusselt number, Prandtl number and Rayleigh number. The mean temperature is given by

$$T_m = \frac{T_s - T_a}{2} \tag{6.7}$$

Heat transfer through radiation

$$Q_r = \sigma A \varepsilon (T_1^4 - T_2^4) \tag{6.8}$$

Where σ, A, and ε are Boltzmann constant area and emissivity respectively. T_1 and T_2 are surface and wall temperatures, emissivity is also calculated (Atalla et al. 1966).

The cooling or solidification occurs due to rejection of heat, which is the combined effect of convection and radiation. The gradual heat rejection during complete solidification process is estimated for experimental and numerical analysis. Table 6.3 shows the experimental and numerical comparison of heat rejection during solidification. Amount of heat rejection by convection and radiation is calculated for both approaches. Experimental study exhibits high values of rejection compared to numerical results. System efficiency is calculated with respect to the amount of heat supplied during melting, and the amount of heat rejected during the solidification process. The base material shows the least rejection and retains 20.53% heat by rejecting 1430.50 kJ of heat, and CPCM-2 shows maximum rejection and retains 12.90% heat by rejecting 1785.59 kJ of heat. The CPCM-1 and CPCM-3 shows a reduction of heat rejection and retains 19.95 and 16.68% by losing 1541.02 and 1687.25 kJ of heat. The experimental and numerical results are analyzed into two sections (i) heating and (ii) cooling cycle where the amount of heat energy stored and temperature variations are summarized.

Table 6.3: Experimental and numerical comparison of heat rejected during solidification.

Heat Rejection during Solidification (kJ)								
Materials	Experimental				Numerical			
	Q Convection	Q Radiation	Q Total	Heat Retention (%)	Q Convection	Q Radiation	Q Total	Heat Retention (%)
LLDPE	972.74	457.76	1430.50	20.53	827.82	306.18	1134	22.32
CPCM-1	983.10	557.92	1541.02	19.95	858.816	405.76	1264.57	19.45
CPCM-2	1273.43	512.16	1785.59	12.90	1160.548	263.72	1424.26	13.68
CPCM-3	1100.95	586.30	1687.25	16.68	942.058	436.4	1378.45	14.38

6.6 ENERGY ABSORPTION DURING MELTING PROCESS

Continuous heating is carried out upto 4000 sec to complete the melting process. The amount of heat absorbed and the rise in temperature is observed and discussed in the present section. Figure 6.3 shows the numerical and experimental calculation of energy absorbed during the melting process with charging for different materials. The heat energy supplied by the electric heater at a constant rate of 250 W through which the thermal storage material receives the heat energy, and starts energy level variation during the melting process. After 500 sec, the heat energy possessed by different materials is 471.13, 754.79, 766.02, and 780.21 kJ calculated for LLDPE, CPCM-1, CPCM-2, and CPCM-3 respectively. As time progresses the continuous supply of heat increases the thermal storage medium temperature until it reaches the phase change temperature. After reaching phase change temperature, TSM starts changing its phase, and melting begins. This happens without changing surface temperature due to the absorption of heat in latent heat form. At the completion of melting process, TSMreceives heat upto its saturation limit. Then surface temperature starts to increase as TSM receives heat in sensible heat form.
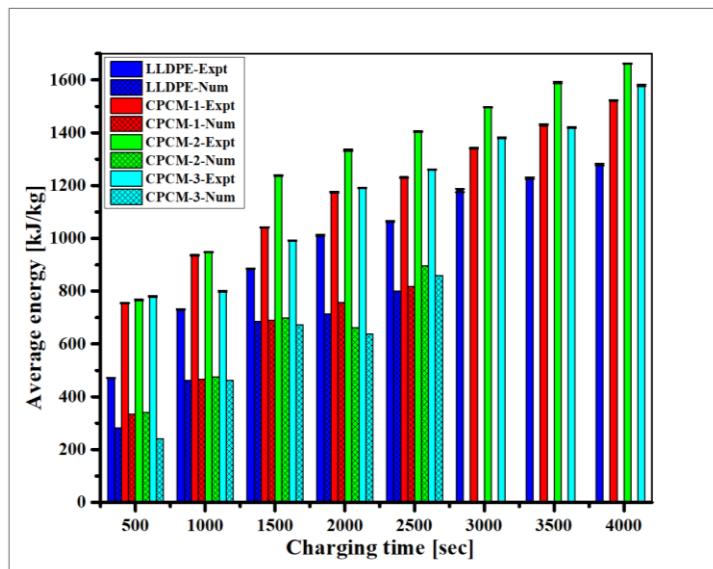
Figure 6.3: Experimental and numerical estimation of energy absorbed during melting process with charging time for different materials.

To understand the complete melting process, it is divided into eight time steps with increment of 500 sec and values are obtained at those points. At 4000 sec, the total energy absorbed and stored by different materials is found to be 1279.45, 1522.61, 1662 and 1580 for LLDPE, CPCM-1, CPCM-2, and CPCM-3 respectively. The energy level enhancement of 43.17, 50.42, 54, and 50.61% is recorded for LLDPE, CPCM-1, CPCM-2, and CPCM-3 respectively. Among the TSM CPCM-2 shows relatively better storage capability (54% enhancement) due to incorporation of optimum concentration of enhancing the material. Higher concentration causes a reduction in specific heat capacity of CPCM-3, and it leads to a reduction in thermal storability. The discrepancy between experimental and numerical results are due to insulation of thermal storage unit, measurement device, and operating conditions.

6.7 TEMPERATURE VARIATION DURING MELTING PROCESS

The temperature variation during the phase change process is monitored and found in the initial stage of the phase change process. The average temperature in simulation is slightly uniform for all TSMs. Experimental temperature values are higher for LLDPE and CPCM-1, but CPCM-2 and CPCM-3 temperature is lower than numerical results with an increase in heating plate temperature. As time progresses the viscous properties of the material, the temperature of CPCM-2 and CPCM-3 increases rapidly due to its higher thermal conductivity. The blending of high conductive material changes thermophysical properties, and thermal performance enhances.
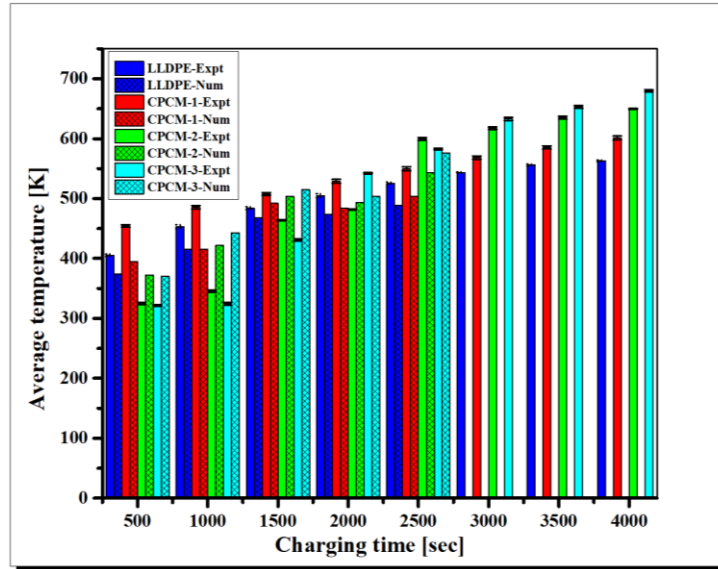
Figure 6.4: Experimental and numerical estimation of temperature variation during the melting process with charging time for different materials.

Figure 6.4 shows the numerical and experimental calculation of temperature variation during the melting process with charging time for different materials. The temperature variation data shows the temperature increment of 28, 24, 50, and 52.73% for LLDPE, CPCM-1,CPCM-2, and CPCM-3 respectively.

6.8 ENERGY REJECTION AND TEMPERATURE VARIATION DURING THE SOLIDIFICATION PROCESS

The complete solidification process requires 40000 sec, and it is divided into 8-time steps with an increment of 5000 sec to understand the solidification process. The heat rejection process is by natural convection and required more extended time to complete the process. The numerical and experimental calculations of energy rejection during the solidification process with discharging time for different materials, as shown in figure 6.5. A comparative study of experimental and numerical results are different, but it follows the same trend. At the beginning of the solidification process, the amount of heat energy stored in the TSM is 1279.45, 1522.61, 1662.09 and 1580.02 kJ calculated for LLDPE, CPCM-1, CPCM-2, and CPCM-3 respectively.
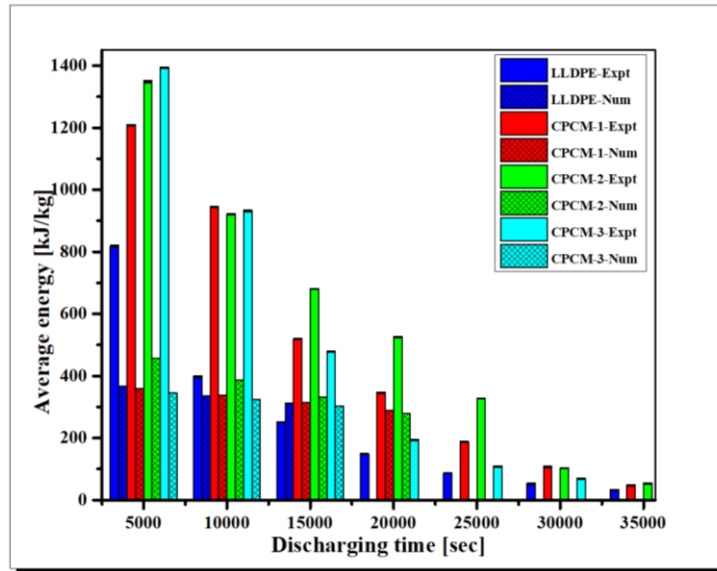
Figure 6.5: Experimental and numerical calculation of energy rejection during the solidification process with discharging time for different materials.

The TSM is kept open to atmosphere heat rejection takes place through natural convection, and a considerable amount of heat is rejected through radiation. The total heat rejection leads to energy level drop in the TSM, and as time progresses heat rejection process is continuous until it reaches the surrounding temperature. At the completion of the solidification process, the TSM energy level reduces 79.47, 80.05, 87.10 and 83.32% for LLDPE, CPCM-1, CPCM-2, and CPCM-3 respectively.

Figure 6.6 shows experimental and numerical calculations of temperature variation during the solidification process with discharging time for different materials. The temperature variation is high in the experiment, but it is uniform for numerical analysis, and the percentage variation is ranging between 11 and 23%. The temperature percentage reduction is 44, 46, 53.6, and 49.53% for LLDPE, CPCM-1, CPCM-2, and CPCM-3 respectively.
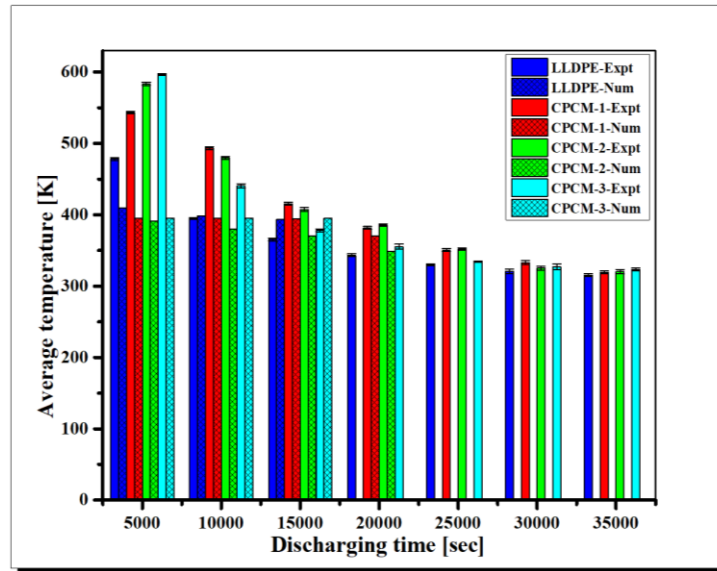
Figure 6.6: Experimental and numerical calculation of temperature variation during the solidification process with discharging time for different materials.

The maximum temperature loss is 53.6% for CPCM-2. Good agreement is seen for temperature variation between experimental and numerical results. The discrepancy is observed at the beginning of the solidification process, and it is due to conduction resistance ignored for numerical studies. This resistance causes a reduction in heat transfer rate and holds heat energy within the TSM and surface temperature is maintained constant throughout the process.

6.9 TOTAL HEAT REJECTION ANALYSIS

Thermophysical properties of TSM play a significant role in storing heat energy, such as thermal conductivity and viscosity respectively. Materials with high thermal conductivity lead faster charging, and discharging rate, same materials with high viscosity resists the particle migration during convection and controls the heat transfer rate.
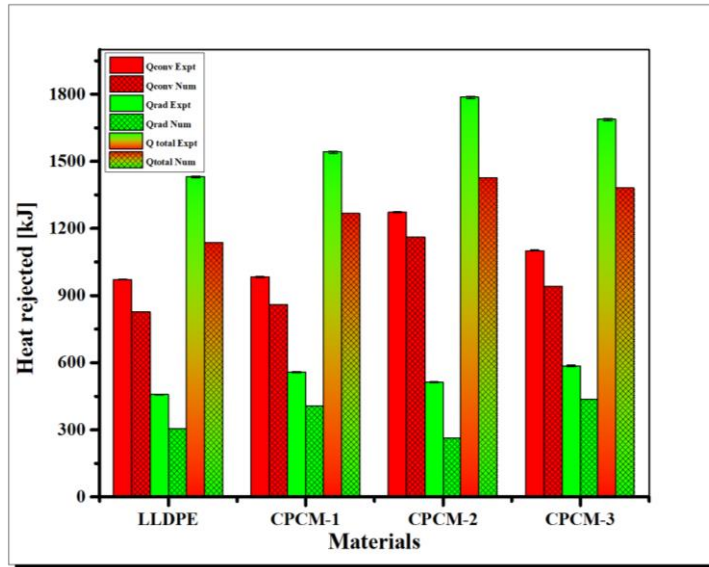
Figure 6.7: Experimental and numerical calculation of convection, radiation, and total heat transfer contribution during the solidification process for different materials.

Figure 6.7 shows experimental and numerical estimation of convection, radiation, and total heat transfer contribution during the solidification process for different materials. In the total amount of heat transfer, natural convection heat transfer contributes more, and the radiation effect subsidizes a considerable amount of heat. The convection heat transfer is calculated as 71.43, 69.45, 80, and 68.96% for LLDPE, CPCM-1, CPCM-2, and CPCM-3 respectively. Radiation heat loss contributes 28.57, 30.55, 20 and 31.03% for LLDPE, CPCM-1,CPCM-2 and CPCM-3 respectively. Maximum heat rejection is observed for CPCM-2 around 80% experimentally and 75% numerically.

6.10 HEATING AND COOLING CYCLE ANALYSIS

The amount of heat energy stored during the melting process is calculated by the amount of heat energy transferred from the heating plate to thermal storage material. Total energy supplied is the time integration of the instantaneous heat transfer rate during the melting process. Figure 6.8 shows the numerical and experimental comparison of energy stored and rejected during the complete cycle with time for different thermal storage materials. Initially, a sharp increment of the curve is observed, which indicates sensible heating of

TSM up to phase change temperature. It follows a plateau of gradual increase in energy level, and it reaches the saturation point above which phase change occurs. The CPCM-2 reaches the highest peak by absorbing 1662 kJ of heat. The consequent peaks are obtained at 1279.45, 1522.61, 1662 and 1580 kJ for LLDPE, CPCM-1, CPCM-2, and CPCM-3 respectively and completes the melting process at 4000 sec. As TSM reaches the molten phase heat supply is stopped and the top surface is kept open to allow heat rejection through natural convection.
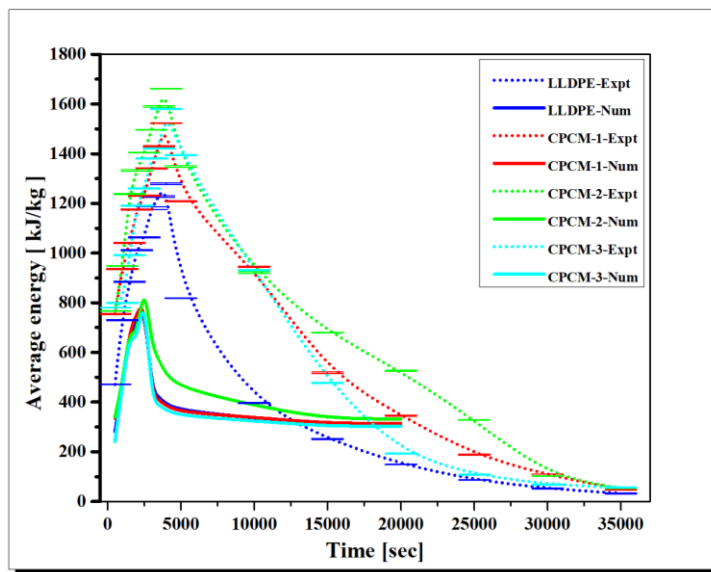
Figure 6.8: Experimental and numerical comparison of energy stored and released during the complete cycle with time for different thermal storage materials.

More heat rejection takes place by natural convection, but total heat rejection takes place by convection and radiation mode of heat transfer. Radiative heat loss subsidizes around 20 to 30%. The declining trend of curves shows the solidification process, and these curves are shorter for numerical compared to experimental results. The complete system is considered to be perfectly insulated, and the amount of heat released from the heater is completely absorbed by the materials without any thermal loss. During experiment, perfect insulation is not possible and some amount of heat absorbed by the thermal storage unit itself due to its material properties. Several unavoidable conditions also make the discrepancy between numerical and experimental results. The curves obtained through

simulation are shorter than experimental curves because the amount of heat energy supplied to the TSM is completely transferred.

Figure 6.9 experimental and numerical comparison of temperature variation during the complete cycle with time for different thermal storage materials. During the solidification process, TSM rejects heat faster and requires less time compared to experimental results. In numerical analysis, solidification process completes within 20000 sec of time interval, but the experiment completes 40000 sec. As TSM loses the sensible heat, the material temperature starts declining until it reaches the phase change temperature.
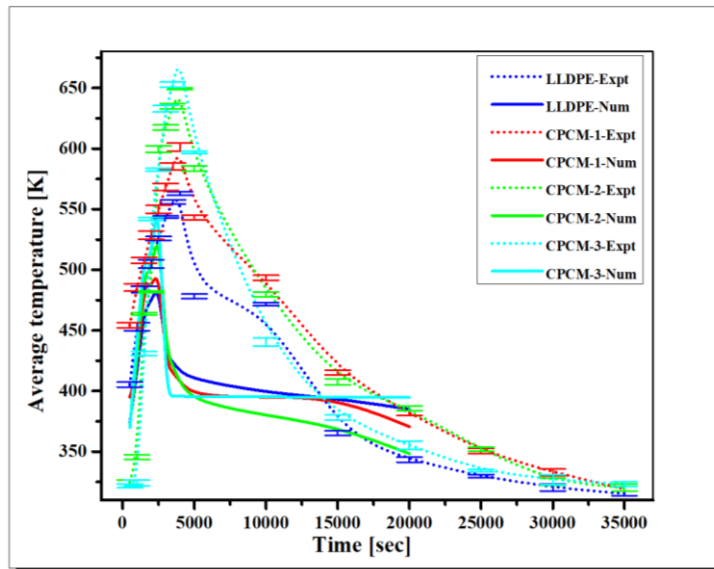
Figure 6.9: Experimental and numerical results comparison of temperature variation during the complete cycle with time for different thermal storage materials.

The instantaneous energy level is ascended to maximum energy level under the given operating conditions, in order to compare the results for both experimental and numerical results. It is clear that higher temperature differences lead to faster charging and discharging of sensible heat, and it affects the thermal energy storage performance.

6.11 UNCERTAINTY ANALYSIS OF THERMAL STORAGE SYSTEM

The uncertainty analysis is performed using three readings measured during the experiment. From the measurement, the average values are calculated. The accuracy of

K-type thermocouple is considered ± 0.5 °C or $\pm 0.75\%$ for temperature range 0 to 200°C. The uncertainty in power calculation is also observed as ± 0.5. The uncertainty is calculated using equations (6.9) and (6.10).

$$\sigma = \sqrt{\frac{\sum_{i=1}^{N}(X_i - \bar{X})^2}{N-1}}$$ 6.9

$$\bar{X} = \frac{X_1 + X_2 + X_3...}{N}$$ 6.10

Where X_i is Sample, $\bar{X}$ = Average sample values, and N is the number of samples.

The Uncertainty in measuring convective heat transfer is 2.5, and radiative heat transfer is 4.38. Table 6.4 shows the uncertainties observed during temperature measurement and energy calculations.

Table 6.4: Uncertainty observed during temperature measurement and energy calculations.

Materials	LLDPE	CPCM-1	CPCM-2	CPCM-3
Temperature Measurement	0.202041	0.459342	0.835275	0.553831
Energy Calculation	0.543252	0.426386	0.616323	0.70450

The uncertainty in measuring temperature is estimated as 0.202041, 0.459342, 0.835275, and 0.553831 for LLDPE, CPCM-1, CPCM-2, and CPCM-3 respectively. Uncertainty observed in calculating the thermal energy storage capacity of different materials are 0.543252, 0.426386, 0.616323 and 0.70450 for LLDPE, CPCM-1, CPCM-2, and CPCM-3 respectively.

6.12 CLOSURE

In this chapter, the experimental procedure of thermal storage capacity evaluation for different materials is discussed. Next, the variations of thermophysical properties during

melting and solidification processes are reported. To substantiate the experimental results, 3-D numerical analysis is also carried out and tabulated. Heat supply and rejection analysis are done for the heating and cooling cycle. The role of mass fraction and temperature variation are analyzed.

CHAPTER 7

CONCLUSIONS AND SCOPE OF FUTURE WORK

7.1 CONCLUSIONS

The present work successfully demonstrates the feasibility and applicability of plastic-based composite phase change materials (CPCMs) development using polyethylene as a base material for thermal energy storage applications. The effect of nanoparticle concentration (copper nanoparticles with 2, 5, 8, and 10%vol) on thermophysical properties of composite phase change materials are studied. It enhances the thermophysical properties, and heat transfer rate with an increase in nanoparticle concentration. Proper dispersion of highly conductive nanoparticles within conventional PCMs also enhances the thermophysical properties.

For better thermal performance different thermal storage system and material combinations are considered. A numerical study of a rectangular bounded domain with two different arrangements (deep and shallow) are analyzed with constant heat supply. The shallow domain is shown faster charging/discharging rate compared to the deep domain. The geometrical modification also affects the thermal performance of CPCMs. Three different wall heating (base, left and top wall) for four different orientations such as $45°$, $90°$(deep), $135°$ and $180°$ (shallow) domains are studied for understanding the melting and solidification characteristics of CPCMs. The heat transfer in the solidification process is by conduction but, in the melting process it, is by natural convection. Three models of square, pentagon and hexagon are studied, and TSM used is CPCM of paraffin wax and Al_2O_3 nanoparticles. Among the three models, the hexagon model shown optimum results for both the heating and cooling processes with uniform and smooth variation in liquid fraction and temperature.

Linear low-density polyethylene (LLDPE) is incorporated with functionalized graphene (f-Gr) with different concentrations (1, 3 and 5%) and CPCMs are named as CPCM-1,

CPCM-2 and CPCM-3 for 1, 3 and 5% blending respectively. Optimal concentration (3%) of nanoparticle provides favorable results and polyethylene-based composites with optimal concentration can be utilized for thermal energy storage applications. The preparation and characterization of polyethylene-graphene based CPCMs enhancement in the thermophysical properties are found. By using the thermophysical properties, numerical and experimental studies are carried out on the thermal performance of polyethylene-graphene based CPCMs to address the energy and pollution issues.

The conclusions are summarized as follows.

- Copper nanoparticle blending enhances the thermal conductivity and specific heat of CPCM increases upto 10% addition, above 10% addition the specific heat capacity reduces to 20%, which shows an adverse effect on the TES applications.

- The shallow domain is shown faster charging/discharging rate compared to the deep domain, and it requires 10% less time.

- Copper nanoparticles addition enhances the thermophysical properties in which thermal conductivity increased with nanoparticle concentrations. The specific heat capacity gets reduced up to 20%, which have an adverse effect and increases the volume requirement.

- The shallow domain is shown faster charging/discharging rate compared to the deep domain and requires up to 10% less time. Among three wall heating (base, left and top wall), top wall heating shows complete melting at minimum time. Top wall heating with shallow domain gives faster melting rate and raises the molten material temperature, and reduced viscosity leads to faster particle migration. Deep domain with top wall heating can be preferred for faster melting.

- The material characterization study revealed that the addition of functionalized graphene (f-Gr) nanoparticle provides enhanced thermophysical properties to the CPCMs. The latent heat storage capacity and heat of fusion increases to 20% for 5% addition of f-Gr nanoparticle.

- Numerical and experimental investigations are performed for thermal performance of four CPCMs such as LLDPE, CPCM-1, CPCM-2 and CPM-3. The energy level

enrichment is 43.17, 50.42, 54, and 50.61% for LLDPE, CPCM-1, CPCM-2, and CPCM-3 respectively.

- The temperature increases from 28, 24, 50 and 52.73% for LLDPE, CPCM-1, CPCM-2, and CPCM-3 respectively. During the solidification process, the temperature reduces 44, 46, 53.6 and 49.53% for LLDPE, CPCM-1, CPCM-2, and CPCM-3 respectively.

- Enhanced thermal storage capacity is achieved through optimum percentage blending (3%), and waste polyethylene can be successfully converted into thermal storage material. It will be very obliging in tackling energy issues and environmental pollution caused due to the usage of plastics.

- The functionalized graphene significantly improved the thermophysical properties of polyethylene, it is demonstrated that waste plastics can be manipulated, and it can be used for TES application like solar thermal storage.

- This thesis also addresses the global issues of energy preservation and controlling plastic pollution in the environment with cost reduction. TES model implementation also determines the better utilization of thermal energy for a greener environment.

7.2 SCOPE OF FUTURE WORK

(i) The present study extended for different aspect ratio of bounded domains like triangle, square, pentagon, and hexagon with the different base to enhance the thermal performance.

(ii) The present study extended for multiple cycles like 500, 1000, 2000, 3000 cycles to analyze the material stability and performance degradation.

(iii) The present study also extended for different orientations of geometries like triangle, square, pentagon, and hexagon models to enhance the thermal performance.

(iv) Different material combinations of composite phase change materials can be analyzed through TGA, SEM, FTIR, DSC analysis.

(v) Life cycle analysis of composite phase change materials for the different number of heating and cooling cycles.

(vi) The thermal stability analysis for the number of heating and cooling cycles.

(vii) Cost reduction possibilities of materials for thermal energy storage applications.

(viii) Thermal energy storage method can be extended for different thermal storage applications like domestic solar water heater, solar space heating, vapor absorption refrigeration systems, etc.

(ix) The LLDPE can be blended with different nanoparticles like fullerene, carbon nanotubes with different concentrations for thermophysical properties enhancement.

(x) The HDPE can be blended with different nanoparticles like fullerene, carbon nanotubes with different concentrations for thermophysical properties enhancement.

(xi) Thermal energy storage unit with cylindrical geometries can be experimented to analyze the effects on thermal performance.

(xii) Numerical and experimental analysis can be extended for commercial and industrial-scale applications.

REFERENCES

Abhat, A. (1983). "Low temperature latent heat thermal energy storage: Heat storage materials." *Sol. Energy*, 30(4), 313–332.

Abolghasemi, M., Keshavarz, A., and Mehrabian, M. A. (2012). "Thermodynamic analysis of a thermal storage unit under the influence of nano-particles added to the phase change material and / or the working fluid." *Int. J. Heat Mass Transfer.*, 12, 39-41.

Akeiber, H., Nejat, P., Majid, M. Z. A., Wahid, M. A., Jomehzadeh, F., Zeynali Famileh, I., Calautit, J. K., Hughes, B. R., and Zaki, S. A. (2016). "A review on phase change material (PCM) for sustainable passive cooling in building envelopes." *Renew. Sustain. Energy Rev.*, 60, 1470–1497.

Alkan, C. (2006). "Enthalpy of melting and solidification of sulfonated paraffins as phase change materials for thermal energy storage." *Thermochim. Acta*, 451(1–2), 126–130.

André, L., Abanades, S., and Flamant, G. (2016). "Screening of thermochemical systems based on solid-gas reversible reactions for high temperature solar thermal energy storage." *Renew. Sustain. Energy Rev.*, 64, 703–715.

Arthur, O., and Karim, M. A. (2016). "An investigation into the thermophysical and rheological properties of nanofluids for solar thermal applications." *Renew. Sustain. Energy Rev.*, 55, 739–755.

Atalla (1966). "A relationship between emissivity sand thermal conductivity of metals."

Brit. J. Appl. Phys, 573, 4–6.

Audichon, T., Guenot, B., Baranton, S., Cretin, M., Lamy, C., and Coutanceau, C. (2017). "Preparation and characterization of supported $RuxIr(1-x)O_2$ nano-oxides using a modified polyol synthesis assisted by microwave activation for energy storage applications." *Appl. Catal. B Environ.*, 200, 493–502.

Bailey, J. (2010). "Modelling Phase Change Material Thermal Storage Systems." *Open*

Access Diss. Theses, (4419).

Bechiri, M., and Mansouri, K. (2016). "Analytical study of heat generation effects on melting and solidification of nano-enhanced PCM inside a horizontal cylindrical enclosure." *Appl. Therm. Eng.*, 104, 779–790.

Bhatt, V. D., Gohi, K., and Mishra, A. (2010). "Thermal energy storage capacity of some phase changing materials and ionic liquids." *Int. J. ChemTech Res.*, 2(3), 1771–1779.

Bose, P., and Amirtham, V. A. (2016). "A review on thermal conductivity enhancement of paraffinwax as latent heat energy storage material." *Renew. Sustain. Energy Rev.*, 65, 81–100.

Cascetta, M., Cau, G., Puddu, P., and Serra, F. (2014). "Numerical investigation of a packed bed thermal energy storage system with different heat transfer fluids." *Energy Procedia*, 45, 598–607.

Costa, H. M. da, and Ramos, V. D. (2008). "Analysis of thermal properties and rheological behavior of LLDPE/EPDM and LLDPE/EPDM/SRT mixtures." *Polym. Test.*, 27(1), 27–34.

Cruz-Aguilar, A., Navarro-Rodríguez, D., Pérez-Camacho, O., Fernández-Tavizón, S., Gallardo-Vega, C. A., García-Zamora, M., and Barriga-Castro, E. D. (2018). "High-density polyethylene/graphene oxide nanocomposites prepared via in situ polymerization: Morphology, thermal, and electrical properties." *Mater. Today Commun.*, 16, 232–241.

Dahash, A., Ochs, F., Janetti, M. B., and Streicher, W. (2019). "Advances in seasonal thermal energy storage for solar district heating applications : A critical review on large-scale hot-water tank and pit thermal energy storage systems." *Appl. Energy*, 239, 2018), 296–315.

Das, N., Takata, Y., Kohno, M., and Harish, S. (2016). "Melting of graphene based phase change nanocomposites in vertical latent heat thermal energy storage unit." *Appl. Therm. Eng.*, 107, 101–113.

Delgado, M., Lázaro, A., Mazo, J., Marín, J. M., and Zalba, B. (2012). "Experimental

analysis of a microencapsulated PCM slurry as thermal storage system and as heat transfer fluid in laminar flow." *Appl. Therm. Eng.*, 36(1), 370–377.

Demirel, Y., and Öztürk, H. H. (2006). "Thermoeconomics of seasonal latent heat storage system." *Int. J. Energy Res.*, 30(12), 1001–1012.

Dinker, A., Agarwal, M., and Agarwal, G. D. (2017). "Experimental assessment on thermal storage performance of beeswax in a helical tube embedded storage unit." *Appl. Therm. Eng.*, 111, 358–368.

Fan, L. W., Fang, X., Wang, X., Zeng, Y., Xiao, Y. Q., Yu, Z. T., Xu, X., Hu, Y. C., and Cen, K. F. (2013). "Effects of various carbon nanofillers on the thermal conductivity and energy storage properties of paraffin-based nanocomposite phase change materials." *Appl. Energy*, 110, 163–172.

Fauzi, H., Metselaar, H. S. C., Mahlia, T. M. I., and Silakhori, M. (2014). "Thermal reliability of myristic acid/palmitic acid/sodium laurate eutectic mixture: A feasibility study of accelerated aging for thermal energy storage application." *Energy Procedia*, 61, 49–54.

Ferrão, P. (2017). "Performance of Composite Building Materials with Phase Change Material for Assessing the feasibility of using the heat demand-outdoor Thermal temperature forecast function for district heat." *Energy Procedia*, 143, 125–130.

Gao, L., Zhao, J., An, Q., Zhao, D., Meng, F., and Liu, X. (2017). "Experiments on thermal performance of erythritol/expanded graphite in a direct contact thermal energy storage container." *Appl. Therm. Eng.*, 113, 858–866.

Ge, Z., Ye, F., Cao, H., Leng, G., Qin, Y., and Ding, Y. (2014). "Carbonate-salt-based composite materials for medium- and high-temperature thermal energy storage." *Particuology*, 15, 77–81.

Guo, X., Zhang, S., and Cao, J. (2018). "An energy-efficient composite by using expanded graphite stabilized paraffin as phase change material." *Compos. Part A*, 107, 83–93.

Hasadi, Y. M. F. El. (2013). "Numerical Simulation of the Effect of the Size of Suspensions

on the Solidification Process of Nanoparticle-Enhanced Phase Change Materials." 135, 1–11.

Huang, X., Lin, Y., Alva, G., and Fang, G. (2017). "Thermal properties and thermal conductivity enhancement of composite phase change materials using myristyl alcohol / metal foam for solar thermal storage." *Sol. Energy Mater. Sol. Cells*, 170, 68–76.

Huang, Z., Gao, X., Xu, T., Fang, Y., and Zhang, Z. (2014). "Thermal property measurement and heat storage analysis of $LiNO_3$/KCl - expanded graphite composite phase change material." *Appl. Energy*, 115, 265–271.

Jackson, M. A., and Eller, F. J. (2006). "Isolation of long-chain aliphatic alcohols from beeswax using lipase-catalyzed methanolysis in supercritical carbon dioxide." *J. Supercrit. Fluids*, 37(2), 173–177.

J. C., Kou, Y., Wang, S., Luo, J., Sun, K., Zhang, J., Tan, Z., and Shi, Q. (2019). "Thermal analysis and heat capacity study of polyethylene glycol (PEG) phase change materials for thermal energy storage applications." *J. Chem. Thermodyn.*, 128, 259–274.

Jiji, L. M., and Gaye, S. (2006). "Analysis of solidification and melting of PCM with energy generation." *Appl. Therm. Eng.*, 26(5–6), 568–575.

Kalaiselvam, S., Veerappan, M., Arul Aaron, A., and Iniyan, S. (2008). "Experimental and analytical investigation of solidification and melting characteristics of PCMs inside cylindrical encapsulation." *Int. J. Therm. Sci.*, 47(7), 858–874.

Kamkari, B., and Shokouhmand, H. (2014). "Experimental investigation of phase change material melting in rectangular enclosures with horizontal partial fins." *Int. J. Heat Mass Transf.*, 78, 839–851.

Khodadadi, J. M., and Hosseinizadeh, S. F. (2007). "Nanoparticle-enhanced phase change materials (NEPCM) with great potential for improved thermal energy storage." 34, 534–543.

Khonakdar, H. A. (2015). "Dynamic mechanical analysis and thermal properties of LLDPE/EVA/modified silica nanocomposites." *Compos. Part B Eng.*, 76, 343–353.

Koushal, V., Sharma, R., Sharma, M., Sharma, R., and Sharma, V. (2014). "Plastics : Issues Challenges and Remediation." *International Journal of Waste Resources* 4(1), 1–6.

Kumar, A., and Shukla, S. K. (2015). "A Review on Thermal Energy Storage Unit for Solar Thermal Power Plant Application." *Energy Procedia*, 74, 462–469.

Li, T., Sun, H., Lei, F., Li, D., Leng, J., Chen, L., Huang, Y., and Sun, D. (2019). "High performance linear low density polyethylene nanocomposites reinforced by two-dimensional layered nanomaterials." *Polymer (Guildf).*, 172, 142–151.

Li, Z., and Wu, Z.-G. (2014). "Numerical study on the thermal behavior of phase change materials (PCMs) embedded in porous metal matrix." *Sol. Energy*, 99, 172–184.

Lin, S., Anwer, M. A. S., Zhou, Y., Sinha, A., Carson, L., and Naguib, H. E. (2018). "Evaluation of the thermal, mechanical and dynamic mechanical characteristics of modified graphite nanoplatelets and graphene oxide high-density polyethylene composites." *Compos. Part B Eng.*, 132, 61–68.

Liu, Z., Hu, D., Lv, H., Zhang, Y., Wu, F., Shen, D., and Fu, P. (2017a). "Mixed mill-heating fabrication and thermal energy storage of diatomite / paraffin phase change composite incorporated gypsum-based materials." *Appl. Therm. Eng.*, 118, 703–713.

Liu, Z., Wu, B., Fu, X., Yan, P., Yuan, Y., Zhou, C., and Lei, J. (2017b). "Two components based polyethylene glycol / thermosetting solid-solid phase change material composites as novel form stable phase change materials for fl exible thermal energy storage application." 170, 197–204.

Lu, J., Yu, T., Ding, J., and Yuan, Y. (2014). "Thermal analysis of molten salt thermocline thermal storage system with packed phase change bed." *Energy Procedia*, 61, 2038–2041.

Lu, X., Huang, J., Kang, B., Yuan, T., and Qu, J. (2019). "Solar Energy Materials and Solar Cells Bio-based poly (lactic acid)/ high-density polyethylene blends as shape- stabilized phase change material for thermal energy storage applications." *Sol. Energy Mater. Sol. Cells*, 192, 170–178.

Lv, Y., Zhou, W., Yang, Z., and Jin, W. (2016). "Characterization and numerical

simulation on heat transfer performance of inorganic phase change thermal storage devices." *Appl. Therm. Eng.*, 93, 788–796.

Ma, T., Chang, P. R., Zheng, P., and Ma, X. (2013). "The composites based on plasticized starch and graphene oxide/reduced graphene oxide." *Carbohydr. Polym.*, 94(1), 63–70.

Mahdi, J. M., and Nsofor, E. C. (2016). "Solidification of a PCM with nanoparticles in triplex-tube thermal energy storage system." *Appl. Therm. Eng.*, 108, 596–604.

Medrano, M., Gil, A., Martorell, I., Potau, X., and Cabeza, L. F. (2010). "State of the art on high-temperature thermal energy storage for power generation. Part 2-Case studies." *Renew. Sustain. Energy Rev.*, 14(1), 56–72.

Mettawee, E. S., and Assassa, G. M. R. (2007). "Thermal conductivity enhancement in a latent heat storage system." *Solar Energy* 81, 839–845.

Molefi, J. A., Luyt, A. S., and Krupa, I. (2010). "Comparison of LDPE , LLDPE and HDPE as matrices for phase change materials based on a soft Fischer – Tropsch paraffin wax." *Thermochim. Acta*, 500(1–2), 88–92.

Moreno, D. D. P., and Saron, C. (2017). "Low-density polyethylene waste/recycled wood composites." *Compos. Struct.*, 176, 1152–1157.

Nazir, H., Batool, M., Bolivar, F. J., Isaza-ruiz, M., Xu, X., Vignarooban, K., Phelan, P., and Kannan, A. M. (2019). "Recent developments in phase change materials for energy storage applications : A review." *Int. J. Heat Mass Transf.*, 129, 491–523.

Oró, E., Gil, A., Miró, L., Peiró, G., Álvarez, S., and Cabeza, L. F. (2012). "Thermal energy storage implementation using phase change materials for solar cooling and refrigeration applications." *Energy Procedia*, 30, 947–956.

Parsazadeh, M., and Duan, X. (2017). "Numerical and statistical study on melting of nanoparticle enhanced phase change material in a shell-and-tube thermal energy storage system." *Appl. Therm. Eng.*, 111, 950–960.

Paul, A., Shi, L., and Bielawski, C. W. (2015). "A eutectic mixture of galactitol and mannitol as a phase change material for latent heat storage." *Energy Convers. Manag.*, 103,

139–146.

Pielichowska, K., Bieda, J., and Szatkowski, P. (2016a). "Polyurethane/graphite nano-platelet composites for thermal energy storage." *Renew. Energy*, 91, 456–465.

Pielichowska, K., Nowak, M., Szatkowski, P., and Macherzyńska, B. (2016b). "The influence of chain extender on properties of polyurethane-based phase change materials modified with graphene." *Appl. Energy*, 162, 1024–1033.

Pina, A., Ferrão, P., Fournier, J., Lacarrière, B., and Corre, O. Le. (2017). "Preparation of microencapsulated phase change materials (MEPCM) Assessing the feasibility of Kokogiannakis using the heat temperature function for a long-term district heat demand forecast." *Energy Procedia*, 121, 95–101.

Putra, N., Rawi, S., Amin, M., Kusrini, E., Kosasih, E. A., and Indra Mahlia, T. M. (2019). "Preparation of beeswax/multi-walled carbon nanotubes as novel shape-stable nanocomposite phase-change material for thermal energy storage." *J. Energy Storage*, 21, 32–39.

Raam Dheep, G., and Sreekumar, A. (2014). "Influence of nanomaterials on properties of latent heat solar thermal energy storage materials - A review." *Energy Convers. Manag.*, 83, 133–148.

Rao, Z., Wang, S., Wu, M., Zhang, Y., and Li, F. (2012). "Molecular dynamics simulations of melting behavior of alkane as phase change materials slurry." *Energy Convers. Manag.*, 64, 152–156.

Saeed, R. M., Schlegel, J. P., Castano, C., and Sawafta, R. (2018). "Preparation and enhanced thermal performance of novel (solid to gel) form-stable eutectic PCM modified by nano-graphene platelets." *J. Energy Storage*, 15, 91–102.

Saha, M., Tambe, P., and Pal, S. (2016). "Thermodynamic approach to enhance the dispersion of graphene in epoxy matrix and its effect on mechanical and thermal properties of epoxy nanocomposites." *Compos. Interfaces*, 6440, 1–18.

Şahan, N., and Paksoy, H. (2017). "Investigating thermal properties of using nano-tubular

ZnO powder in paraffin as phase change material composite for thermal energy storage." *Compos. Part B Eng.*, 126, 88–93.

Sanusi, O., Warzoha, R., and Fleischer, A. S. (2011). "Energy storage and solidification of paraffin phase change material embedded with graphite nanofibers." *Int. J. Heat Mass Transf.*, 54(19–20), 4429–4436.

Sarı, A., and Karaipekli, A. (2007). "Thermal conductivity and latent heat thermal energy storage characteristics of paraffin / expanded graphite composite as phase change material." *Applied Thermal Engineering*, 27, 1271–1277.

Sathishkumar, A., Kumaresan, V., and Velraj, R. (2016). "Solidification characteristics of water based graphene nanofluid PCM in a spherical capsule for cool thermal energy storage applications." *Int. J. Refrig.*, 66, 73–83.

Schuller, M., Shao, Q., and Lalk, T. (2015). "Experimental investigation of the specific heat of a nitrate-alumina nanofluid for solar thermal energy storage systems." *Int. J. Therm. Sci.*, 91, 142–145.

Sharma, A., Tyagi, V. V., Chen, C. R., and Buddhi, D. (2009). "Review on thermal energy storage with phase change materials and applications." *Renew. Sustain. Energy Rev.*, 13(2), 318–345.

Shen, Q., Ouyang, J., Zhang, Y., and Yang, H. (2017). "Applied Clay Science Lauric acid / modi fi ed sepiolite composite as a form-stable phase change material for thermal energy storage." *Appl. Clay Sci.*, 146(April), 14–22.

Sobolciak, P., Karkri, M., Krupa, I., and Maadeed, M. Al. (2015). "Storage and release of thermal energy of phase change materials based on linear low density of polyethylene, parafin wax and expanded graphite." *Proc. TMS Middle East - Mediterr. Mater. Congr. Energy Infrastruct. Syst. MEMA 2015*, 0.

Takahashi, Y. (1988). "Heat Capacities and Latent Heats of of $LiNO_3$, $NaNO_3$, and KNO_3." *International Journal of Thermophysics,* 9, 1081-1090.

Tang, Y., Alva, G., Huang, X., Su, D., Liu, L., and Fang, G. (2016a). "Thermal properties

and morphologies of MA-SA eutectics/CNTs as composite PCMs in thermal energy storage." *Energy Build.*, 127, 603–610.

Tang, Y., Jia, Y., Alva, G., Huang, X., and Fang, G. (2016b). "Synthesis, characterization and properties of palmitic acid/high density polyethylene/graphene nanoplatelets composites as form-stable phase change materials." *Sol. Energy Mater. Sol. Cells*, 155, 421–429.

Tang, Y., Lin, Y., Jia, Y., and Fang, G. (2017). "Improved thermal properties of stearyl alcohol / high density polyethylene / expanded graphite composite phase change materials for building thermal energy storage." *Energy Build.*, 153, 41–49.

Teng, T. P., Cheng, C. M., and Cheng, C. P. (2013). "Performance assessment of heat storage by phase change materials containing MWCNTs and graphite." *Appl. Therm. Eng.*, 50(1), 637–644.

Torkkeli, A. (2003). "Droplet microfluidics on a planar surface." *VTT Publ.*, 52(504), 3–194.

Wang, C., Lin, T., Li, N., and Zheng, H. (2016a). "Heat transfer enhancement of phase change composite material: Copper foam/paraffin." *Renew. Energy*, 96, 960–965.

Wang, Y., Chen, Z., and Ling, X. (2016b). "A molecular dynamics study of nano-encapsulated phase change material slurry." *Appl. Therm. Eng.*, 98, 835–840.

Wang, Y., Liang, D., Liu, F., Zhang, W., Di, X., and Wang, C. (2017). "A polyethylene glycol / hydroxyapatite composite phase change material for thermal energy storage." *Appl. Therm. Eng.*, 113, 1475–1482.

Wei, P., and Bai, S. (2015). "Fabrication of a high-density polyethylene/graphene composite with high exfoliation and high mechanical performance via solid-state shear milling." *RSC Adv.*, 5(114), 93697–93705.

Wu, S., Wang, H., Xiao, S., and Zhu, D. (2012). "Numerical simulation on thermal energy storage behavior of Cu/paraffin nanofluids PCMs." *Procedia Eng.*, 31, 240–244.

Xiang, J., and Drzal, L. T. (2011). "Investigation of exfoliated graphite nanoplatelets

(xGnP) in improving thermal conductivity of paraffin wax-based phase change material." *Sol. Energy Mater. Sol. Cells*, 95(7), 1811–1818.

Xu, G., Leng, G., Yang, C., Qin, Y., Wu, Y., Chen, H., and Cong, L. (2017a). "Sodium nitrate – Diatomite composite materials for thermal energy storage." *Sol. Energy*, 146, 494–502.

Xu, T., Li, Y., Chen, J., and Liu, J. (2017b). "Preparation and thermal energy storage properties of LiNO $_3$ -KCl-NaNO $_3$ / expanded graphite composite phase change material." *Sol. Energy Mater. Sol. Cells*, 169, 215–221.

Xu, X., Zhang, X., and Munyalo, J. M. (2019). "Key technologies and research progress on enhanced characteristics of cold thermal energy storage." *J. Mol. Liq.*, 278, 428–437.

Yang, D., Shi, S., Xiong, L., Guo, H., Zhang, H., Chen, X., Wang, C., and Chen, X. (2016a). "Paraffin/Palygorskite composite phase change materials for thermal energy storage." *Sol. Energy Mater. Sol. Cells*, 144, 228–234.

Yang, J., Tang, L.-S., Bao, R.-Y., Bai, L., Liu, Z.-Y., Yang, W., Xie, B.-H., and Yang, M.-B. (2017). "Largely enhanced thermal conductivity of poly (ethylene glycol)/boron nitride composite phase change materials for solar-thermal-electric energy conversion and storage with very low content of graphene nanoplatelets." *Chem. Eng. J.*, 315, 481–490.

Yang, J., Zhang, E., Li, X., Zhang, Y., Qu, J., and Yu, Z. Z. (2016b). "Cellulose/graphene aerogel supported phase change composites with high thermal conductivity and good shape stability for thermal energy storage." *Carbon N. Y.*, 98, 50–57.

Yang, X., Bai, Q., Zhang, Q., Hu, W., Jin, L., and Yan, J. (2018a). "Thermal and economic analysis of charging and discharging characteristics of composite phase change materials for cold storage." *Appl. Energy*, 225, 585–599.

Yang, Z., Xu, Z., Zhang, L., and Guo, B. (2018b). "Dispersion of graphene in chlorosulfonated polyethylene by slurry compounding." *Compos. Sci. Technol.*, 162, 156–162.

Ye, F., Ge, Z., Ding, Y., and Yang, J. (2014). "Multi-walled carbon nanotubes added to

Na$_2$CO$_3$/MgO composites for thermal energy storage." *Particuology*, 15, 56–60.

Youssef, Z., Delahaye, A., Huang, L., Trinquet, F., Fournaison, L., Pollerberg, C., and Doetsch, C. (2013). "State of the art on phase change material slurries." *Energy Convers. Manag.*, 65, 120–132.

Yuan, H., Shi, Y., Xu, Z., Lu, C., Ni, Y., and Lan, X. (2014). "Effect of nano-MgO on thermal and mechanical properties of aluminate cement composite thermal energy storage materials." *Ceram. Int.*, 40(3), 4811–4817.

Yuan, P., Zhang, P., Liang, T., Zhai, S., and Yang, D. (2019). "Effects of functionalization on energy storage properties and thermal conductivity of graphene/n-octadecane composite phase change materials." *J. Mater. Sci.*, 54(2), 1488–1501.

Yuan, Y., Zhang, N., Li, T., Cao, X., and Long, W. (2016). "Thermal performance enhancement of palmitic-stearic acid by adding graphene nanoplatelets and expanded graphite for thermal energy storage: A comparative study." *Energy*, 97, 488–497.

Zhang, H. L., Baeyens, J., Degrève, J., Cáceres, G., Segal, R., and Pitié, F. (2014). "Latent heat storage with tubular-encapsulated phase change materials (PCMs)." *Energy*, 76, 66–72.

Zhang, X., Chen, X., Han, Z., and Xu, W. (2016). "Study on phase change interface for erythritol with nano-copper in spherical container during heat transport." *Int. J. Heat Mass Transf.*, 92, 490–496.

Zheng, J. P. (1995). "Hydrous Ruthenium Oxide as an Electrode Material for Electrochemical Capacitors." *J. Electrochem. Soc.*, 142(8), 2699.

Zhong, Y., Zhou, M., Huang, F., Lin, T., and Wan, D. (2013). "Effect of graphene aerogel on thermal behavior of phase change materials for thermal management." *Sol. Energy Mater. Sol. Cells*, 113, 195–200.

Zhou, M., Bi, H., Lin, T., Lü, X., Wan, D., Huang, F., and Lin, J. (2014). "Heat transport enhancement of thermal energy storage material using graphene/ceramic composites." *Carbon N. Y.*, 75, 314–321.

LIST OF PUBLICATIONS BASED ON PH.D. RESEARCH WORK

S. No.	Title of the paper	Authors (in the same order as in the paper. Underline the Research Scholar's name	Name of the Journal/ Conference, Vol., No., Pages	Month, Year of Publication	Category *
1	A Review on Thermal Energy Storage Using Composite Phase Change Materials	**Santosh C**, Veershetty Gumtapure, Arumuga Perumal D.	*Recent Patents on Mechanical Engineering, Bentham science publishers, Vol. 11 (4), 298-310.* **(Scopus Indexed).**	*December 2018*	1
2	Computational Investigation of Bounded Domain with Different Orientations Using CPCM	**Santosh C,** Gumtapure V, Arumuga Perumal D.	*Journal of Energy Storage, Elsevier Publishers, Vol. 22, 355-372.* **SCIE (Scopus) Indexed, IF 3.5**	*March 2019*	1
3	Characterization of Linear Low-Density Polyethylene with Graphene as Thermal Energy Storage Material.	**Santosh C,** Veershetty Gumtapure, Arumuga Perumal D	*IOP Publishers, Materials Research Express, Vol. 6, 065511, 1-9* **SCIE (Scopus) Indexed IF 1.151**	*March 2019*	1
4	Numerical studies for charging and discharging characteristics of composite phase change material in a deep and shallow rectangular enclosure	**Santosh C,** Arumuga Perumal D, Veershetty Gumtapure	*IOP Conf. Series: Materials Science and Engineering 376 (2018) 012059, 1-8.* **(Scopus Indexed)**	*June 2018*	3

5	Preparation and characterization of nanoparticle blended polymers for thermal energy storage applications	**Santosh C,** Veershetty G and D.A. Perumal,	*AIP Conference Proceedings 2057, 020028,1-8.* **(Scopus Indexed)**	*January 2019*	3
6	Numerical analysis of composite phase change material in a square enclosure	**Santosh C,** Veershetty Gumtapure, Arumuga Perumal D,	*Published in ICAER 2017 at IIT Bombay and extended version going to appear in Springer Proceedings in Energy.* *(Under production)*. **(Scopus Indexed)**.	*December20 17*	3
7	Melting and Solidification Characteristics for Thermal Energy Storage Applications –A computational study	**Santosh C**, Veershetty Gumtapure, Arumuga Perumal D,	*Second International Conference on Recent Trends in Materials Science and Technology 2018 (ICMST 2018), Thiruvananthapuram.*	*October 2018*	4
8	Effect of geometry on heating and cooling characteristics for thermal energy storage- A Computational Study	**Santosh C,** Veershetty Gumtapure, Arumuga Perumal D,	*12th International Conference on Thermal Engineering: Theory and Application (ICTEA-2019), Gandhinagar.*	*February 2019*	4

*Category: 1: Journal paper, full paper reviewed   2: Journal paper, Abstract reviews   3: Conference/Symposium paper, full paper reviewed   4: Conference/Symposium paper, abstract reviewed   5: others (including papers in Workshops, NITK Research Bulletins, Short notes etc.)

Santosh	**Dr. Veershetty Gumtapure**	**Dr. Arumuga Perumal D**
Research Scholar	Research Guide	Research Guide
Name & Signature, with Date	Name & Signature, with Date	Name & Signature, with Date

BIODATA

NAME: SANTOSH

DATE OF BIRTH: 02-10-1989

Mobile No.: +91 9886600171

Email: santosh.chavan083@gmail.com

ADDRESS:

Bhagya Nagar, Sedam road, Near ESIC hospital Kalaburagi, Karnataka 585102.

QUALIFICATION:

Examination	Board/Institute	Year	Percentage/ CGPA
Ph. D (course work)	NITK, Surathkal	2016	6.5
M. Tech (Thermal Engg.)	PDACE Kalaburagi	2011-13	9.01
B.E. (Mechanical Engg)	Dr. AIT Bengaluru	2006-10	60.25%

EXPERIENCE:

Sr. no	Name of the college/Institute	Designation	From	To
1.	Sahyadri Valley College of Engineering and Technology, Alephata, Pune.	Assistant Professor	Sept 2013	June 2014.
2.	Imperial College of Engineering and Research, Wagholi, Pune.	Assistant Professor	July2014	June 2016